CONDUCTIVITY MEASUREMENTS OF MOLTEN METAL OXIDE ELECTROLYTES
AND THEIR EVALUATION IN A DIRECT CARBON FUEL CELL (DCFC)

By

Venkata Raviteja Yarlagadda

Submitted to the graduate degree program in Chemical and Petroleum engineering and the
graduate faculty of the University of Kansas in partial fulfillment of the requirements for the
degree of Master of Science

_____

Chairperson Dr. Trung Van Nguyen

_____

Dr. Laurence Weatherley

_____

Dr. Susan Williams

Date defended: August 26, 2011

The Thesis Committee for Venkata Raviteja Yarlagadda

certifies that this is the approved version of the following thesis:

CONDUCTIVITY MEASUREMENTS OF MOLTEN METAL OXIDE ELECTROLYTES AND THEIR EVALUATION IN A DIRECT CARBON FUEL CELL (DCFC)

_____

Chairperson Dr. Trung Van Nguyen

_____

Dr. Laurence Weatherley

_____

Dr. Susan Williams

Date approved: August 31, 2011

ABSTRACT

Since Direct Carbon Fuel Cell (DCFC) technology is in a beginning stage, emphasis should be laid on addressing the fundamental aspects. A molten electrolyte is required to facilitate ionic contact between solid carbon fuel and electrolyte in a DCFC. Three different metal oxide electrolytes (Bi_2O_3, V_2O_5, and TeO_2) have been chosen based on their ability to form stable liquids in air at higher temperatures. Conductivity data beyond their melting points was not readily available for most of the metal oxides. Conductivity studies concerning the above mentioned molten metal oxides have been thoroughly investigated in this study. A four probe measurement method using an AC milliohm-meter at 1 KHz validated by Electrochemical Impedance Spectroscopy (EIS) was used to acquire the conductivity data because of its accuracy when compared to two probe measurement widely used in literature. Also, a DC ohmmeter was used to check whether these metal oxides exhibit electronic conductivity. Experimental results corresponding to the accuracy of DC ohmmeter showed that, it accurately detected the electronic component of the electrolyte. These conductivity studies revealed that the molten oxide electrolytes exhibit high ionic conductivity, in particular, beyond their melting points. Of all the three metal oxides, Bi_2O_3 demonstrated high ionic conductivity but with minor stability issues under CO_2 environment. Under CO_2 environment Bi_2O_3 showed a slight decrease in the conductivity. EDX analysis revealed an increase in carbon content by 50 percent per one mole of bismuth which can be attributed to possible carbonate formation. V_2O_5 exhibited lower ionic conductivity when compared to Bi_2O_3 but had the advantage of lower cost and higher abundance. Also, the higher volumetric expansion of V_2O_5 upon cooling from its melting point i.e. 690°C caused the

alumina crucible containing the metal oxide to break leading to leakage problems. Investigating further, quartz was found to be the best material for handling V_2O_5. Conductivity of TeO_2 was measured using a quartz crucible since it formed a Al_2TeO_6 complex by reacting with alumina. Ionic conductivity of TeO_2 was almost as high as Bi_2O_3.

Performance of these molten metal oxides in a DCFC has been evaluated. Dense YSZ solid electrolyte and porous LSM cathode used in the DCFC have been prepared by high temperature sintering. Efficiency of Bi_2O_3 based DCFC was mainly limited by unwanted bismuth ion reduction to bismuth metal at the carbon anode oxidation potential. Shorting of the LSM cathode by molten V_2O_5 leaking out of the crucible at high temperatures was found to be major concern corresponding to the performance of V_2O_5 and TeO_2 based DCFC. Based on these results, several fundamental material issues that need to be resolved have been identified.

ACKNOWLEDGEMENT

TABLE OF CONTENTS

LIST OF FIGURES

LIST OF TABLES

.

NOMECLATURE

R_{sol} Resistance of the electrolyte, ohm

$R_{electrode}$ Resistance of the electrode, ohm

$R_{kinetic}$ Kinetic resistance of the electrode, ohm

C Capacitance, Faraday

ρ Resistivity of the electrolyte, ohm-cm

σ mix   Mixed conductivity of the electrolyte, S/cm

σ el   Electronic conductivity of the electrolyte, S/cm

$\dfrac{L}{A}$ Cell constant (length per unit area), cm^{-1}

f Frequency, Hz

V Thermodynamic potential of DCFC, Volts

T Temperature of the furnace, $^{\circ}$C

I Current density, A/cm^{2}

R_{areal} Electronic areal resistance, ohm/cm^{2}

P Power density, W/cm^{2}

CHAPTER 1

Introduction

1.1 History of Direct Carbon Fuel Cells (DCFC)

Direct Carbon Fuel Cell (DCFC) was first discovered by Sir William Grove in 1839. [1] After several attempts to perfect the invention, the first Direct Carbon Fuel Cell (DCFC) was built in 1896 by Dr. William W. Jacques using molten hydroxide as electrolyte. Different cells, electrolytes and cathode materials were used during the experiments. Finally a 100 cell stack was organized which generated over 1kW of electricity. However, the first DCFC had a short lifetime due to rapid degeneration of the electrolyte. This device was considered as a primary battery, not fuel cell, as the electrolyte was progressively consumed to form sodium carbonate by reacting with carbon dioxide produced within the melt. For the next 40 years European researchers attempted to duplicate Dr. Jacques's results but without any success. The next major find came around 1970s during the oil crisis. Dr. Robert Weaver from Stanford Research Institute (SRI) was successful in proving that electrochemical oxidation of carbon is feasible. [1] Later Dr. Weaver and his research group tested different types of carbons in their molten carbonate DCFC. Their results demonstrated that a coal derived anode was much more electrochemically active than a graphite anode. In 1987 Dr. Vutetakis demonstrated a novel approach towards electrochemical oxidation of coal at higher temperatures. [2] The main distinction with previous DCFC studies was that dispersed, granulated carbon was used as fuel with molten carbonate as electrolyte. His configuration did not yield higher current densities due to heavy chemical consumption of carbon by

CO_2, which resulted in low carbon utilization efficiency. Funding for DCFC research was suspended temporarily until mid 1980s as the oil prices went down.

In 1995 Scientific Applications & Research Associates (SARA) revived the DCFC research using molten hydroxide as electrolyte and solid graphite as fuel. [3] In the recent years different designs of DCFC are being researched at Lawrence Livermore National laboratory, Cell Tech Power LLC and SRI International simultaneously with SARA. [3]

1.2 Background and working principle of DCFC

Increasing energy demand in the present day world summons the need for clean energy production. Of all the fossil fuel resources available, coal is the most abundant and accounts for 60% of the world's fossil fuel resources.[4-5] The conventional method of converting chemical energy in coal to electrical energy is by combustion which is only 35 % efficient. Combustion is not an efficient process due to increased CO_2 emission per unit of electrical energy output. DCFC has an efficiency of 70% (twice as efficient compared to combustion) and ability to convert carbon rich solid fuels such as coal and biomass directly into electricity. The concentrated carbon dioxide generated from this fuel cell can also be effectively captured and sequestered thus eliminating many pollution issues caused by conventional coal combustion. Hence, DCFCs are more environmentally friendly than coal-fired power plants.

Figure 1.1 shows a schematic of Direct Carbon Fuel Cell (DCFC). [5] Solid carbon fuels such as coal and biomass act as an anode and air is introduced at the cathode where oxygen is reduced. Electrochemical reactions involved in the DCFC are shown below.

$$\text{Anode:} \quad C + 2O^{=} \longrightarrow CO_2 + 4e^{-}$$

$$\text{Cathode:} \quad O_2 + 4e^{-} \longrightarrow 2O^{=}$$

$$\rule{8cm}{0.4pt}$$

$$\text{Overall:} \quad C + O_2 \longrightarrow CO_2 \quad E_0 = 1.02V$$
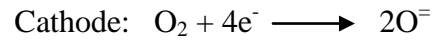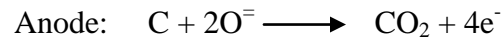
In order to provide intimate ionic contact between the solid fuel and the electrolyte, a molten electrolyte was used to facilitate the transport of ions to and from the fuel surface. Carbon reacts with the reduced oxygen ions to generate electrical power and CO_2.
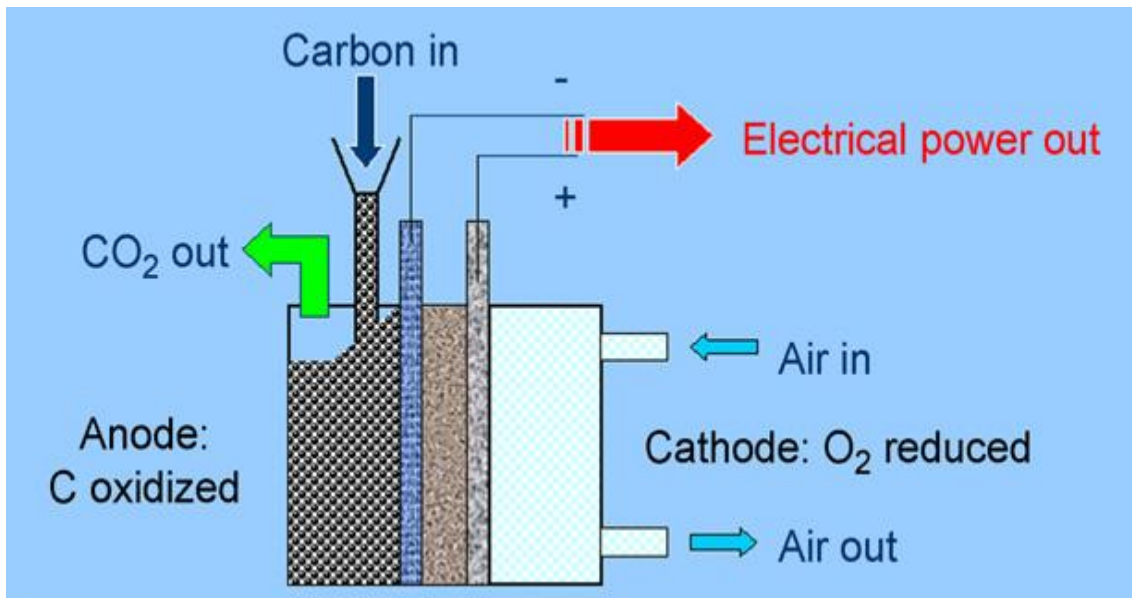
Figure 1.1: Direct Carbon Fuel Cell configuration[5] [D.Cao *et al.* (2010)]

1.3 Classification of Direct Carbon Fuel Cells

Direct Carbon Fuel Cells are classified into three main types.

1.3.1 DCFC with a molten carbonate electrolyte

1.3.2 DCFC with a molten hydroxide electrolyte

1.3.3 DCFC with an YSZ-based solid electrolyte

1.3.1 DCFC with a molten carbonate electrolyte

A mixture of lithium carbonate (Li_2CO_3) and potassium carbonate (K_2CO_3) have been widely used as electrolytes in Molten Carbonate Fuel Cells (MCFC). This electrolyte mixture is also a suitable choice for DCFC because of their high conductivity, suitable melting temperature and good stability in presence of CO_2. Electrochemical reactions involved with molten carbonate DCFC are shown below.

$$\text{Anode: } C + 2CO_3^{2-} \longrightarrow 3CO_2 + 4e^-$$

$$\text{Cathode: } O_2 + 2CO_2 + 4e^- \longrightarrow 2CO_3^{2-}$$

$$\text{Overall: } C + O_2 \longrightarrow CO_2$$
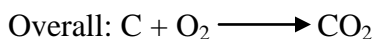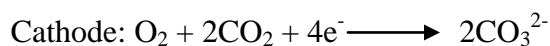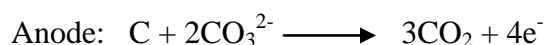
Figure 1.2 shows a tilted DCFC with a molten carbonate electrolyte designed at LLNL by Cooper et $al.$[5] Anode was composed of carbon particle paste with open − foam nickel as the current collector. Cathode was a compressed foam nickel. Activation of the cathode catalyst was done by thermal treatment in air followed by lithiation to form a compact layer of nickel oxide (NiO). Anode and cathode were separated by several layers of Zirconia felt. The cell operates with carbon (anode side) and air/CO_2 mixture (cathode side). Oxygen in the air reacts to produce carbonate ions which oxidizes the carbon particles at the anode. This tilted design allowed the excess electrolyte to drain from the cell thus avoiding flooding of the cathode.
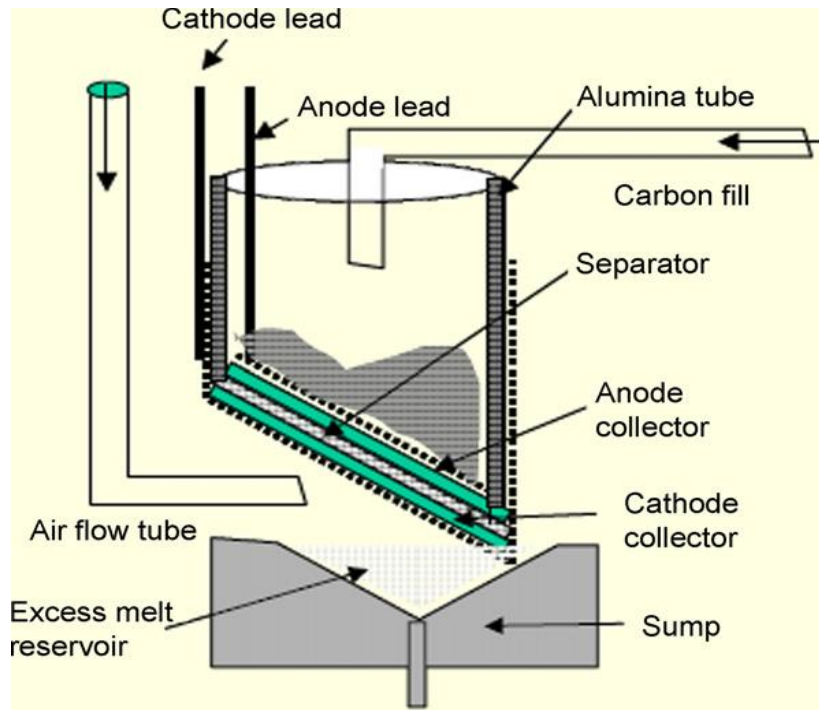
Figure 1.2: Schematic of tilted DCFC with a molten carbonate electrolyte (designed at

Lawrence Livermore National Laboratory)[5] [D.Cao *et al.* (2010)]

This cell operates around 800˚C generating current densities (I) between 58 to 124 mA/cm^2 at a cell voltage of 0.8V.[5-6] However, the major drawbacks include electrode corrosion due to molten carbonate electrolyte; durability and ash build up in the electrolyte.

[5-6]

1.3.2 DCFC with a molten hydroxide electrolyte

After Dr. William Jacques successfully demonstrated the first DCFC, using molten hydroxide as DCFC electrolyte has been discarded for a long time due to the carbonate formation as a byproduct. Compared to molten carbonates, molten hydroxides have a number of advantages such as higher ionic conductivity, higher activity of the carbon

electrochemical oxidation which means a higher carbon oxidation rate and lower overpotential. Electrochemical reactions involved with the molten hydroxide DCFC are shown below.

$$Anode: C + 4OH^- \longrightarrow CO_2 + 2H_2O + 4e^-$$

$$Cathode: O_2 + 2H_2O + 4e^- \longrightarrow 4OH^-$$

$$Overall: C + O_2 \longrightarrow CO_2$$
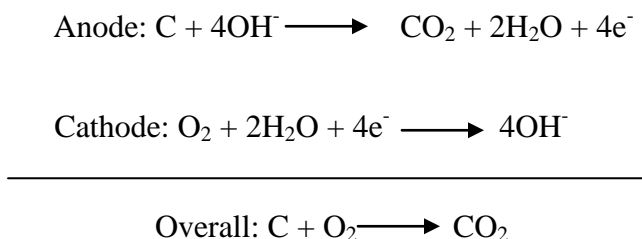
Figure 1.3 depicts the DCFC with a sodium hydroxide electrolyte designed at SARA.[3] A cylindrical graphite rod acts as the anode and the fuel, which was immersed into molten sodium hydroxide electrolyte contained in a cylindrical container. The cylindrical container also acts as the cathode which was generally made of nickel foam lined steel or FeTi because of their good catalytic activity. Humidified air was fed to cell from the bottom of the container in order to reduce the degradation of the electrolyte (mechanism is described in the following paragraphs).

Operation temperature of this DCFC was around 600˚C. Maximum current density (I) obtained was greater than 250mA/cm^2 at an operating voltage between 0.75 and 0.85V. Fabrication cost of DCFC can be brought down as a result of the low temperature operation. All the merits mentioned above can be accomplished only if carbonate formation problem is overcome. The carbonate formation mechanism is shown below.

$$2OH^- + CO_2 \longleftrightarrow CO_3^{2-} + H_2O \text{ ---------- (a)}$$

$$C + 6OH^- \longrightarrow CO_3^{2-} + 3H_2O + 4e^- \text{ ------------ (b)}$$
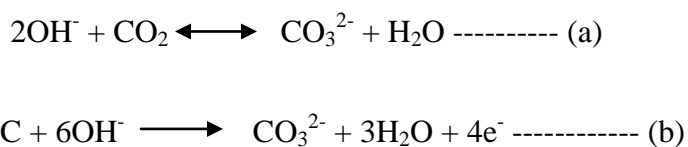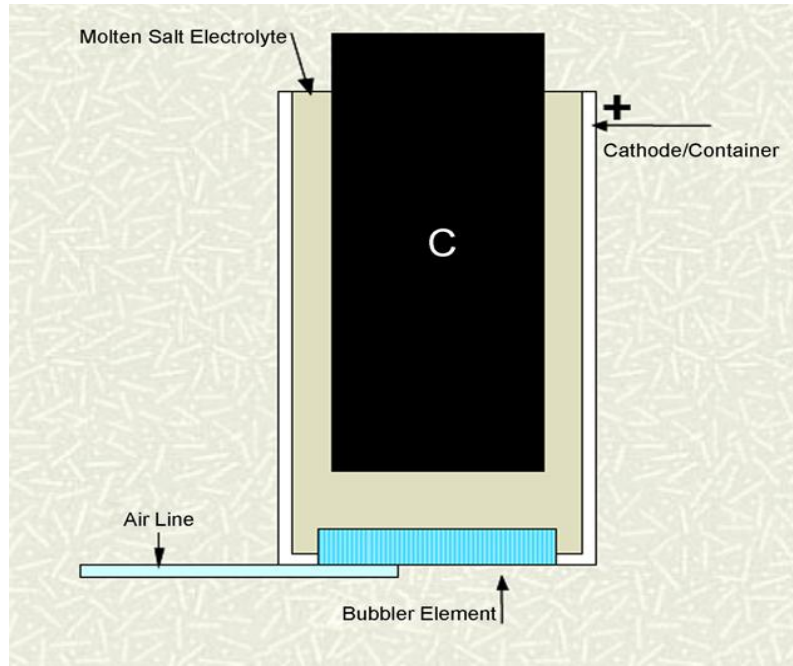
Figure 1.3: DCFC with a molten hydroxide electrolyte (designed at SARA)[3] [S. Zecevic *et al.* (2005)]

$$6OH^- \longleftrightarrow 3O^{2-} + 3H_2O \text{ ------------ (c)}$$

$$C + 3O^{2-} \longrightarrow CO_3^{2-} + 4e^- \text{ ------------ (d)}$$
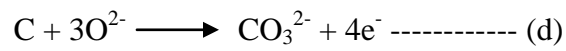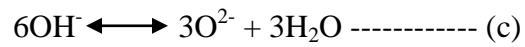
The rate of carbonate formation depends upon O^{2-} and water concentration. Recently this issue has been partially resolved by increasing the water content in the hydroxide electrolyte which causes equations (a) and (c) to shift backward thus decreasing the carbonate formation. However, the major drawbacks include eliminating the carbonate formation and finding suitable materials that sustains the corrosive molten hydroxide electrolyte.

1.3.3 DCFC with an YSZ based solid electrolyte

This DCFC was constructed by merging Solid Oxide Fuel Cell (SOFC) and Molten Carbonate Fuel Cell (MCFC) technologies. The cell consists of a solid Yttria Stabilized Zirconia (YSZ) electrolyte layer along with a liquid electrolyte which comprises a mixture of lithium carbonate (Li_2CO_3), potassium carbonate (K_2CO_3) and sodium carbonate (Na_2CO_3).[5,7]

$$\text{Anode:} \quad C + 2O^= \longrightarrow CO_2 + 4e^-$$

$$\text{Cathode:} \quad O_2 + 4e^- \longrightarrow 2O^=$$

$$\text{Overall:} \quad C + O_2 \longrightarrow CO_2$$
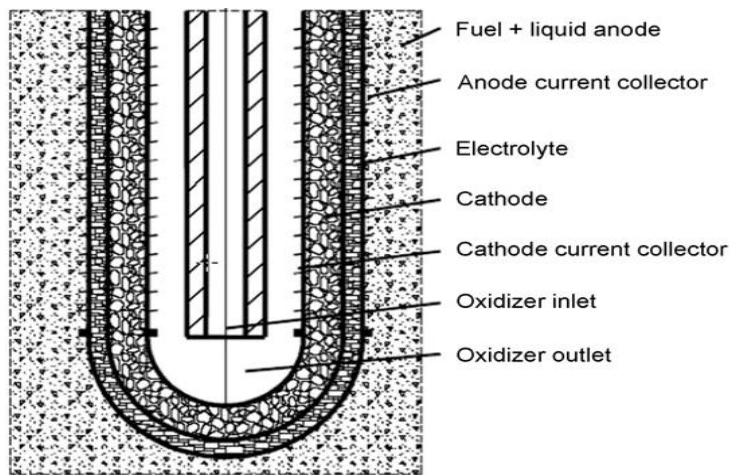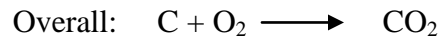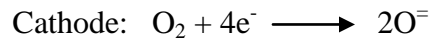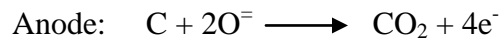
Figure 1.4: Schematic of DCFC with a YSZ based solid electrolyte (designed at SRI)[5]

[D.Cao *et al.* (2010)]

Fig 1.4 shows the schematic of DCFC with a YSZ based solid electrolyte.[5] This DCFC is a U-tube consisting of a metal mesh cathode current collector, Lanthanum

Strontium Manganate (LSM) cathode layer, YSZ electrolyte layer and a metal mesh anode current collector from inner to outer portion of the tube. This tube was immersed into a mixture of carbon particles and carbonate electrolyte mixture. The DCFC was operated in a stirring mode to facilitate better contact between carbon particles and anode current collector to enhance mass transport. Using conventional coal without pretreatment power densities (P) greater than $100mW/cm^2$ were achieved which was comparable to the power densities achieved by commercial MCFC plants operating on natural gas. This DCFC is used as a high energy density battery for military application.[5]

Since DCFC technology is still at the beginning stage, serious efforts are required to address many challenges, both in the fundamental and the engineering aspects. Some of the major challenges include effect of impurities in the carbon fuels on carbon electrooxidation, ash removal from the liquid electrolyte, continuous feeding of solid carbon without interrupting fuel cell operation, materials sustaining the corrosive nature of the electrolytes and scale up of DCFC.

1.4 Significance of electrolyte and fuel in DCFC

Molten electrolytes are required in DCFC in order to provide direct ionic contact between solid carbon fuel and the electrolyte. For solid electrolyte systems such as the Polymer Electrolyte Membrane Fuel Cells (PEMFC) or Solid Oxide Fuel Cells (SOFC), solid fuels such as coal and biomass were converted into gaseous or liquid fuel such as hydrogen, syn-gas or methanol before they can be fed into the fuel cell. In the DCFC, with the usage of molten electrolyte coal can be used directly reducing a lot of effort and capital.

Ample amount of carbon blacks were produced annually by pyrolysis. Electrooxidation of solid carbon releases high energy per unit volume (20 kWh/L) when compared to hydrogen (2.4 kWh/L), methane (4 kWh/L), gasoline (9 kWh/L) and diesel (9.8 kWh/L) used widely in many fuel cells.[8] Pyrolysis production of carbon which can be used in DCFC requires less energy and capital compared to the production of hydrogen rich fuels for MCFC or SOFC. Also, the transportation and handling of solid carbon fuels is relatively easy.

1.5 Experimental objectives

Currently existing liquid electrolyte systems such as molten carbonate, phosphoric acid and hydroxide operate at temperatures around 650˚C or lower. Of all the below mentioned fuel cell systems in Table 1.1, only the molten carbonate system is feasible because its operating temperature is high enough to overcome extremely slow carbon oxidation kinetics. There has been numerous recent activities in this area all around the world.[7-12]

However, even at 650˚C the temperature is still not high enough to provide sufficiently high power density (P) to offset the cost of the system. Furthermore, the cathode feed gas requires a stoichiometric composition of carbon and oxygen to provide optimal performance which further complicates the system.

The obstacles mentioned above could be resolved if a hybrid molten metal oxide fuel cell could be found. This molten metal oxide fuel cell system will provide direct ionic contact to the surface of the solid to allow a solid fuel like coal or biomass derived carbon

to be used directly and at a temperature much higher than that of the molten carbonate
system for higher kinetic rate and power density. Furthermore, anode and cathode reactions

Table 1.1: Fuel cells classified by electrolytes used

Electrolyte (ionic carrier)	Temperature Range	Electrode Reactions (Anode/Cathode)
Alkaline (OH^-)	$\sim 100^\circ C$	$2H_2 + 4OH^- \rightarrow 4H_2O + 4e^-$ $O_2 + 2H_2O + 4e^- \rightarrow 4OH^-$
Phosphoric Acid (H^+)	$\sim 200^\circ C$	$2H_2 \rightarrow 4H^+ + 4e^-$ $O_2 + 4H^+ + 4e^- \rightarrow 2H_2O$
Proton Exchange Membrane (H^+)	$\sim 80^\circ C$	$2H_2 \rightarrow 4H^+ + 4e^-$ $O_2 + 4H^+ + 4e^- \rightarrow 2H_2O$
Molten Carbonate $(CO_3^=)$	$\sim 650^\circ C$	$2H_2 + 2CO_3^= \rightarrow 2H_2O + 2CO_2 + 4e^-$ $C + 2CO_3^= \rightarrow 3CO_2 + 4e^-$ $O_2 + 2CO_2 + 4e^- \rightarrow 2CO_3^=$
Solid Oxide/Molten Oxide $(O^=)$	$\sim 1000^\circ C/\sim 850^\circ C$	$2H_2 + 2O^= \rightarrow 2H_2O + 4e^-$ $C + 2O^= \rightarrow 2CO_2 + 4e^-$ $O_2 + 4e^- \rightarrow 2O^=$

were greatly simplified as shown in Table 1.1. No special treatment of feed gas was
necessary. In this case solid carbon was utilized as fuel and electronic current carrier in the
anode. The oxygen ion current will be carried by the molten electrolyte with reaction
occurring at the coal/liquid electrolyte/gas triple phase boundary.

This work mainly focuses on the following tasks

> Measuring the conductivities of different molten metal oxide electrolytes (Bi_2O_3, V_2O_5, and TeO_2) at various temperatures using AC milliohm-meter and Electrochemical Impedance Spectroscopy (EIS). DC ohmmeter was also used to check electronic conductivity.

> Assembling a hybrid DCFC consisting of an anode immersed in a molten metal oxide electrolyte which is in contact with a solid electrolyte supported cathode.

> Measuring the electrochemical properties of carbon oxidation in these molten metal oxides at various temperatures using the hybrid molten metal oxide DCFC fixture.

CHAPTER 2

Literature Review

Major aspects involved in this research are evaluating the conductivity of different molten metal oxide electrolytes, construction of the hybrid molten metal oxide with its anode immersed in a molten metal oxide electrolyte contacting a solid electrolyte and oxygen cathode, synthesizing composite solid electrolyte/cathode and testing the performance of these molten metal oxides in the developed hybrid DCFC fixture.

2.1 Structure and Electrical properties of the Metal Oxides

The metal oxides used in this research are Bismuth Oxide (Bi_2O_3), Vanadium Pentoxide (V_2O_5), and Tellurium dioxide (TeO_2).

2.1.1 Bismuth Oxide Electrolyte

Researching the existing literature revealed that bismuth oxide (Bi_2O_3) exhibits high oxide ion conductivity and has been proposed as an efficient electrolyte material for SOFC and oxygen sensor applications.[13]

2.1.1.1 Phases involved with Bi_2O_3

Polymorphism of Bi2O3 has been the subject of investigation for the past 100 years. Four polymorphs of Bi_2O_3 have been reported in literature namely α, β, γ and δ.[13-14] When solid bismuth oxide was heated from room temperature it transforms from monoclinic α phase to cubic δ phase around 730˚C. The δ phase was also found to be stable until its melting point

i.e. 825˚C. Cooling down from high temperature δ phase resulted in large hysteresis in conductivity and formation of two intermediate metastable phases β and γ. The tetragonal β phase and body centered cubic γ phase occur approximately around 650˚C and 640˚C respectively. When the cooling rate is low γ phase exists until it reaches room temperature. Figure 2.1 depicts different phase transitions involved with bismuth oxide.
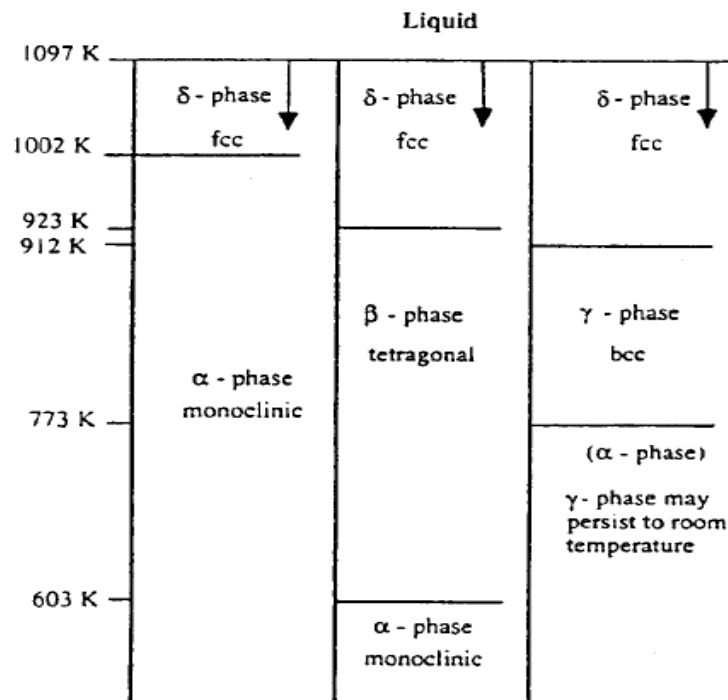
Figure 2.1: Stable and metastable phases involved with Bi_2O_3[13] [N. M. Sammes *et al.* (1999)]

2.1.1.2 Structure of δ-Bi_2O_3

δ-Bi_2O_3 exhibits high conductivity because of its defect fluorite structure.[13-15] Three models for the structure of δ-Bi_2O_3 have been proposed in literature by Gattow and Schroder, Sillen and Willis. Figure 2.2 shows the proposed models for δ-Bi_2O_3.[14] Sillen reported that

$\delta\text{-}Bi_2O_3$ has a cubic structure which was related to fluorite structure but with ordered defects in the oxygen sublattice as shown in Figure 2.2.[14] Gattow and Schroeder with using X-ray diffraction described the structure of $\delta\text{-}Bi_2O_3$ as face centered cubic (fcc). The ordered defect sub-lattice described by Sillen was rejected by Gattow and Schroeder who preferred to describe the system with statistical occupation of the sites in the oxygen sub-lattice (75 % of the oxygen sublattice sites are filled). Later Willis with the help of neutron diffraction
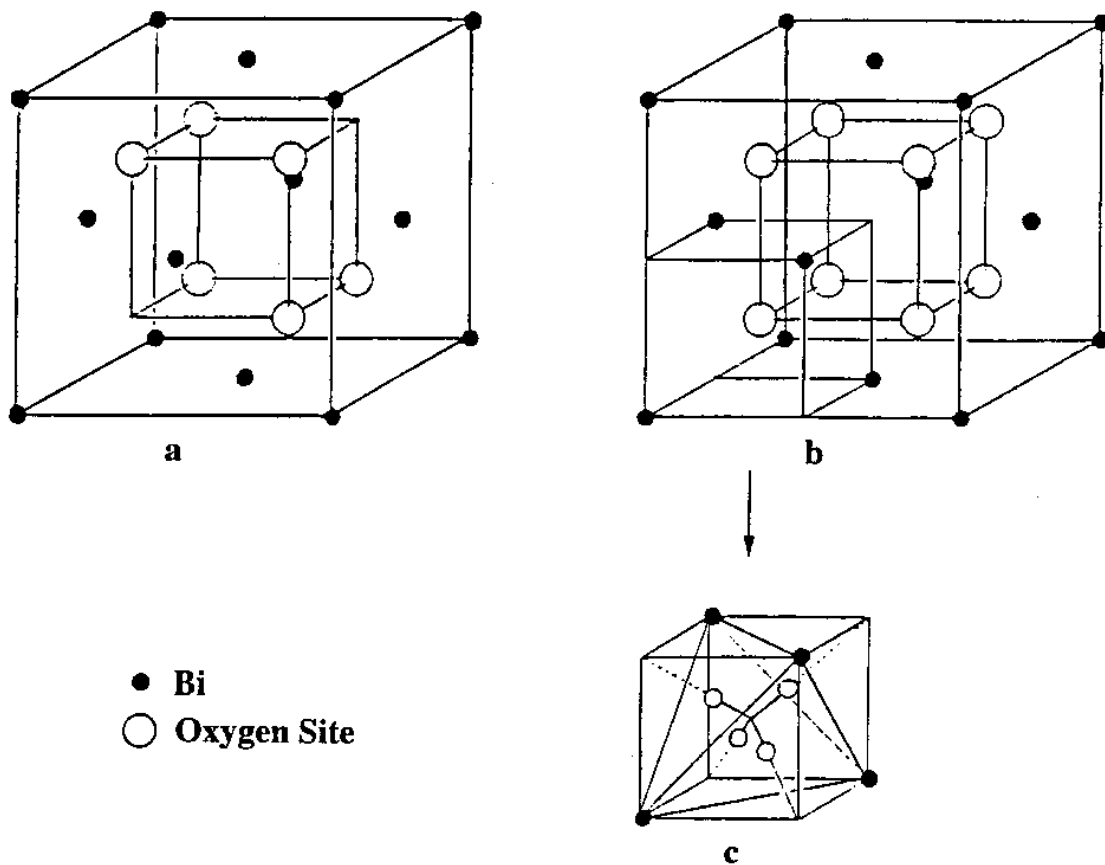
Figure 2.2: a) Sillen model   b) Gattow model   c) Willis model[14] [P. Shuk *et al.* (1996)]

stated that oxide ions occupy the sites statistically with an occupancy factor of 3/16. Similar work was done by Battle *et al.* who also approved that δ-Bi$_2$O$_3$ has a defective fluorite structure in which 43 % of the regular oxide ion sites are randomly occupied.[16] The vacant sites in the fluorite type lattice leads to high oxide ion mobility which explains the exceptionally high ionic conductivity of δ-Bi$_2$O$_3$.

2.1.1.3 Electrical properties of Bi$_2$O$_3$

Mixed conductivity of α, β, γ and δ phases were systematically measured by Harwig.[17] Harwig's measurement included repeated heating and cooling runs as shown in Figure 2.3.
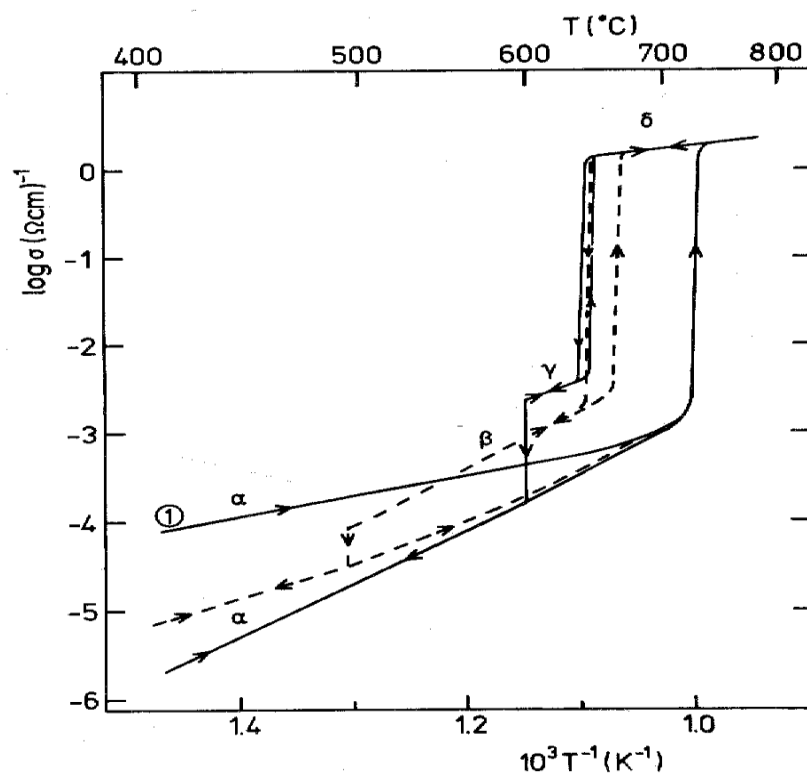
Figure 2.3: Mixed conductivity of Bi$_2$O$_3$ as a function of temperature[17] [H. A. Harwig *et al.* (1978)

There was a sharp rise in conductivity by three orders of magnitude when Bi_2O_3 transformed from α to δ phase at 729˚C approximately. This jump in conductivity could be attributed to the highly disordered state of δ-Bi_2O_3. During the cooling process, a hysteresis of 80-90˚C was observed as a result of formation of the metastable β and γ phases. Harwig and Gerards determined the conductivity of β, γ and δ phases to be predominantly ionic with the conductivity of δ phase being three orders of magnitude higher than the intermediate phases. Also, they concluded that the α phase was electronically conductive with holes being the majority charge carriers.

Major characteristic of an electrolyte is its ionic conductivity. Comparison of Bi_2O_3 with other solid metal electrolytes has been shown in literature.[18-19] From the results Bi_2O_3
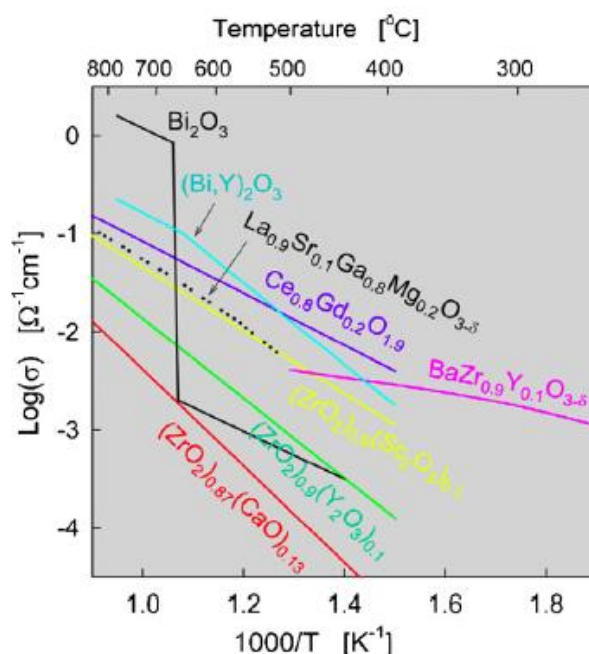
Figure 2.4: Comparison of conductivities of different solid metal electrolytes[19] [R. Chockalingam *et al.* (2008)]

was proven to be a suitable alternative to other solid metal oxides such as $Bi_2Y_{0.9}Cu_{0.1}O_{5.35}$, $Bi_{0.8}Er_{0.2}O_{1.5}$, $Zr_{0.77}Y_{0.23}O_{1.885}$, etc. Figure 2.4 shows a graph comparing the conductivities of different solid metal electrolytes.[19]

Until now bismuth oxide (Bi_2O_3) was doped with materials such as yttria, lanthanum etc to stabilize below its melting point facilitating its usage as a solid electrolyte in Solid Oxide Fuel Cells (SOFC).[13-14] Present study involves the proposed use of Bi_2O_3 as a potential liquid electrolyte for a DCFC system.

2.1.2 Vanadium Pentoxide Electrolyte

Vanadium Pentoxide (V_2O_5) is the most stable and common compound of vanadium which is the 22nd most abundant element in the earth's crust. V_2O_5 is used as a catalyst in different industrial processes. Major applications of V_2O_5 include production of ferrovanadium, sulfuric acid and maleic anhydride.

2.1.2.1 Crystal structure of V_2O_5

From the existing literature crystal structure of V_2O_5 was known to be orthorhombic. Figure 2.5 shows the crystal structure of V_2O_5. Smaller blue and larger brown circles represent vanadium atoms and bridge oxygens respectively. Larger orange circles represent chain oxygens. Vanadium Pentoxide is a non stoichiometric compound. Heating it results reversibly in the loss of oxygen leading to oxygen vacancies. These vacancies can be replenished by incorporating oxygen ions or by diffusion of oxygen ions from the bulk which results in the regeneration of the active sites. Due to the existence of channels that

promote diffusion of oxygen, regeneration of the active sites was very short. This shows that the dead time of the active sites was short resulting in high catalytic activity.
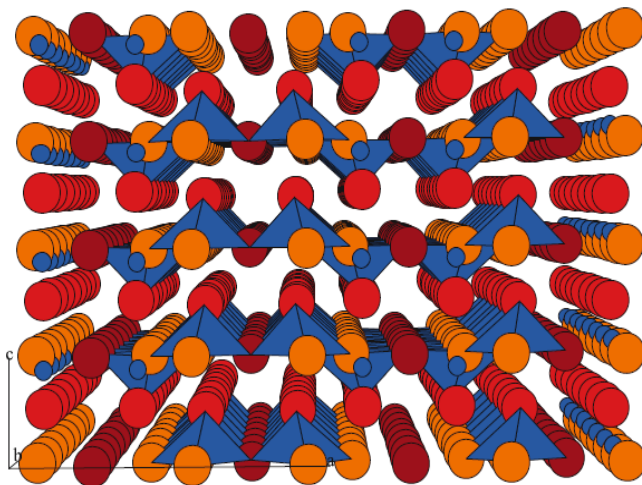
Figure 2.5: Crystal structure of V_2O_5[20] [R. B. Darling *et al.* (2009)]

2.1.2.2 Electronic applications of V_2O_5

V_2O_5 in powder form was insoluble in water but at elevated temperatures it was soluble.[20] This high aqueous solubility of V_2O_5 allows its use in solution-based microfabrication methods such as sol-gel fabrication process.[20-22] Initially V_2O_5 was melted in a ceramic crucible to its melting point after which deionized water was added with continuous stirring resulting in an orange colored gel. This gel can applied to substrates by different coating methods following by dehydration and annealing thus producing nano V_2O_5 films. These fabrication processes offer exciting new possibilities in glass and ceramic fabrication.

Another major application of V_2O_5 is in the field of electrochromism.[21-22] Electrochromic effects are reversible changes in optical properties as a result from the

injection or extraction of a charge exhibited by many transition metal oxides. Research involved with electrochromism mainly explores the mechanism to create efficient windows with adjustable reflectivity for use in buildings, automobiles and space satellites. Electrochromic effects in V_2O_5 were found by injection of a charge from Atomic Force Microscopy (AFM) tip. Iwanaga *et al* used a new type of AFM nanolithography in which the patterns were bound for many months.[20] Figure 2.6 shows the reflectivity spectrum of V_2O_5 deposited onto a chromium layer on a silicon substrate.[20] As shown in Figure 2.6 AFM nanolithography produces stable color changes along with high contrast changes which shows that V_2O_5 is a suitable metal oxide for electrochromic applications. Furthermore, V_2O_5 was doped with sodium in order to create a regular, periodic pattern to
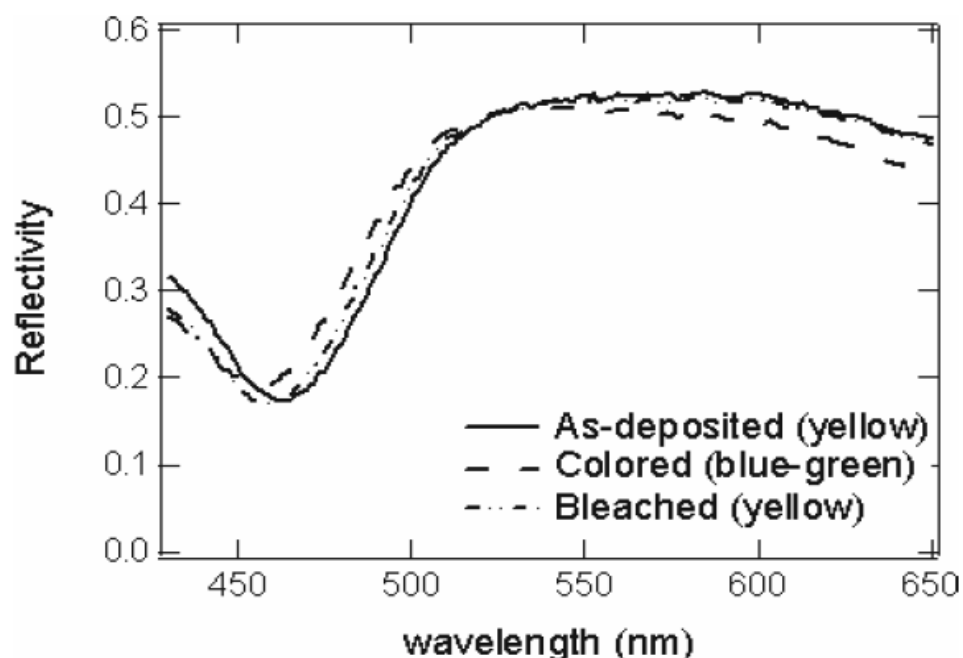
Figure 2.6: Reflectivity spectrum of V_2O_5 using AFM nanolithography[20] [R. B. Darling *et al.* (2009)]

form a sodium vanadium bronze phase.[22] This phase was mainly exploited for new interconnect and addressing schemes in nano electronics.

In the recent years V_2O_5 is considered as a favorable transition metal oxide for microelectronic and sensing applications. Currently sodium vanadium bronzes are being investigated to create a new generation of biosensors and bioassays.[20]

2.1.2.3 Electrical properties of V_2O_5

Electrical conductivity of both solid and liquid V_2O_5 has been reported in literature. Many authors have reported the conductivity data of solid V_2O_5.[23-24] Figure 2.7 shows the ac (mixed) and dc (electronic) conductivity of V_2O_5 measured between 90- 350°K by Haemers
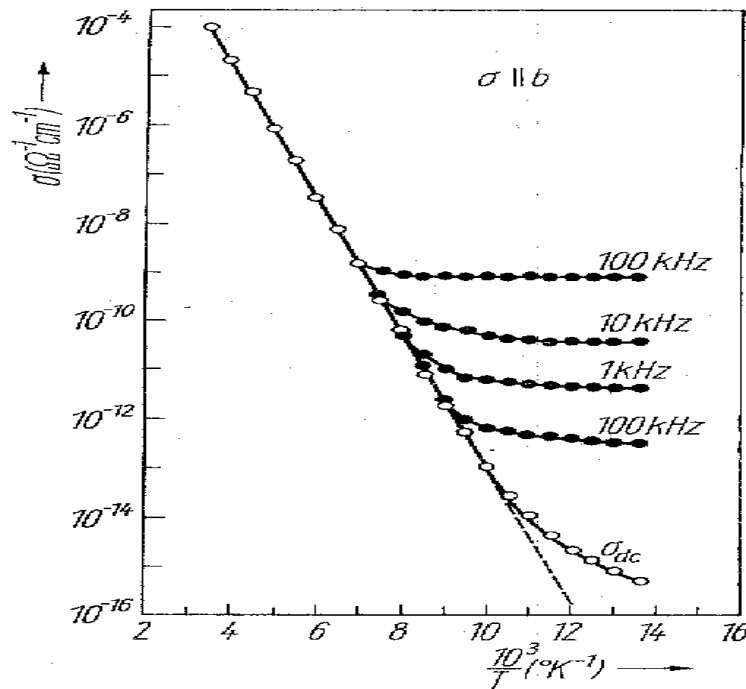
Figure 2.7: AC and DC conductivity of V_2O_5 crystal[23] [J. Haemers *et al.* (1973)]

et al.[23] Solid V_2O_5 crystals have been used for the conductivity measurements. Also, a model based on the theory of amorphous semiconductors has been developed to fit the experimental data in order to investigate the mechanism of electrical conduction in solid V_2O_5. Based on the results it was found that below 140°K conduction was mainly due to hopping of electrons between defect sites situated near the Fermi level and between 140 and 350°K conduction was due to hopping of electrons along the vanadium chains.

Mixed conductivity of molten V_2O_5 also has been reported in literature.[25-27] Figure 2.8 shows the electrical conductivity of V_2O_5 between 670-1000°C measured by Kerby and
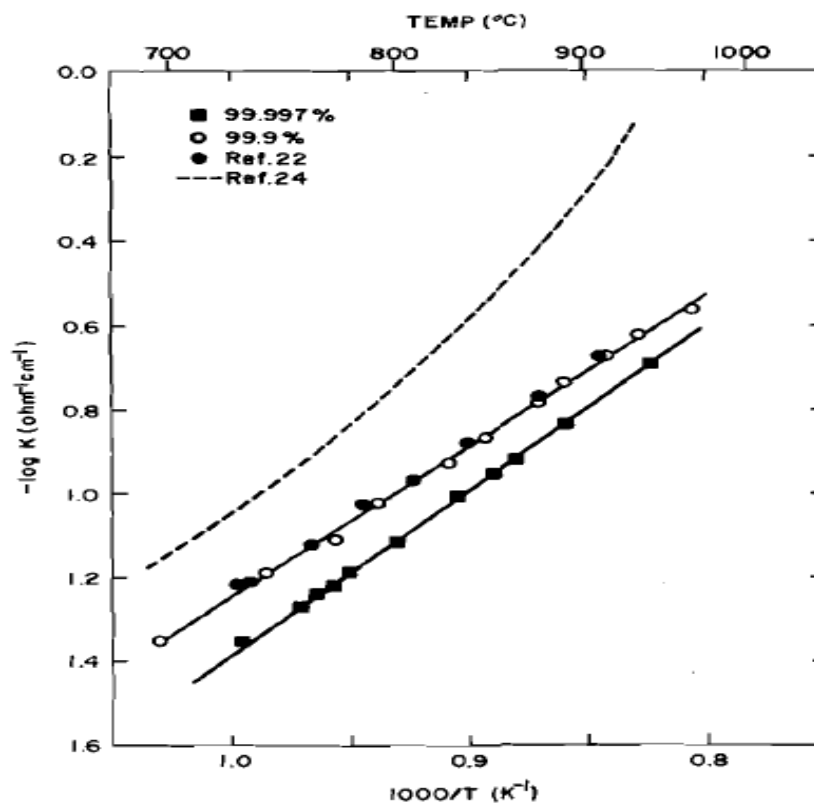
Figure 2.8: Electrical conductivity of molten V_2O_5[25] [R. C. Kerby *et al.* (1972)]

Wilson in 1972.[25] A gold-palladium cylindrical crucible was used to melt the solid V_2O_5. Two gold-palladium electrodes were dipped inside the crucible in order to carry out the conductivity measurements. This conductivity data was compared with data reported by Alleresma *et al.*[27] (Ref 22 in the graph) and Pantony *et al.*[26] (Ref 24 in the graph). Conductivity data procured by Kerby and Wilson and Pantony *et al* didn't match because of the different grade of V_2O_5 used for the measurement. Based on the results it is found that V_2O_5 exhibits predominant n-type conduction between 670-1000˚C.

2.1.3 Tellurium dioxide electrolyte

Tellurium is one of the least abundant metals available in earth's crust. Tellurium dioxide mainly exists in two forms, yellow orthorhombic tellurite (β-TeO_2) and colorless tetragonal paratellurite (α-TeO_2). However, most of the research has been conducted on studying the physical properties and crystal structure of paratellurite (α-TeO_2).[28-33] Crystalline TeO_2 is mainly used in glass applications, acousto-optic devices and ultrasonic generators because of its remarkable dielectric, optic and electro-acoustic properties.[28-33]

2.1.3.1 Crystal structure of TeO_2

At ambient conditions tellurium dioxide exhibits two main polymorphs, paratellurite (α-TeO_2) and tellurite (β-TeO_2). [28-29] Backbone of both the structures mainly comprises of distorted bipyramid structured TeO_4. As shown in Figure 2.9 tellurium atom is surrounded by four neighboring oxygen atoms, two of them being in axial position and other two in equatorial.[28] Figure 2.10 shows the crystal structures of α and β-TeO_2.[28] Each oxygen atom
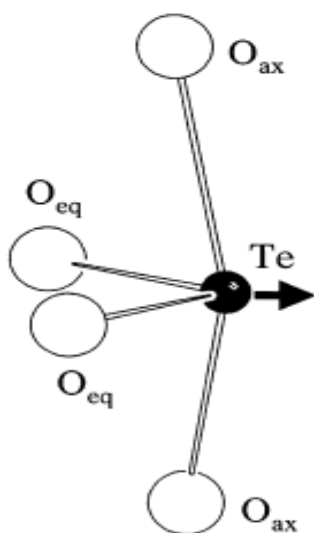
Figure 2.9: Structure of TeO_4[28] [A. P. Mirgorodsky *et al.* (2000)]

in these structures was coordinated to two tellurium atoms forming a highly asymmetric bridge.
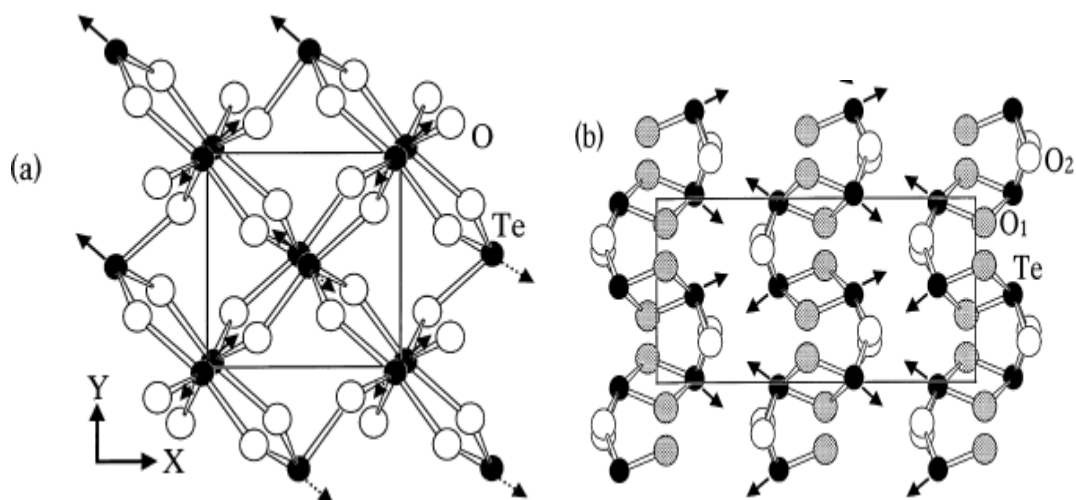
Figure 2.10 Crystal structures of a) α-TeO_2 and b) β-TeO_2[28] [A. P. Mirgorodsky *et al.* (2000)]

The arrow marks in both structures indicate the lone pair of electrons of tellurium atom. In the three dimensional structure of α-TeO$_2$ visualized in Figure 2.10a, the TeO$_4$ units constitute by sharing the corners. In the β-TeO$_2$ structure, the TeO$_4$ units alternatively share corners and edges forming a two dimensional network. In the above structures symmetrical Te-O-Te bridges were present in which the bonds were chemically identical.

Recently two more polymorphs of TeO$_2$ were identified namely γ and δ TeO$_2$. γ-TeO$_2$ was formed when the TeO$_2$ crystal is heated to 390˚C and annealed for 24 hours which is orthorhombic. δ-TeO$_2$ was formed when TeO$_2$ samples containing traces of tungsten oxide are annealed at 350˚C for 24 hours which has fluorite related structure. Currently crystal structures of these polymorphs are being investigated.[28-29]

2.1.3.2 Applications of TeO$_2$

Primary application of TeO$_2$ is in glass industry. Pure TeO$_2$ is used as a network former in glass industry. It was doped with several metal oxides such as titanium dioxide, vanadium pentoxide and silicon dioxide etc. in order to improve the mechanical strength and durability of the glass material.[29-31] Another major application of TeO$_2$ is in the area of acousto-optics. Acousto-optic modulators are mainly used for amplitude modulation of laser light. For near and infra red laser lines, TeO$_2$ based modulators were used because of their high diffraction efficiency and ability to form glass with high refractive indices.[29-30]

2.1.3.3 Electrical properties of TeO$_2$

Electrical conductivity of TeO$_2$ has been reported in literature by a few authors.[34-35] Most

of the conductivity data reported in literature were below the melting point of TeO_2, i.e. 733˚C. Figure 2.11 shows the dc (electronic) conductivity of TeO_2 between room temperature and 700˚C measured by Hartmann et al.[34] Conductivity measurements were carried out using rectangular crystals of surface area 16mm[2] and thickness 2mm. The faces
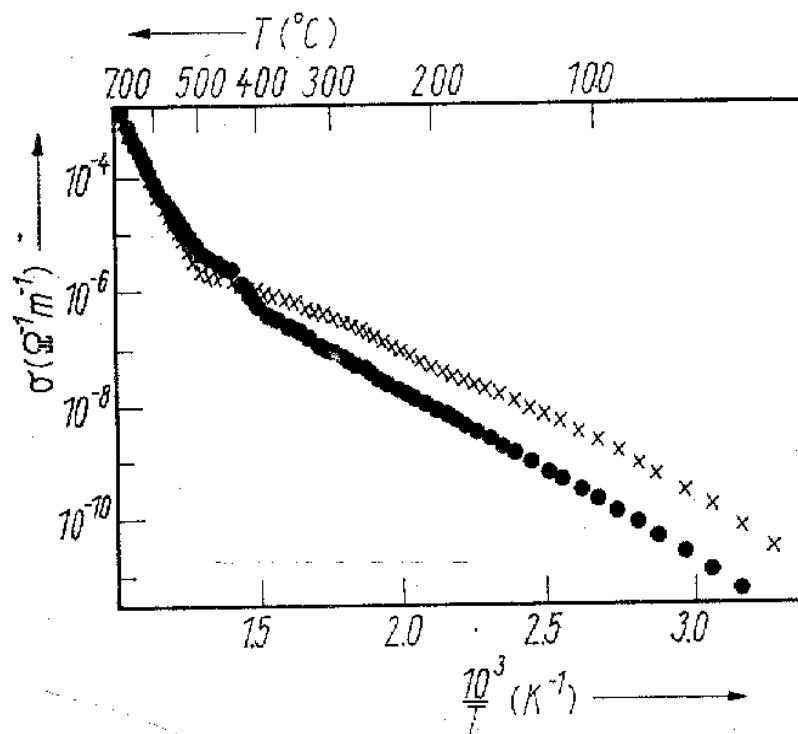
Figure 2.11: DC conductivity of TeO_2[34] [E. Hartmann et al. (1982)]

of these crystal samples were either covered with platinum or graphite paste in order to connect the probes. A vibrating capacitor electrometer was used to carry out the measurements. The two curves in the graph correspond to two different orientations of the TeO_2 crystals.

AC conductivity measurements also have been reported in literature. Figure 2.12 shows the

comparison of ac and dc conductivity of TeO_2 crystals.[35] These measurements were made
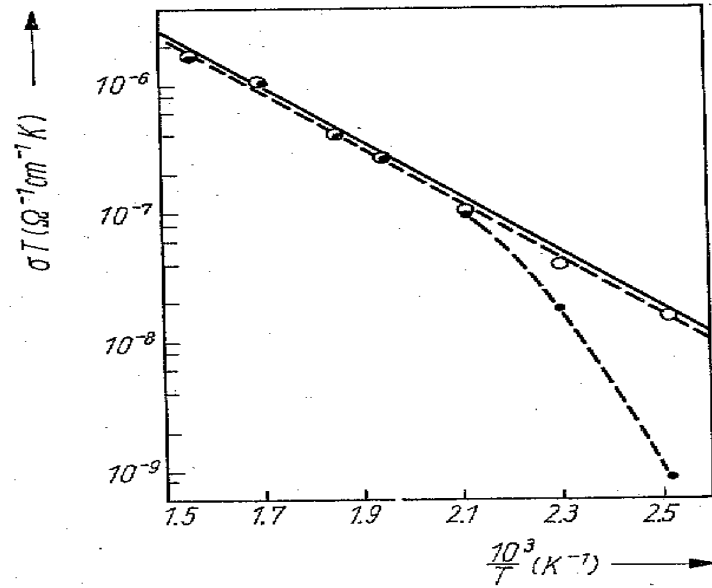
Figure 2.12: Comparison of AC and DC conductivity of TeO_2[35] [H. Jain *et al.* (1981)]

using plate like crystals of area $1cm^2$ and thickness 1-1.5mm. Gold electrodes were vacuum deposited to carry out the measurements. Based on the conductivity data in literature, TeO_2 was identified as a predominant ionic conductor with little or no electronic conduction between room temperature and 350˚C and a mixed conductor at temperatures above 350˚C with ionic conductivity still being dominant.[34-35]

2.2 Fabrication methods of composite electrolyte/cathode in a DCFC

2.2.1 Significance of solid electrolyte/cathode in a DCFC

A hybrid DCFC fixture has been used in this work in case the molten electrolytes used in them were mixed conductors (ionic and electronic). Figure 2.13 shows the arrangement of

hybrid DCFC. As shown in the Figure 2.13 a pure solid state ionic conductor i.e. YSZ was placed between the cell cathode and the molten electrolyte in order to prevent electrical shorting of the carbon anode and the molten electrolyte. LSM cathode was used to reduce
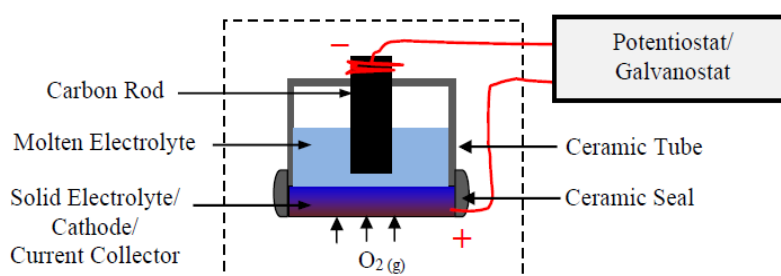
Figure 2.13: Hybrid Direct Carbon Fuel Cell (DCFC) configuration

oxygen in the air to oxygen ions. LSM was the primary choice for the cathode because of its chemical compatibility with solid YSZ electrolyte.[52] LSM has a similar coefficient of thermal expansion as YSZ which makes composite YSZ/LSM substrates a favorable choice, particularly at high operating temperatures.[52] Fabrication of the composite YSZ/LSM electrolyte/cathode discs will be discussed in the following sections.

2.2.2 Steps involved in preparation of composite YSZ/LSM discs

Major steps involving the preparation of composite YSZ/LSM electrolytes are listed below. These below specified steps are discussed in detail in the following sections.

- Initially 8 % YSZ powder was used to prepare solid YSZ discs. Techniques involved in this process were tape casting (aqueous and non aqueous), slip casting and direct compression.

- Second step involves preparation of LSM paste using 20 % LSM powder.

28

- Next step involves coating of LSM paste over solid YSZ discs using screen printing or plasma spraying.

- Finally co-sintering of composite YSZ/LSM material was carried in a high temperature furnace.

2.2.3 Preparation of solid YSZ discs

Fabrication of YSZ discs is done using tape casting, slip casting or direct compression. Out of these three techniques tape casting and direct compression were the most widely used ones.

Preparation of YSZ discs by means of tape casting involves the following steps.[36-44]

- Initially YSZ slips were prepared by deagglomeration of 8 % YSZ powder with dispersant, solvent and binder (Widely used dispersants, solvents and binders are shown in Table 2.1 below).

- These slips were cast manually on a Mylar film using doctor's blade and dried at room temperature up to constant weight.
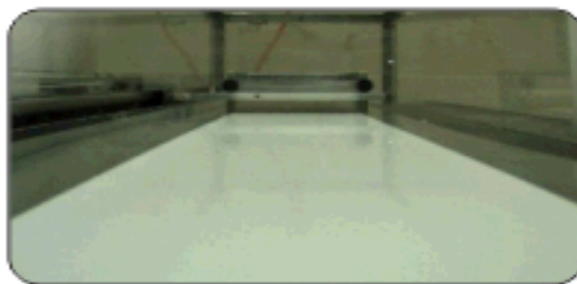
Figure 2.14: Casting of tape on a mylar film using doctor's blade [Ref. 37]

- Density and thickness of the tape were measured before they are sintered in a high temperature furnace.

- Sintering of these tapes was done at a ramp rate of 1˚C/min until 1000˚C in order to burn out the organic additives and 5˚C/min between 1000-1500˚C. These tapes were treated for 2 hours at 1500˚C.

Different combinations of binders, dispersants, solvents and poreformers used in tape casting are specified in Table 2.1.[36-44] However, there was no need of adding poreforming agent in the slurry since dense YSZ electrolyte was used in the DCFC fixture.

Table 2.1: Different materials used in tape casting

Dispersant	Binder	Solvent	Poreformer
Ammonium Polyacrylate	Acrylic latex emulsion		Cornstarch
Fish oil	Polyvinylbutyral and dibutylpthalate	Isopropanol	
Hydroxypropyl Cellulose		Isopropanol	Polymethylmethaacrylate
Distilled water	Acrylic latex emulsion		Graphite or Polystyrene

In the recent years tape casting was modified by substituting volatile and toxic organic binders with water soluble binders. This method is known as aqueous tape casting. Water soluble binders mainly used in aqueous tape casting were Polyvinyl alcohol (PVA) and Polyvinylpyyrolidone.[40-44] Also, drying of the tapes involves two steps in aqueous tape casting. Initially slips were de-aired for several minutes under mechanical vacuum and then vacuum vessel was backfilled with saturated air to prevent skin formation on the slip.[42]

Organic solvents and binders used in traditional tape casting are harmful to the environment because of their volatility and toxicity. Although, the use of aqueous tape casting can eliminate this problem, there are some hindrances arising in this process such as low strength of water soluble binders, slow drying rate of cast tapes and low density of the dried tape (green tape). However, these obstacles can be overcome by controlling the tape processing parameters and selecting suitable slurry additives. Also, better porosity control

(a)   (b)
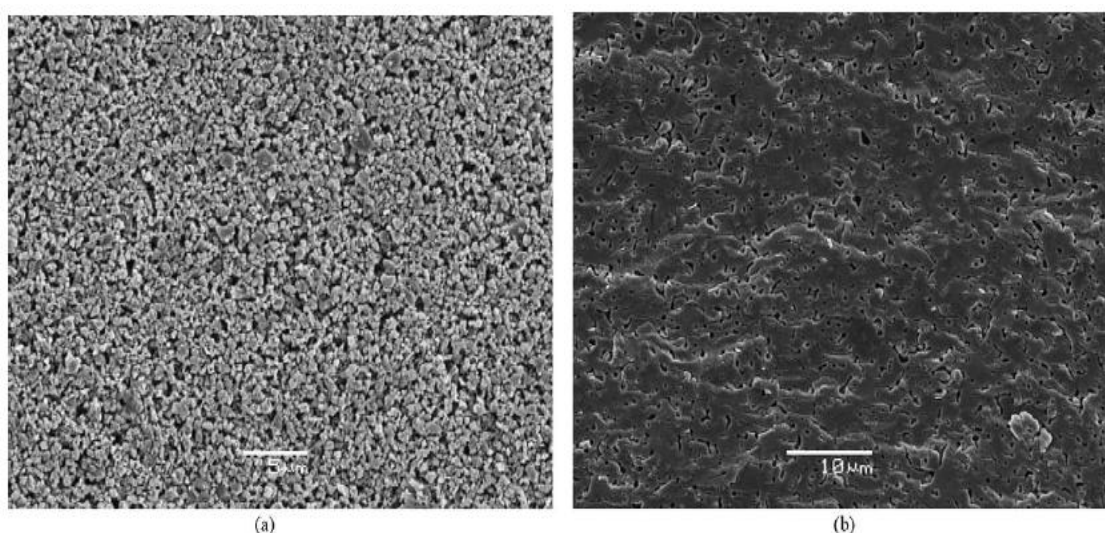
Figure 2.15: SEM images of a) Green tape (dried tape) and b) Sintered tape fabricated by aqueous tape casting[42] [M. P. Albano *et al*. (2006)]

can be obtained using aqueous tape casting when compared to non aqueous tape casting. Figure 2.15 shows the SEM images of green tape and sintered tape obtained from literature.[42]

One of the other widely used methods for fabricating dense YSZ electrolyte discs was direct compression.[46,50] This process is very easy and reliable. In this process fine nano

YSZ powder was compressed into discs using a hydrostatic press. These discs were then sintered at a heating rate of 4˚C/min until 1400-1500˚C. They were held for 2 hours at 1400-1500˚C and then cooled down to room temperature. Figure 2.16 shows the SEM images of sintered YSZ electrolyte discs at 1400 and 1500˚C.[46]
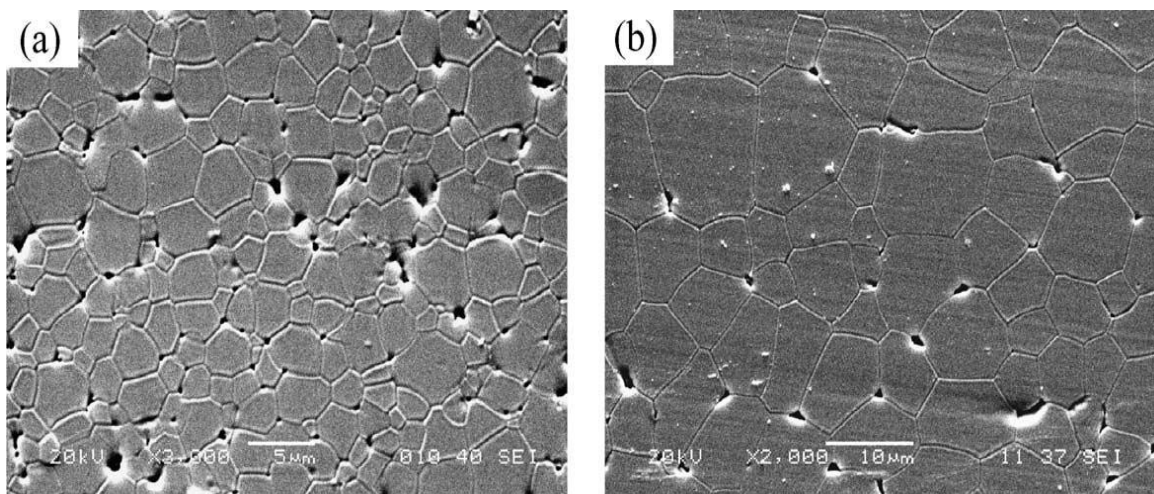
Figure 2.16: SEM images of a) YSZ electrolyte sintered at 1400˚C and b) YSZ electrolyte sintered at 1500˚C[46] [X. J. Chen *et al*. (2004)]

2.2.4 Preparation and coating of LSM ink on YSZ substrates

LSM ink was prepared by mixing LSM powder with solvent, dispersant binder and pore forming agent (materials used are shown in Table 2.1). Prepared LSM paste was coated on the YSZ substrate using different techniques such as screen printing, plasma spraying, and spray pyrolysis etc.[46-52]

2.2.4.1 Coating of LSM ink by screen printing

Screen printing is the widely used technique for printing LSM ink on YSZ substrates. This

technique is efficient and cost effective. In this process LSM ink was printed by using a brush onto the YSZ substrate and then co-sintered at 1400°C.[51] Main disadvantage in this process was the degradation of the performance of composite YSZ/LSM substrate due to formation of $SrZrO_3$ and $La_2Zr_2O_7$ complexes at the interface.[49]

2.2.4.2 Coating of LSM ink by plasma spraying

In plasma spraying LSM powder was introduced into a plasma jet where the temperature is around 10,000°K and sprayed onto the YSZ substrate. Figure 2.17 depicts the plasma spraying mechanism.[47]
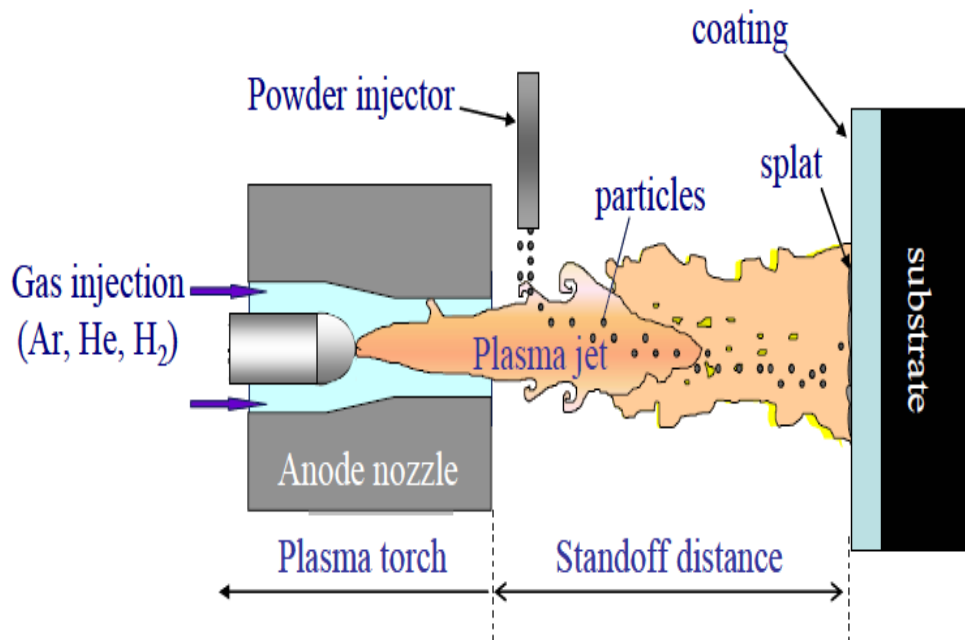
Figure 2.17: Mechanism of Plasma Spraying[47] [K. Wittmann-Teneze *et al*. (2009)]

LSM powder was introduced in to the flame (Ar, He, H_2) and sprayed onto the YSZ substrate placed at a certain distance from the anode nozzle. Major advantage of plasma

spraying was that there was no need to fire at elevated temperature, which prevents the undesirable complex formation.[46-49]

2.2.4.3 Coating of LSM ink by spray pyrolysis

Spray pyrolysis is one of the most cost effective techniques for deposition of thin films on solid electrolyte substrates. Advantages include deposition of cathode at a low temperature when compared to plasma spraying, i.e. around 600˚C, and its ability to control the shape, size and composition more effectively. Figure 2.18 shows the schematic of spray pyrolysis
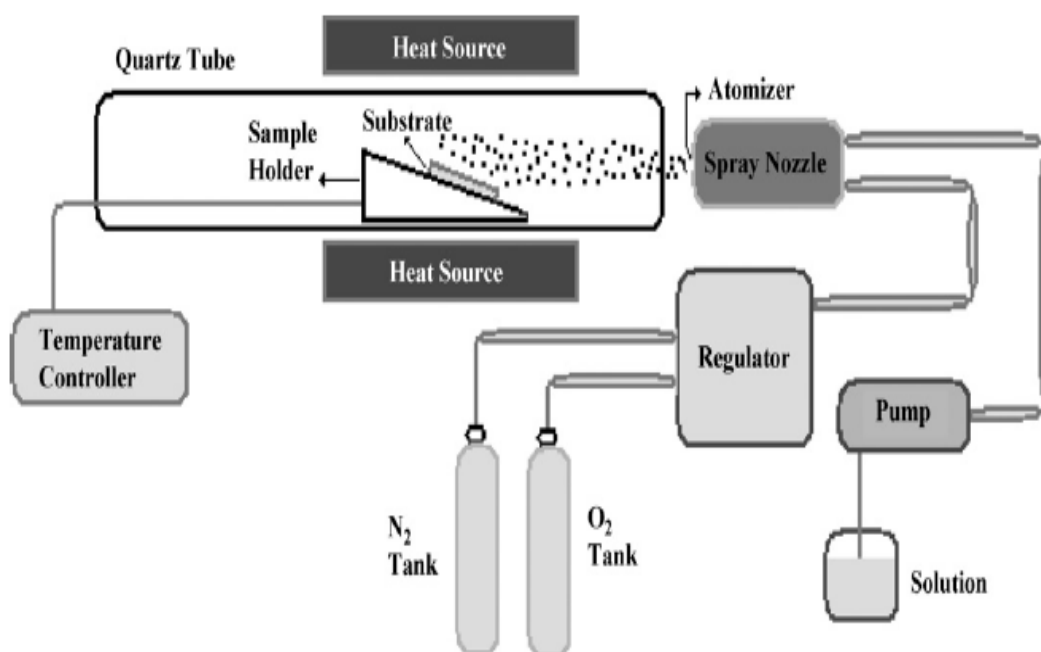
Figure 2.18: Schematic showing spray pyrolysis mechanism[50] [H. A. Hamedani *et al*. (2008)]

process.[50]In this process precursor solution comprising cathode material was introduced into the vaporizer (spray nozzle) by means of a pump. As the precursor solution hits the

hits the heated substrate it undergoes pyrolytic decomposition reducing it to atomized droplets. These precursor particles were sprayed on to the electrolyte substrate using nitrogen and oxygen as carrier gases. Temperature controller was used to adjust the substrate temperature, and regulator controls the carrier gas flow rate.

2.2.5 Co-sintering of composite LSM/YSZ substrate

After coating the LSM ink over YSZ substrate, they were co-sintered together for the porous LSM cathode to adhere on the YSZ substrate. Porous LSM over YSZ substrate was desired because a triple phase boundary (where electrolyte, air and electrode meet) is required for the electrochemical reaction to take place in a DCFC. Figure 2.19 shows the triple phase boundary at the LSM/YSZ interface.[50] The microstructure of the cathode
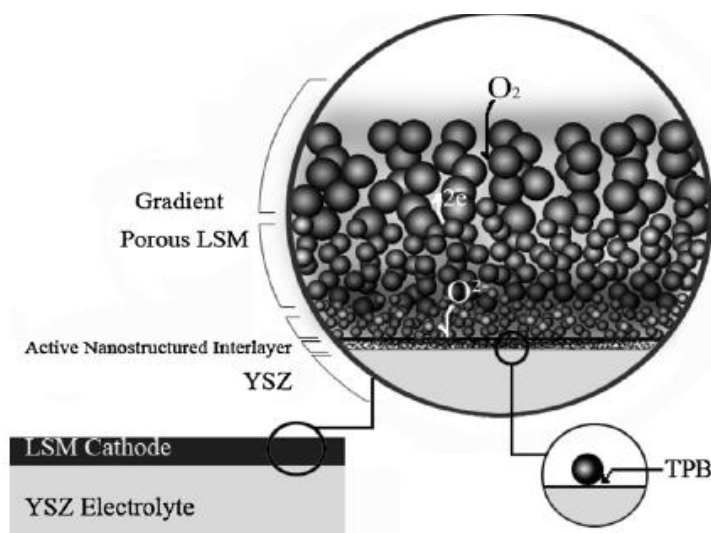
Figure 2.19: Schematic of porous LSM/dense YSZ substrate depicting the triple phase boundary concept[50] [H. A. Hamedani *et al*. (2008)]

requires sufficient porosity for the oxygen supply while providing electrochemical reaction sites for oxygen reduction as well as a way for the electrons from the interface to the surface of the cathode.

Figure 2.20 shows the SEM images of the LSM/YSZ interface for different techniques such as screen printing, plasma spraying and spray pyrolysis.[46-52] Based on these SEM images we can see that proper adhesion was achieved using plasma spraying, spray pyrolysis and screen printing. However, plasma spraying and spray pyrolysis have the advantage of skipping the co-sintering at elevated temperatures. Reducing the co-sintering temperature by carefully choosing the additives in preparing LSM ink makes screen printing the most efficient technique of all the three techniques.

(a) (b) (c)
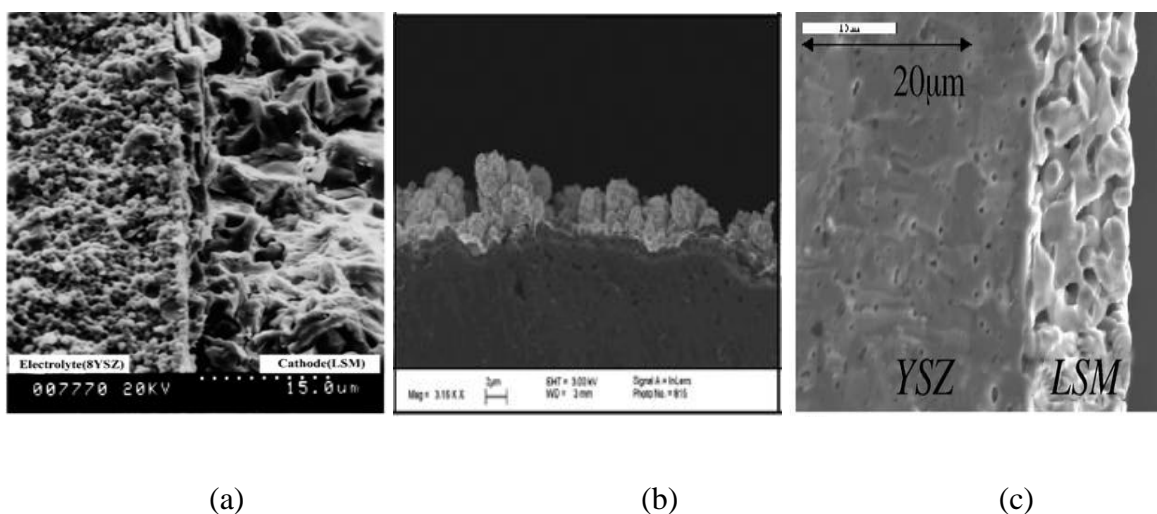
Figure 2.20: SEM images of the interface of LSM/YSZ substrates prepared by a) plasma spraying[49] [H. Nie *et al*. (2002)] b) spray pyrolysis[50] [H. A. Hamedani *et al*. (2008)] and c) screen printing[51] [J. R. Smith *et al*. (2006)]

CHAPTER 3

Conductivity studies of molten metal oxide electrolytes

3.1 Introduction

The first half of this research mainly focuses on proposing suitable molten metal oxide electrolytes based on their conductivity measurements. Three metal oxides that could form stable liquids in air have been identified based on their ionic properties, melting point, and stability. They are bismuth oxide (Bi_2O_3), vanadium pentoxide (V_2O_5), and tellurium dioxide (TeO_2) respectively. Although, part of the conductivity data of these metal oxides was shown in literature, most of the conductivity measurements were carried out using two probes which is not very accurate. Also, there is not much conductivity information available at the molten range of these metal oxides. This study proposes using a more efficient four probe measurement approach with the aid of EIS in order to study the electrical properties of these metal oxides with strong emphasis on their molten range.

Conductivity measurements were made using AC milliohm-meter (HP 4338A) and DC ohmmeter (HP 974A).The measurements by the AC milli-ohmmeter at 1 KHz were also validated by Electrochemical Impedance Spectroscopy (GAMRY EIS 300) to validate that the values represent the ohmic components at the high frequency intercepts. DC ohmmeter was used to check whether the molten metal oxides exhibit mixed (both ionic and electronic) conductivity. AC milliohm-meter was used to detect the mixed conductivity and DC ohmmeter to detect the electronic conductivity. Significance of AC milliohm-meter (four probe measurement), Electrochemical Impedance Spectroscopy (EIS) and accuracy of

DC ohmmeter in detecting the electronic component of a mixed (both ionic and electronic) conductor will be discussed in the following sections.

3.2 Significance of AC milliohmmeter

A four probe measurement method was used to detect the mixed conductivity of metal oxide electrolytes because of its significant advantage over conventionally used two probe measurement. Figure 3.1 shows the equivalent circuits representing both two probe and four probe measurement techniques. In a two probe measurement technique current and voltage sensing leads are essentially the same. Current is supplied through the two probes and voltage is sensed internally between them. Resistance measured using this technique involves both contact resistance (R_c) and electrolyte resistance (R_Ω) which is inaccurate since R_Ω alone is required to determine the conductivity of the electrolyte. In a four probe
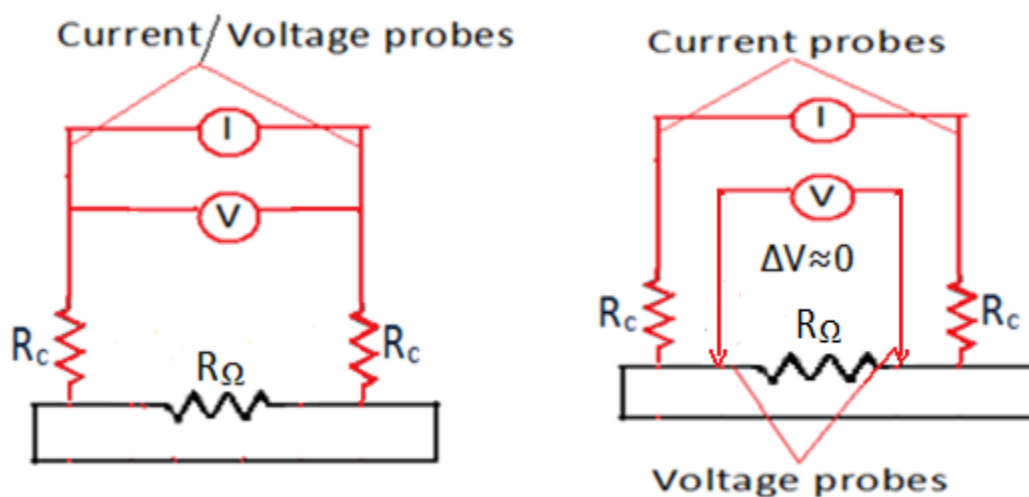
Figure 3.1: Equivalent circuits representing two probe (left) and four probe (right) measurement techniques

measurement technique, current is supplied through a pair of current sensing probes situated on the outside generating a voltage drop across the current sensing probes themselves. In order to exclude this voltage drop from the measurement, a pair of voltage sensing probes are placed adjacent to the current sensing probes. The precision of the technique comes from the fact that almost no current flows through the inner voltage sensing probes resulting in a near zero potential drop. Hence the contact and wiring resistances can be eliminated and the resistance of the electrolyte (R_Ω) is accurately measured. Due to the accuracy of four probe measurement technique, it is especially used in measurements involving highly conductive samples (low resistance) whereas two probe measurement because of its inability to eliminate the contact resistance, is generally used to evaluate highly resistive samples.

3.3 Significance of EIS

EIS was used to validate the conductivity measurements generated by AC milliohm-meter at 1KHz. Simplified equivalent circuit representing a four probe technique is shown in Figure 3.2. R_{sol} denotes the resistance of the electrolyte (both ionic and electronic). Resistance of the electrode is represented by a resistor ($R_{electrode}$) and capacitor (C) in parallel. $R_{electrode}$ includes kinetic resistance and capacitor (C) represents faradaic adsorption. Scanning the whole system from high frequency to low frequency using EIS, resistance of the electrolyte and kinetic resistance of the electrode can be precisely extracted. At high frequency, capacitor was not fully charged and hence acts as a short

circuit. Thus, R_{sol} was detected alone at high frequency. At low frequency, capacitor was fully charged and hence acts as an open circuit. Both R_{sol} and $R_{electrode}$ were detected at low
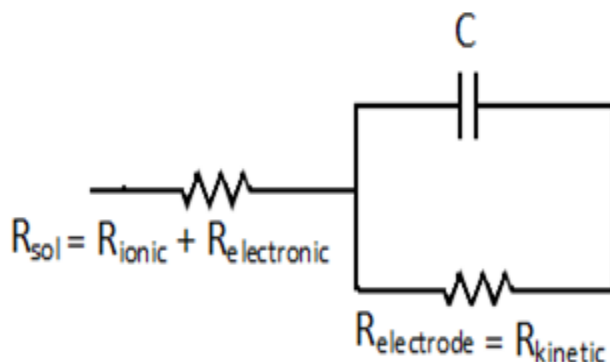
Figure 3.2: Simplified equivalent circuit denoting four probe measurement method

frequency. Based on the resistances obtained at high and low frequencies, kinetic contribution of the electrode can be eliminated yielding accurate resistance of the electrolyte (ionic and electronic). R_{sol} obtained using EIS was compared to the resistance obtained by AC milliohmmeter at 1KHz in order to check the accuracy of AC milliohm-meter.

3.4 Accuracy of DC ohmmeter

A simple experiment has been designed to demonstrate the accuracy of DC ohmmeter. Experimental setup and the procedure will be demonstrated in following paragraphs.

3.4.1 Experimental setup

Experimental setup mainly constitutes a glass beaker with a rectangular teflon frame fixed inside. Figure 3.3 demonstrates a schematic of the experimental setup. Height and diameter

of the beaker were 7 and 5.4 cm respectively. Height of the teflon frame was 5.4 cm. Width of the teflon frame was adjusted such that it fits effectively inside the beaker. Four notches
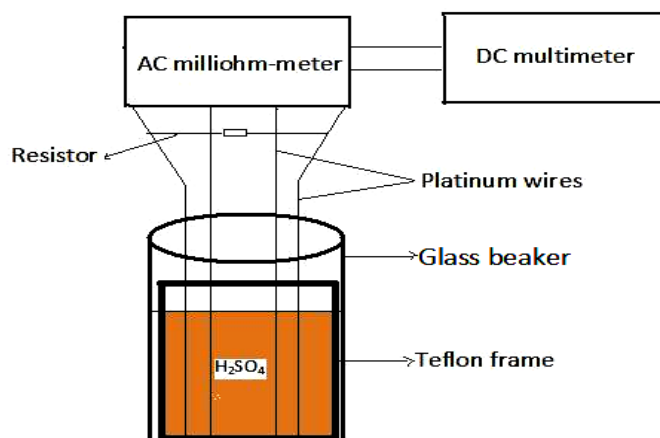
Figure 3.3: Schematic for demonstrating the accuracy of DC ohmmeter

were made on the bottom and top surfaces of the teflon frame. Platinum wires were then wrapped to these top and bottom notches. Platinum wires coming out of the setup were connected to the AC milliohm-meter and DC ohmmeter respectively.

3.4.2 Experimental procedure

Experimental procedure for determining the accuracy of DC ohmmeter is described below.

- Initially glass beaker was filled with sulphuric acid up to 5cm of the total height.

- Simultaneously an electronic resistor of known resistance was connected in parallel to the sulphuric acid.

- Readings obtained from the DC ohmmeter and AC milliohm-meter with only resistor, only sulfuric acid and both resistor and sulfuric acid were recorded.

- Whole experiment was then repeated by changing the resistor. Resistors having resistance between $1\Omega - 4.7k\Omega$ were used for the experiment.

- Accuracy of the DC ohmmeter was determined from the readings.

3.4.3 Results and Discussion

Readings corresponding to the experimental procedure are shown in Table 3.1. Based upon the data shown in Table 3.1 we can say that the DC ohmmeter detects only the resistance of the electronic resistor when it was simultaneously connected to both resistor and acid. Readings of the DC ohmmeter with sulfuric acid alone were unstable since it cannot detect the ionic conductivity. Hence we can say that the DC ohmmeter is accurate enough to detect the electronic component of a mixed conductor. In the following sections conductivity measurements of each of the metal oxides will be discussed individually and later compared with each other.

Table 3.1: Experimental data concerning accuracy of DC ohmmeter

Resistor used (ohm)	DC ohmmeter readings (ohm)		
	With resistor only	With resistor and acid	With acid only
1	1.2	1.2	Unstable
10	10.4	10.4	Unstable
22	22.4	22.4	Unstable
33	33.3	33.3	Unstable
50	51.3	51.4	Unstable
220	218.3	218.3	Unstable

3.5 Conductivity studies of Bi_2O_3

Conductivity studies of Bi_2O_3 involve both conductivity and stability measurements. Bi_2O_3 was mainly chosen because of its lower melting point and high ionic conductivity. A four

probe measurement method was used to determine the conductivity in order to eliminate the contact resistance.

3.5.1 Experimental setup for measuring the conductivity of Bi_2O_3

Experimental setup for evaluating the conductivity of bismuth oxide (Bi_2O_3) is shown in Figure 3.4. Setup mainly involves a high form alumina crucible of height 5.4cm, bottom diameter 2.15cm and top diameter 4.15cm. A rectangular crucible piece was glued to the bottom of the high form crucible and a bridge was constructed over it using alumina rods. The whole setup was put together using an alumina adhesive (Ceramabond 569). Four rectangular notches were indented on surfaces of both top and bottom crucible pieces. Platinum wires of thickness 0.2mm were wrapped on to the notches existing on both bottom and top crucible pieces. Platinum wires drawn out of the crucible were connected to AC milliohm-meter and DC ohmmeter in parallel in order to measure both mixed and electronic conductivity.
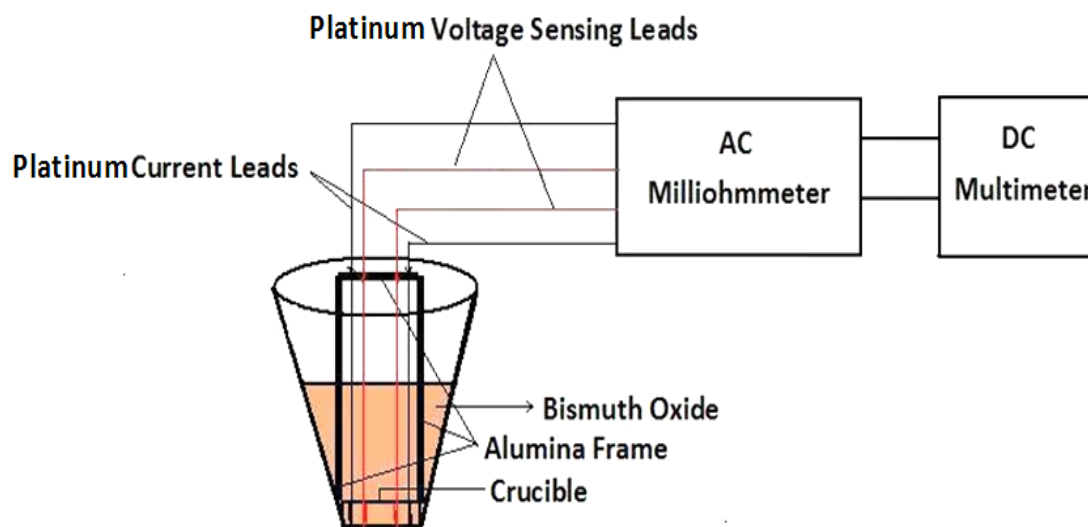
Figure 3.4: Schematic for evaluating the conductivity of Bi_2O_3

The high form crucible was then filled with Bi_2O_3 powder (10μm, 99.9% trace metal basis) and the whole arrangement was placed in a high temperature furnace. Temperature of the furnace was ramped to the melting point of Bi_2O_3 i.e. 825°C and was allowed to stay

(a)
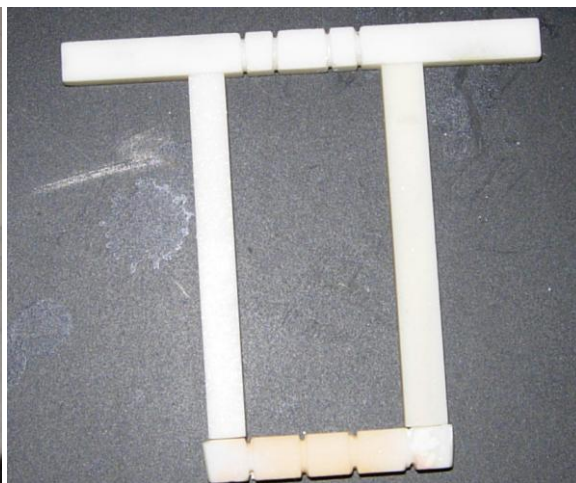
(b)

(c)
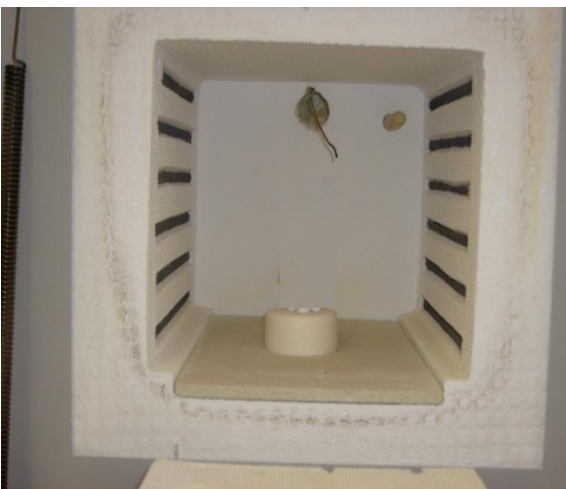
(d)

Figure 3.5: (a) Whole fixture with Bi_2O_3 crystal (b) Rectangular ceramic bridge (c) High temperature furnace (d) Chamber inside the high temperature furnace

there for 1 hour. After cooling down to room temperature, Bi_2O_3 crystal was formed which was then used for carrying out the conductivity measurement. Multiple runs were made until the crystal reaches optimum height which was determined by the cell constant measurements (described in the next section). Figure 3.5 shows the ceramic bridge, high temperature furnace and the whole experimental setup comprising bismuth oxide crystal.

3.5.2 Experimental procedure to evaluate the conductivity of Bi_2O_3

Conductivity measurement of Bi_2O_3 mainly involves three steps

a) Measuring cell constant of the experimental setup using 0.2M sulphuric acid

b) Validating the cell constant using 0.1 and 0.526M sulphuric acid

c) Evaluating conductivity of Bi_2O_3.

3.5.2.1 Measuring cell constant of the experimental setup

Cell constant measurement is essential in determining the optimum height of the metal oxide crystal inside the high form crucible. Conductivity data of sulfuric acid was well known in literature and hence used to estimate the cell constant of the setup.[53] Procedure for measuring the cell constant is described below.

- Initially 0.2M H_2SO_4 was prepared and resistance of H_2SO_4 was measured by pouring it into the high form crucible.

- Resistance of H_2SO_4 was measured at various heights i.e. at 1cm, 2 cm, 3cm and 4 cm using an AC milliohm-meter. Total height of the crucible was 5.4cm.

- Four probe sensing method was used to measure the resistance as shown in Figure 3.6.
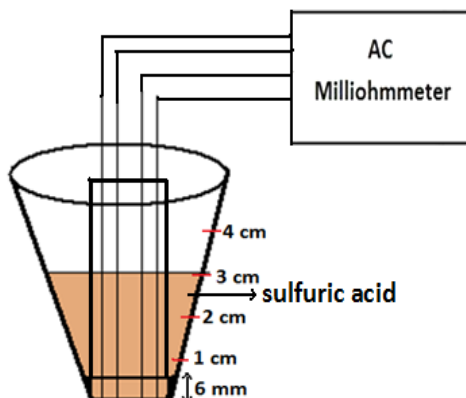
Figure 3.6: Schematic for cell constant estimation

- Two platinum wires situated on the outside were used as current sensing leads and inner two wires as voltage sensing leads.

- Using the conductivity data of H_2SO_4 from literature cell constant of the setup was evaluated at various heights.

The cell constant is measured using the following equation.

$$R = \rho\left(\frac{L}{A}\right) \text{------------------------ 3.1}$$

Where R = Resistance in ohm and ρ = Resistivity in ohm-cm

L/A = Cell constant (length over cross-sectional area) in cm^{-1}

3.5.2.2 Validating the cell constant

Cell constants estimated at different heights using 0.2M H_2SO_4 were validated using 0.1 and 0.526M H_2SO_4.Process for validating the cell constant is given below.

- Resistance measurements of 0.1 and 0.526M H_2SO_4 were made using the same procedure as described above.

- Cell constants measured using 0.2M H_2SO_4 were used to evaluate the conductivity of 0.1 and 0.526M H_2SO_4 at various heights.

- These experimental conductivities were compared with ones from the literature and best height for evaluating conductivity of bismuth oxide was determined.

3.5.2.3 Evaluating the conductivity of Bi_2O_3

After estimating the optimum height, the high form crucible with Bi_2O_3 crystal as shown on Figure 3.4 was placed inside the high temperature furnace to carry out the conductivity measurements. Steps for evaluating the conductivity of Bi_2O_3 are shown below.

- Initially the whole experimental setup was placed inside the high temperature furnace and was made sure that four platinum wires from the crucible come out of the furnace at four different locations without overlapping.

- Furnace was then closed and platinum wires coming out were wrapped around the screws mounted on a wooden block which was placed on the top of the furnace.

- Alligator clips from the AC milliohm-meter and DC ohmmeter were attached to the screws.

- Ramp rate of the furnace was maintained at 5˚C/min until 700˚C and resistance readings were taken at 50˚C intervals between 400 -700˚C.

- After reaching 700˚C, the ramp rate of the furnace was decreased to 1˚C/min and resistance readings were taken at 25˚C intervals between 700-900˚C.

- At every set point the furnace was allowed to settle down for 30-45 minutes in order to obtain uniform temperature distribution inside the furnace.

- After completion of the experiment, the furnace was allowed to cool down naturally.

- Three conductivity runs were made in order to check the reproducibility of the data obtained.

3.5.3 Results and Discussion

Results concerning the cell constant measurement at various heights using 0.2M H_2SO_4 are shown in Table 3.2. Cell constants obtained using 0.2M H_2SO_4 were used to calculate the conductivities of 0.1 and 0.526M H_2SO_4 at various heights i.e. 1, 2, 3 and 4cm respectively.

Table 3.2: Cell constant measurements using 0.2M H_2SO_4

Height (cm)	Resistance (ohm)	Cell constant (cm^{-1})
1	4.07	0.37
2	3.16	0.3
3	2.54	0.24
4	2.22	0.2

Tables 3.3 and 3.4 show the comparison of experimental and theoretical resistivities of 0.1 and 0.526M H_2SO_4 at various heights. Since the thickness of the bottom crucible piece is 6 mm, electrolyte at heights 1and 2 cm was insufficient enough to measure the resistivity generating high errors. Error percentage between experimental and theoretical resistivities at heights 3 and 4 cm was within 5% due to the presence of ample electrolyte in

Table 3.3: Validation of cell constant using 0.1 M H_2SO_4

Height (cm)	Resistivity(experimental), Ω-cm	Resistivity(theoretical), Ω-cm	Error (%)
1	16.66	20.92	20.4
2	18.41	20.92	12
3	20.16	20.92	3.6
4	22.3	20.92	6.6

Table 3.4: Validation of cell constant using 0.526 M H_2SO_4

Height (cm)	Resistivity (experimental), Ω-cm	Resistivity (theoretical), Ω-cm	Error (%)
1	6	4.74	25
2	4.8	4.74	1.4
3	4.5	4.74	5.4
4	4.6	4.74	3

the cell. Hence any height between 3 and 4 cm can be assumed as an ideal height for measuring the conductivity of Bi_2O_3.

AC milliohm-meter and DC ohmmeter were used to measure total and electronic conductivity respectively. The results show that bismuth oxide was highly conductive in its molten state and exhibits both ionic and electronic conductivity. We haven't separated the ionic conductivity from the total conductivity but the electronic conductivity has been detected successfully using a DC ohmmeter. From Figure 3.7, which shows the average conductivity from three runs of Bi_2O_3 over a temperature range of 400˚C to 900˚C, one can

see a sharp rise in both the total and electronic conductivity when bismuth oxide begins to transform from α state to δ state around 725˚C. The electronic conductivity of Bi_2O_3 between 400 and 725˚C was approximately 25 - 40% of total conductivity. Between 750 and 810˚C the electronic conductivity was 2-5% of the total conductivity, and therefore, Bi_2O_3 was essentially an ionic conductor ($t_i > 0.9$) in this temperature range. Beyond 810˚C there was another sharp rise in the total conductivity as Bi_2O_3 starts to transform into liquid form. Beyond its melting point, 825˚C, Bi_2O_3 was completely in liquid form, and the total conductivity of Bi_2O_3 in this state was almost three orders of magnitude higher than the electronic conductivity, and therefore, Bi_2O_3 can be considered to be exclusively an ionic conductor in this temperature range. Note that while the electronic conductivity relative to the total conductivity was very small, it was still high enough to create a major electrical short between the anode and the cathode if a pure ionic conductor was not used between Bi_2O_3 and the cathode. For example, an electrolyte gap of 20 microns with an electronic conductivity of 0.007 S/cm (e.g. for molten Bi_2O_3 at 825˚C) has an electronic areal resistance (R_{areal}) of 0.286 ohm/cm^2 which could pass as much as 0.35 A/cm^2 for a 0.1 V potential difference or 3.5 A/cm^2 for a 1V potential difference across this electrolyte gap.

Due to its high conductivity at temperatures around 900˚C higher efficiency and power density can be achieved when compared to electrolyte systems such as molten carbonate, hydroxide and phosphoric acid which operate at lower temperatures. Also, the mixed conductivity data obtained between 400˚C and 750˚C were in good agreement with the published values (Harwig et al.).[17] These conductivity measurements were further validated with the aid of Electrochemical Impedance Spectroscopy (EIS). Scan range was

between 0.2Hz-100KHz. Impedance obtained by the AC milli-ohmmeter at 1 kHz was found to be close to the impedance obtained at the high frequency intercept obtained with
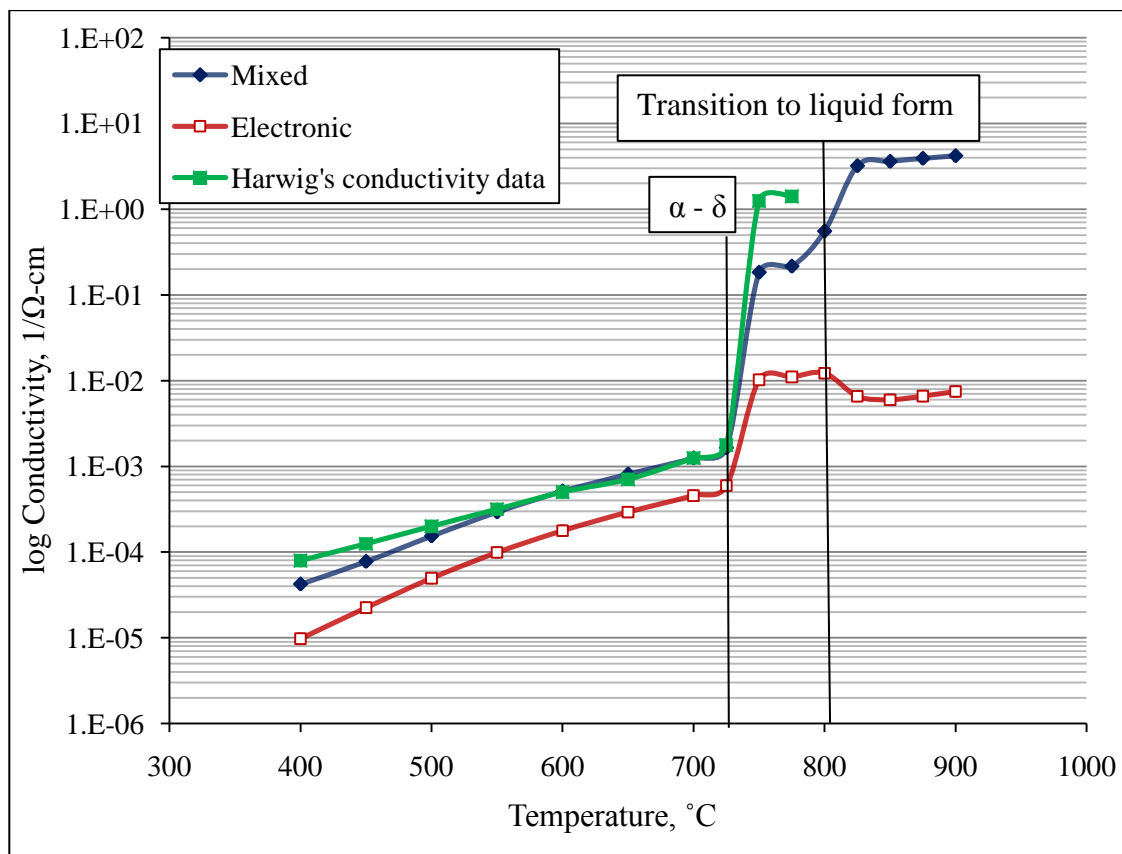
Figure 3.7: Mixed and electronic conductivity of Bi_2O_3

Electrochemical Impedance Spectroscopy (EIS) (0.2 Hz to 100 KHz) which excludes the kinetic contribution from the electrodes. Figure 3.8 shows the nyquist plot obtained from the EIS measurements at 900˚C. From the resistance obtained at high frequency intercept (1585 Hz), mixed conductivity was found to be 4.5 ohm^{-1}cm^{-1}. This conductivity was close enough to the mixed conductivity obtained using AC milliohm-meter which was 4.2 ohm^{-1}cm^{-1}. Hence AC milliohm-meter was found to be accurate enough to evaluate the mixed conductivity of Bi_2O_3.
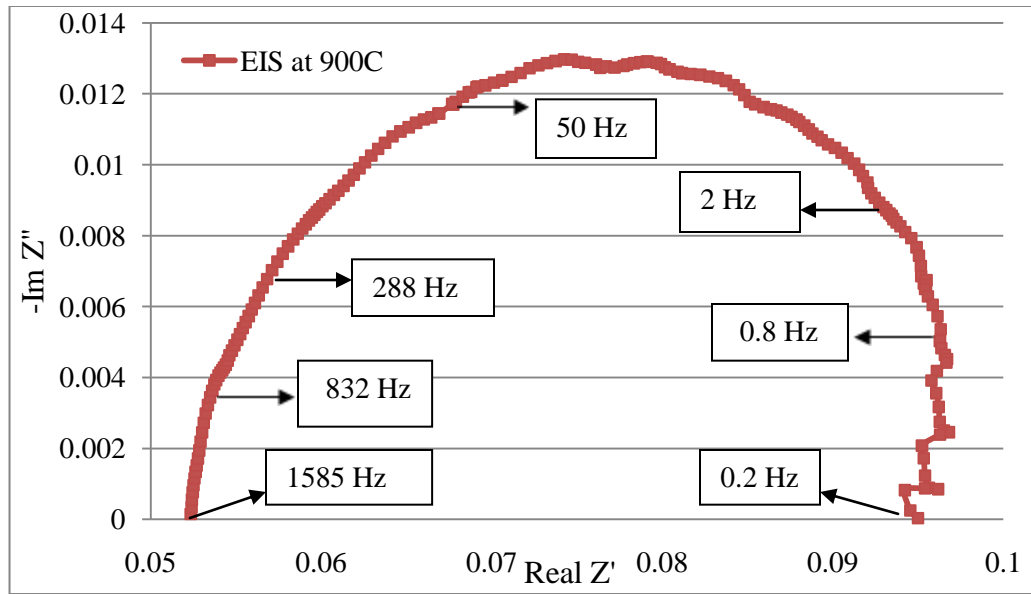
Figure 3.8: EIS of Bi_2O_3 at 900°C

3.6 Stability of Bi_2O_3 under CO_2 environment

Carbon dioxide (CO_2) is one of the byproducts in DCFC. So, in order to assess the stability

of molten Bi_2O_3 under CO_2 environment the same setup as shown in Figure 3.4 was used

but with a slight extension as shown in Figure 3.9. CO_2 was fed into the high form crucible
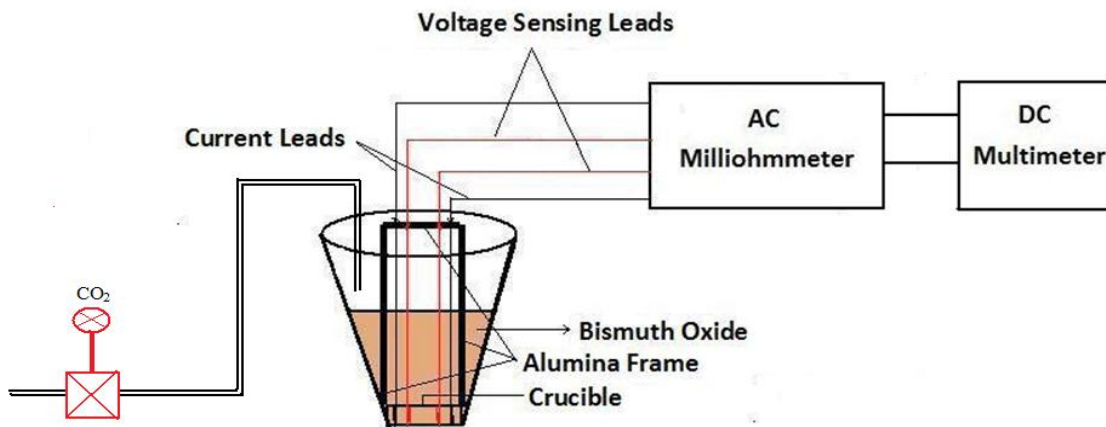
Figure 3.9: Schematic for assessing the stability of Bi_2O_3 under CO_2 environment

crucible through a stainless steel tube and conductivity of molten Bi_2O_3 was monitored over a period of time.

3.6.1 EDX and XRD analysis

Bi_2O_3 may react with CO_2 leading to the formation of bismuth carbonate which may raise stability issues. So, Energy Dispersive X-ray spectroscopy (EDX) and X-ray diffraction (XRD) analysis was done in order to detect possible carbonate formation. For this analysis both pure and CO_2 treated samples were investigated.

3.6.2 Results and Discussion

With carbon used as the fuel at the anode carbon dioxide was formed as a by-product. Resulting carbon dioxide may further react with Bi_2O_3 leading to possible formation of bismuth carbonate. In order to check whether bismuth carbonate hinders the performance of DCFC, conductivity measurement using the setup in Figure 3.9 was done under CO_2 environment at 825˚C. As before, the conductivity obtained by the AC milli-ohmmeter was validated against the high frequency intercept values obtained from EIS. Partial pressure of CO_2 is 1 atm. Stability of Bi_2O_3 over a period of time is shown in Figure 3.10. From this result it is evident that after 90 minutes molten Bi_2O_3 tends to stabilize.

Table 3.5 shows the mixed and electronic conductivities of both pure and CO_2 treated Bi_2O_3 at 825˚C. Both mixed and electronic conductivity decreased by approximately 40% under CO_2 environment. Prior to stability assessment of Bi_2O_3 under CO_2 environment, conductivity of Bi_2O_3 was monitored in air environment. No decrease in conductivity was
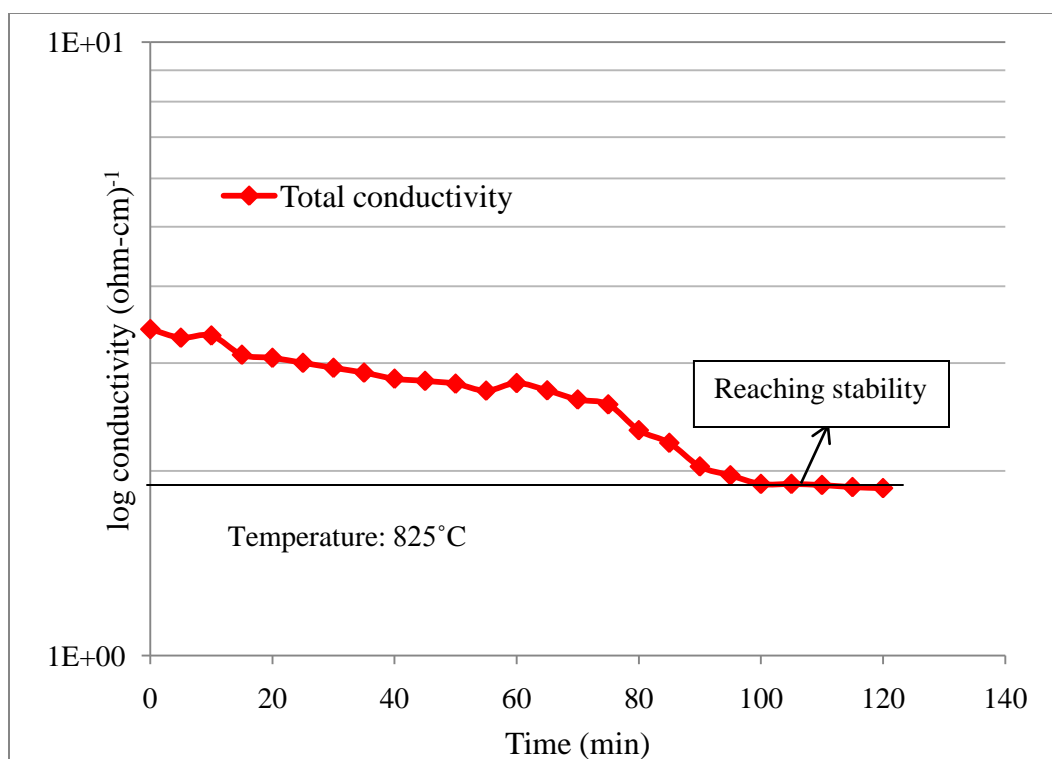
Figure 3.10: Variation of conductivity over time under CO_2 environment

observed over a long period of time which shows that there was no loss of material. However, under CO_2 environment there was a slight decrease in the conductivity which could be attributed to possible carbonate formation. To further investigate and confirm the carbonate formation, Energy Dispersive Spectroscopy (EDS) and X-ray Diffraction (XRD)

Table 3.5: CO_2 effect on conductivity of molten Bi_2O_3 at 825˚C

Type of electrolyte	Mixed Conductivity (S/cm)	Electronic conductivity(S/cm)
Pure Bi_2O_3	3.2	0.0066
CO_2 treated Bi_2O_3	1.88	0.0038

techniques were used to analyze both pure and CO_2 treated samples.

EDX analysis was done in order to find the oxygen to bismuth ratio of pure and CO_2 treated Bi_2O_3. Figure 3.11 shows EDX plots of both pure and CO_2 treated bismuth oxide samples. Oxygen to bismuth ratio acquired from EDX software was also validated by manually calculating the area under bismuth (Bi Ma) and oxygen (O Ka) curves. Analysis revealed that there was an increase in oxygen content by 50 percent per mole of bismuth. The X-axis in the graph represents intensity and the Y-axis wavelength of the X-ray. Applied voltage was around 15kV since bismuth oxide has higher atomic mass and number. Three different peaks of bismuth represent three different energy levels, larger peak being the higher energetic one. The aluminum peak on the curve appears due to the exposed aluminum stub on which the samples were placed and the other small peaks corresponding to carbon and fluorine arise due to minor impurities present in the samples.
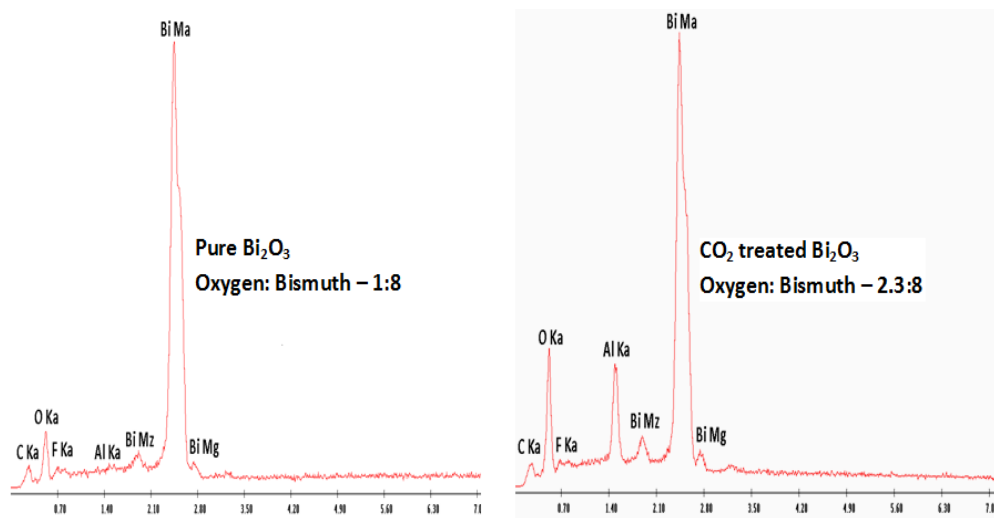
Figure 3.11: EDX analysis of pure and CO_2 treated Bi_2O_3
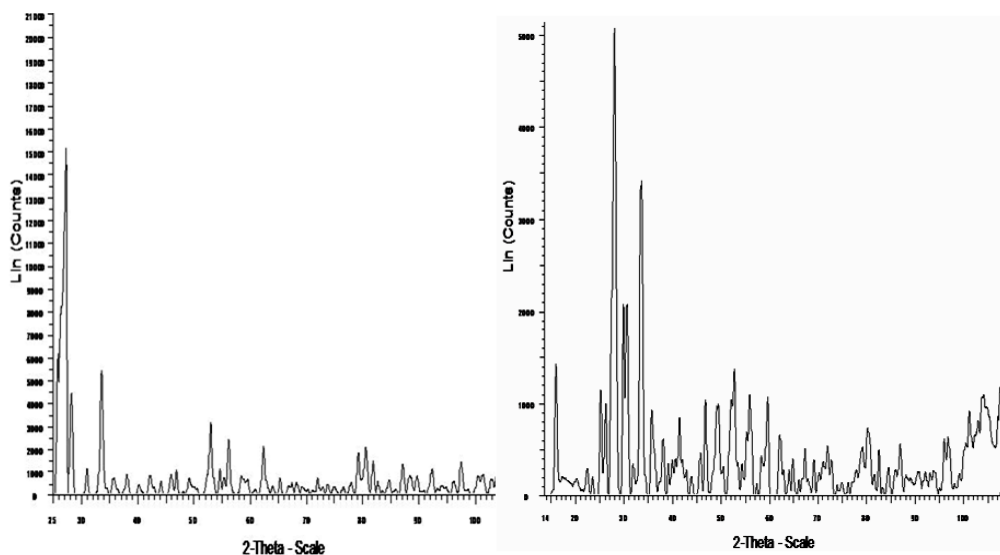
Figure 3.12: XRD analysis of pure and CO_2 treated Bi_2O_3

Furthermore XRD analysis was done to examine the changes in crystal structure of both pure and CO_2 treated Bi_2O_3. Figure 3.12 shows the XRD analysis of pure and CO_2 treated Bi_2O_3. XRD data also support the fact that CO_2 treated Bi_2O_3 undergoes minor changes in its crystal structure. X-axis and Y-axis in the plot represent scattering angle and intensity respectively. From both EDX and XRD analysis, the decrease in conductivity could be attributed to possible carbonate formation.

3.7 Conductivity studies of V_2O_5

Vanadium pentoxide (V_2O_5) was mainly chosen because of its lower melting point and higher abundance. Conductivity studies of V_2O_5 were done in a similar manner as Bi_2O_3 with some minor modifications. Initially cell constant was estimated and then conductivity was measured.

3.7.1 Experimental setup

Setup used for conductivity was similar to Figure 3.4 but with a small modification. The whole ceramic bridge was elevated by 3-4 mm for the electrolyte to contact the platinum wires all the way around as shown in the Figure 3.13 below. Dimensions and materials of the setup remain the same as in the case of Bi_2O_3. Even setup for the cell constant measurement remains the same. After preparing the setup, V_2O_5 powder was poured into the crucible for building up the crystal in order to measure the conductivity.
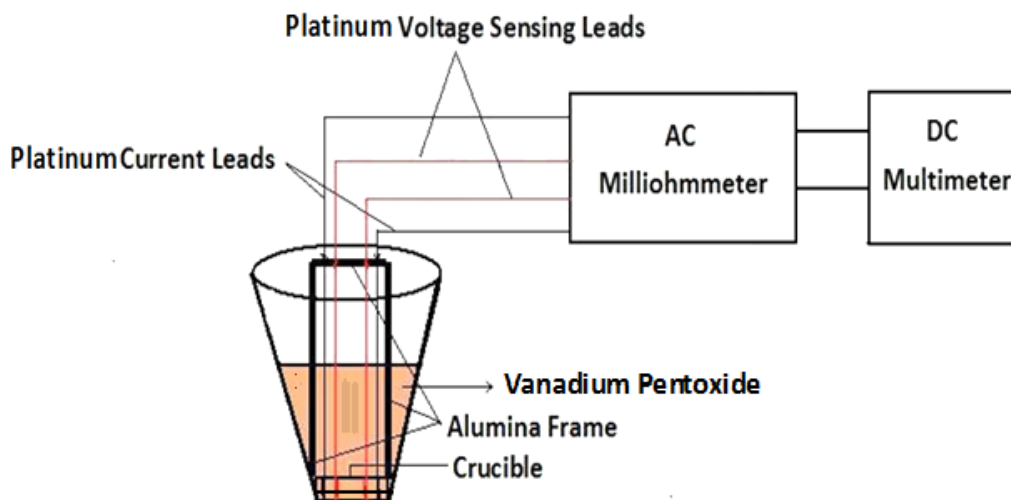
Figure 3.13: Schematic of the cell for conductivity measurement of V_2O_5

3.7.2 Experimental procedure

Experimental procedure involves two steps, cell constant measurement and conductivity measurement. Cell constant was measured and validated using H_2SO_4, procedure being similar as discussed in sections 3.3.2.1 and 3.3.2.2. The procedure for the conductivity measurement was also the same as discussed in section 3.3.2.3 except for the adjustment of

ramp rate at different temperature intervals. Ramp rate of the furnace was maintained at 3˚C/min until 600˚C and 1˚C/min between 600-750˚C. Resistance readings were taken at 25˚C intervals between 100-750˚C.

3.7.3 Results and Discussion

Results corresponding to cell constant measurement using 0.526M H_2SO_4 are shown below in Table 3.6. Cell constants measured using 0.526M H_2SO_4 were used to calculate the resistivities of 0.1and 0.2 M H_2SO_4 at various heights in the crucible and then compared to

Table 3.6: Cell constant measurement using 0.526M H_2SO_4

Height (cm)	Resistance (ohm)	Cell constant (cm^{-1})
1	1.29	0.271
2	0.73	0.154
3	0.67	0.141
4	0.51	0.108

Table 3.7: Validation of cell constant using 0.1M H_2SO_4

Height (cm)	Resistivity(experimental), Ω-cm	Resistivity(theoretical), Ω-cm	Error (%)
1	18.6	20.92	12
2	23.4	20.92	11
3	21.4	20.92	2
4	21.01	20.92	0.4

Table 3.8: Validation of cell constant using 0.2M H_2SO_4

Height (cm)	Resistivity(experimental), Ω-cm	Resistivity(theoretical), Ω-cm	Error (%)
1	13.86	10.86	22
2	12.98	10.86	16
3	10.92	10.86	0.5
4	11.75	10.86	7

the resistivities reported in literature in order to find the ideal height for measuring the conductivity. Results concerning validation of cell constant were shown in Tables 3.7 and 3.8. Based on the cell constant measurements any height between 3-4 cm would be ideal for the conductivity measurements.

Conductivity measurements were carried out using AC milliohm-meter and DC ohmmeter to find the mixed and electronic conductivity. However, there was a problem in measuring the conductivity using high form alumina crucible. Due to substantial volumetric expansion of V_2O_5 during the cooling process, the alumina crucible developed cracks on its surface rendering it useless to generate multiple conductivity runs. Hence three different alumina crucibles were used to generate three conductivity runs which was a bit strenuous. Figure 3.14 shows the alumina crucible after the second run. Although these cracks have been covered using alumina adhesive while evaluating the conductivity, molten V_2O_5 still leaked leading to a bit uncertainty in the data obtained.

Figure 3.14: Cracks visible on the surface of the alumina crucible after the second run

Further investigating the literature, it was found that quartz containers were used for handling V_2O_5. Hence the whole process was repeated again by replacing the alumina crucible with quartz crucible with similar dimensions as the former. Also, the alumina ceramic bridge was replaced with a quartz one with the experimental setup and procedure remaining the same. Cell constant was measured again using H_2SO_4 which proved that 3-4 cm was an ideal height for measuring the conductivity. Figure 3.15 shows the plot comparing the mixed and electronic conductivities obtained by both alumina and quartz crucible. From the graph one can see a sharp rise in total conductivity at 690°C where V_2O_5 transforms from solid to molten state. Between 100 - 675°C electronic conductivity of V_2O_5 was 15-20% of total conductivity. The electronic conductivity of V_2O_5 between 675-750°C was 4-10% of the total conductivity which makes it a predominant ionic conductor in this temperature range. Beyond 700°C V_2O_5 was completely transformed into liquid form where total conductivity was two orders of magnitude higher than electronic conductivity.
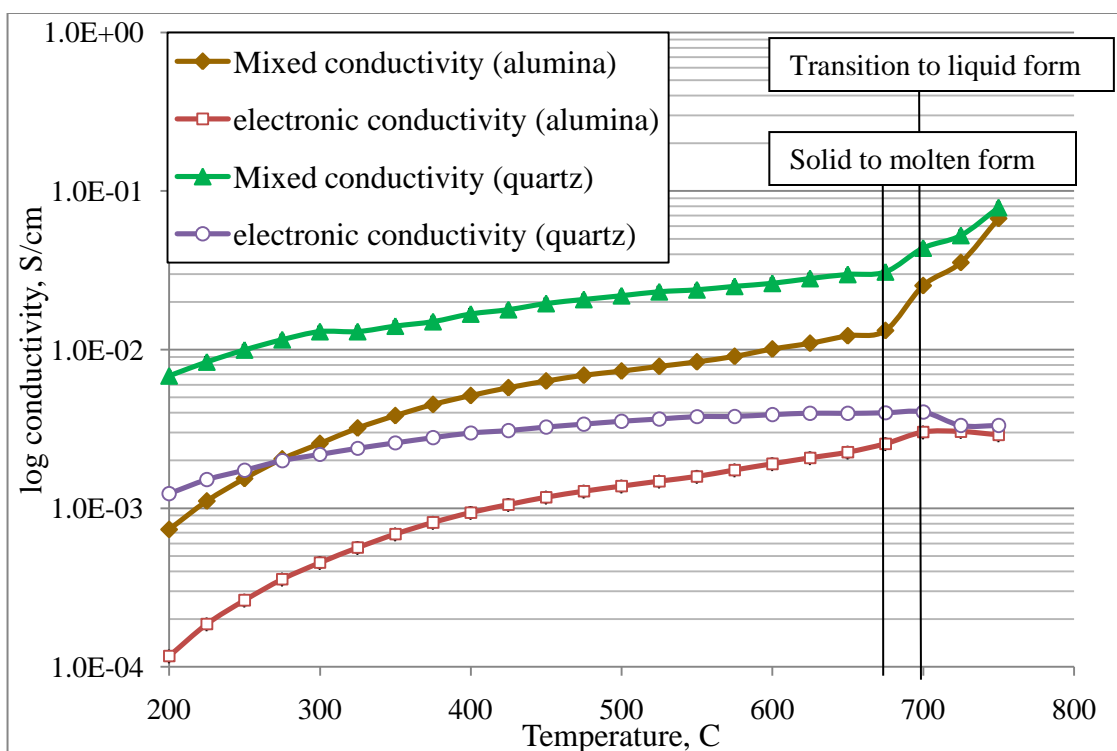
Figure 3.15: Total and electronic conductivity of V_2O_5

Conductivity of V_2O_5 was lower when compared to that of Bi_2O_3 but it has the advantage of lower melting point which decreases the operating temperature of DCFC further.

Although quartz crucible survived multiple conductivity runs, it eventually yielded to the significant volumetric expansion of V_2O_5. Figure 3.16 shows the quartz crucible after multiple conductivity runs. Finally conductivity data obtained by alumina and quartz crucibles were compared to the existing data in literature to check which of the crucibles generated accurate data. Conductivity data between 670-1000°C has been reported in the literature by Wilson *et al*[25] and Alleresma *et al*.[27] A Gold-palladium crucible has been used by Wilson *et al* in order to evaluate the conductivity of V_2O_5.

Figure 3.16: Cracks developed on the surface of the quartz crucible after multiple

conductivity runs

Figure 3.17 shows the comparison of the experimental data obtained using alumina and quartz crucible with that existing in literature. From the graph one can see that mixed conductivity data from existing literature (Wilson and Alleresma *et al.*) is closer to the conductivity data obtained by quartz crucible. Thus, quartz was proven to be a better material in handling V_2O_5 when compared to alumina. Irrespective of the type of crucible used, the conductivity data acquired from literature (gold-palladium crucible), quartz and alumina crucibles eventually merged beyond the melting point of V_2O_5 whereas at low temperatures there was a large mismatch between the conductivity data acquired from all the three crucibles. Possible explanation could be that, probe wires present inside the crucible alter their position every time the metal oxide is cooled from its melting point due to uneven crystallization. Hence, the cell constant of the experimental setup no longer applies in estimating the conductivity which explains the large variation in the conductivity data attained by different type of crucibles particularly below the melting point of metal

oxide. Once the metal oxide was molten, probes were no longer locked inside the crystal thus restoring to their initial position. This illustrates the merging of the conductivity data generated by different types of crucibles.
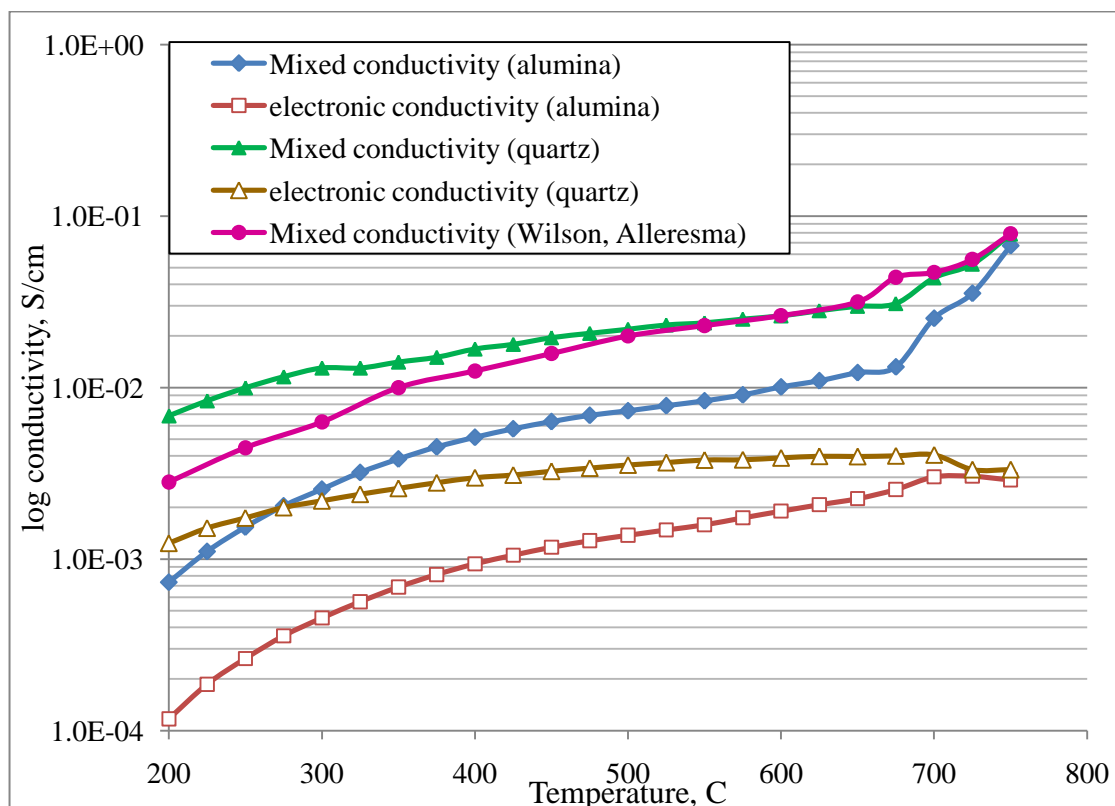
Figure 3.17: Comparison of experimental conductivity data with existing data in literature

As before, the accuracy of AC milliohm-meter was validated using EIS. Figure 3.18 shows the EIS at 675°C. Mixed conductivity based on the resistance acquired at the high frequency intercept (7943 Hz) was 0.036 $ohm^{-1}cm^{-1}$ which was close enough to the mixed conductivity obtained using AC milliohm-meter i.e. 0.034 $ohm^{-1}cm^{-1}$. Due to substantial volumetric expansion of V_2O_5, the quartz frame inside the high form crucible altered its

position at high temperatures resulting in an irregular impedance plot. Although the impedance plot doesn't make any sense, the high frequency intercept (electrolyte resistance) obtained was close to the data acquired by AC milliohmmeter. EIS scans were also done at other temperatures. The plots obtained were irregular but their high frequency
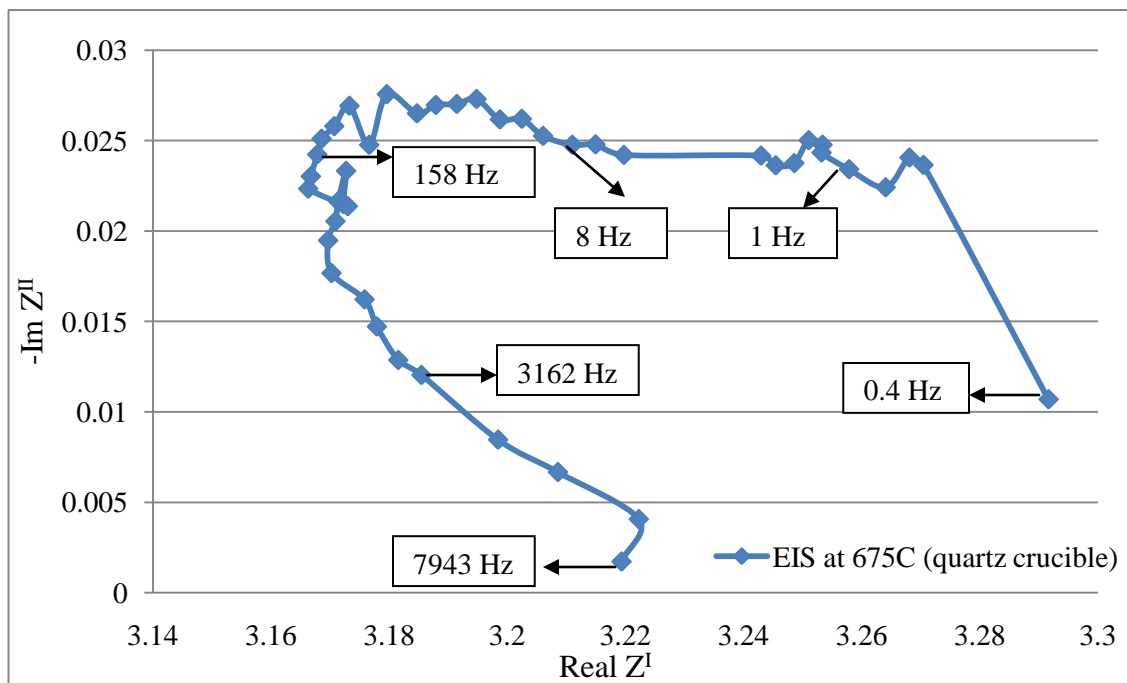
Figure 3.18: EIS of V_2O_5 at 675˚C

intercepts (electrolyte resistance) closely matched with data generated by AC milliohm-meter.

3.8 Conductivity measurements of TeO_2

TeO_2 is another metal oxide with a lower melting point and is known to be a predominant ionic conductor. Conductivity studies include measurement of cell constant followed by measurement of conductivity as before.

3.8.1 Experimental setup

The experimental setup for evaluating the conductivity is same as shown in Figure 3.13. Both alumina and quartz crucibles have been used for evaluating the conductivity of TeO_2. Figure 3.19 shows both vacant quartz crucible and the one filled with V_2O_5 crystal. A quartz adhesive (Resbond-905) was used to glue the frame and platinum wires to the crucible.

(a)   (b)
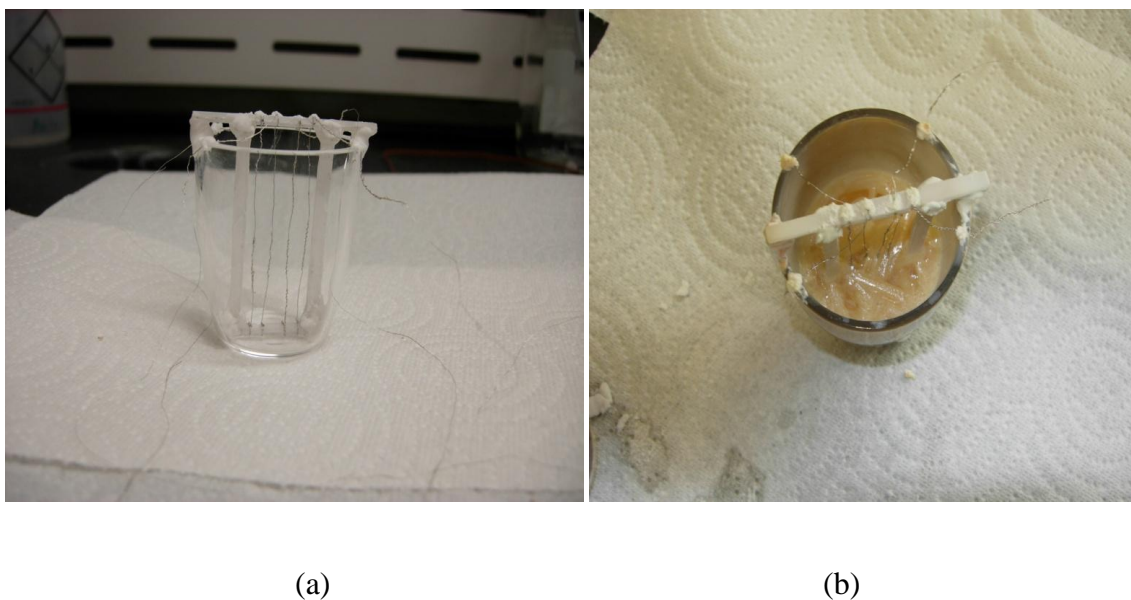
Figure 3.19: a) Quartz crucible with the frame and b) Quartz crucible with V_2O_5 crystal

3.8.2 Experimental procedure

Experimental procedure remains the same as discussed in section 3.5.2 except for the adjustment of the ramp rate. Ramp rate was maintained at 5˚C/min between 400-600˚C and 1˚C/min between 600-800˚C. Resistance readings were taken every 50˚C interval between 400-600˚C and every 25˚C intervals between 600-800˚C.

3.8.3 Results and Discussion

Initial conductivity measurements were performed using a high form alumina crucible. After measuring the cell constant of the setup, the crucible was filled with TeO_2 powder in order to measure the conductivity. After multiple conductivity runs it was found that TeO_2 reacted with alumina (Al_2O_3) above 650˚C resulting in the formation of a new complex i.e. Al_2TeO_6. Figure 3.20 shows the alumina frame before and after the reaction with TeO_2. Figure 3.20(right) shows the alumina frame after multiple conductivity runs. Part of the frame has been consumed by reacting with TeO_2 resulting in the formation of a new complex This resulted in the generation of unreliable conductivity data. Hence, alumina crucible has been replaced with quartz crucible for measuring the conductivity of TeO_2.
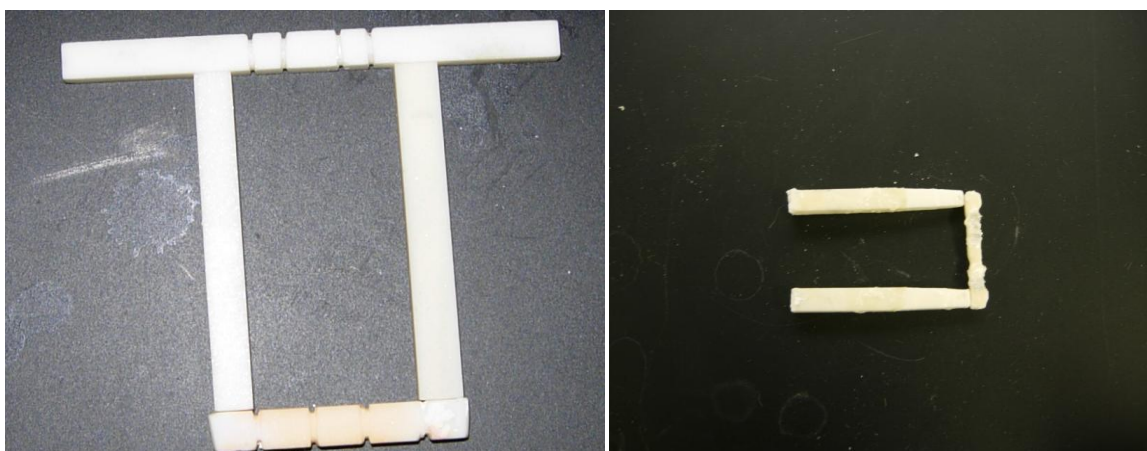
Figure 3.20: Alumina frame before (left) and after(right) reaction with TeO_2

After replacing the alumina crucible with quartz, the cell constant was measured using H_2SO_4 before proceeding to the conductivity measurements. Dimensions of the quartz crucibles were similar to the alumina crucible. Table 3.9 shows the cell constant

measurements estimated using 0.526M H_2SO_4. Estimated cell constants were validated using 0.2 and 0.1M H_2SO_4 as explained in the previous section 3.5.3. Tables 3.10 and 3.11 display the results concerning validation of the estimated cell constants. As before 3-4 cm was found to be the ideal height for performing the conductivity measurements. After measuring the cell constant, the quartz crucible was filled with TeO_2 crystal as shown in Figure 3.19(b).

Table 3.9: Estimation of cell constants at various heights using 0.526M H_2SO_4

Height (cm)	Resistance (ohm)	Cell constant (cm^{-1})
1	1.37	0.29
2	0.92	0.194
3	0.56	0.118
4	0.42	0.088

Table 3.10: Validation of cell constant using 0.1M H_2SO_4

Height (cm)	Resistivity (experimental), Ω-cm	Resistivity (theoretical), Ω-cm	Error (%)
1	20.41	20.92	2.5
2	18.35	20.92	12
3	21.27	20.92	2
4	20.88	20.92	0.2

Table 3.11: Validation of cell constant using 0.2M H_2SO_4

Height (cm)	Resistivity (experimental), Ω-cm	Resistivity (theoretical), Ω-cm	Error (%)
1	11.13	10.86	2.5
2	9.9	10.86	9
3	10.16	10.86	6
4	11.06	10.86	2
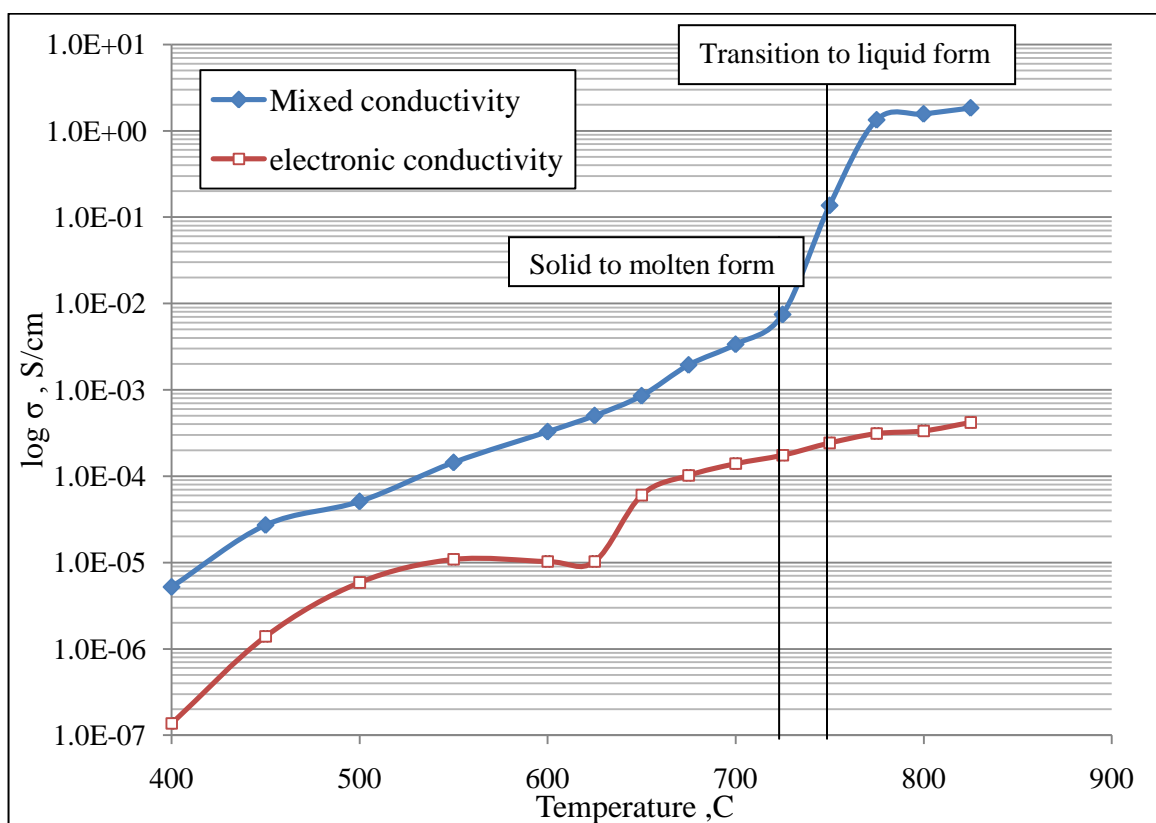
Figure 3.21: Mixed and electronic conductivity of TeO_2

Figure 3.21 shows the mixed and electronic conductivity of TeO_2 along with error bars. From the graph, one can see two major transitions at 725˚C and 750˚C respectively.

At 725°C TeO$_2$ transforms from solid to molten form. Electronic conductivity of TeO$_2$ was around 2-10% of total conductivity between 400-725°C and 0.02-0.1% of total conductivity between 725-800°C. This shows that TeO$_2$ is a predominant ionic conductor over the entire temperature range. Once TeO$_2$ reaches 750°C, it was completely transformed into liquid form where total conductivity was almost four orders of magnitude higher than electronic conductivity. Also, the electronic conductivity of V$_2$O$_5$ acquired was insignificant compared to mixed conductivity which explains the irregularity in the curve particularly at lower temperatures. Again the accuracy of AC milliohm-meter was tested using EIS. EIS of TeO$_2$ at 800°C is shown in Figure 3.22. Conductivity of TeO$_2$ based on the resistance
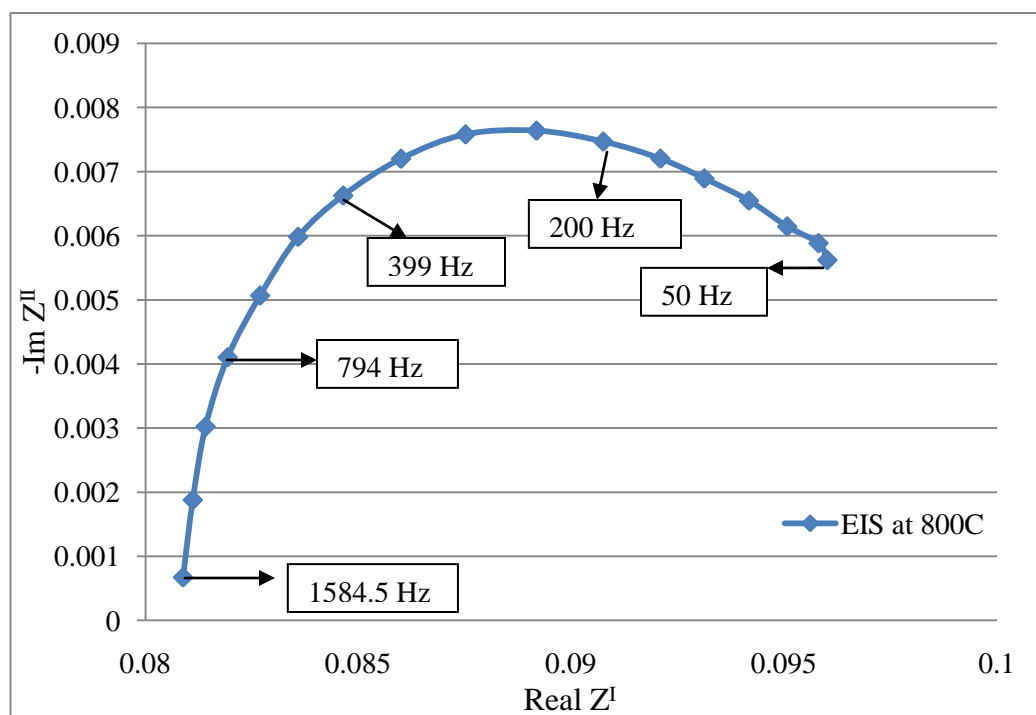
Figure 3.22: EIS of TeO$_2$ at 800°C

at high frequency intercept (1584.5 Hz) was 1.5 ohm^{-1}cm^{-1} which was close enough to the conductivity estimated using AC milliohm-meter i.e. 1.56 ohm^{-1}cm^{-1}.

3.9 Conclusions

Mixed and electronic conductivities of all the three metal oxides have been compared in Figure 3.23. Of all the three metal oxides, bismuth oxide and vanadium pentoxide exhibit high ionic and high electronic conductivity respectively. Since a molten electrolyte is required in a DCFC, emphasis was mainly on the conductivity acquired at the molten range. All the three metal oxides have displayed predominant ionic conductivity beyond their melting points. Although, the electronic conductivity of these metal oxides was small, it was high enough to cause an electrical short if a pure ionic conductor was not used between molten electrolyte and the cathode. If a mixed conducting electrolyte is used in a DCFC, solid carbon fuel will be completely consumed even though part of it gets separated from the whole electrode. Hence, electrolytes demonstrating mixed conductivity have an additional advantage. Also, these metal oxides have a lower melting point which is quite beneficial.

Of all the three metal oxides V_2O_5 is highly abundant and hence cost effective. However, the ionic conductivity of V_2O_5 was much smaller when compared to Bi_2O_3 and TeO_2. Although TeO_2 displays high ionic conductivity, the cost is very high rendering it as the least possible choice of all the three electrolytes. Bismuth oxide has low toxicity and high conductivity when compared to other two metal oxides making it a favorable choice as

an electrolyte in DCFC. However, all the three metal oxides have been tested in a DCFC

fixture and results will be discussed in the next chapter.
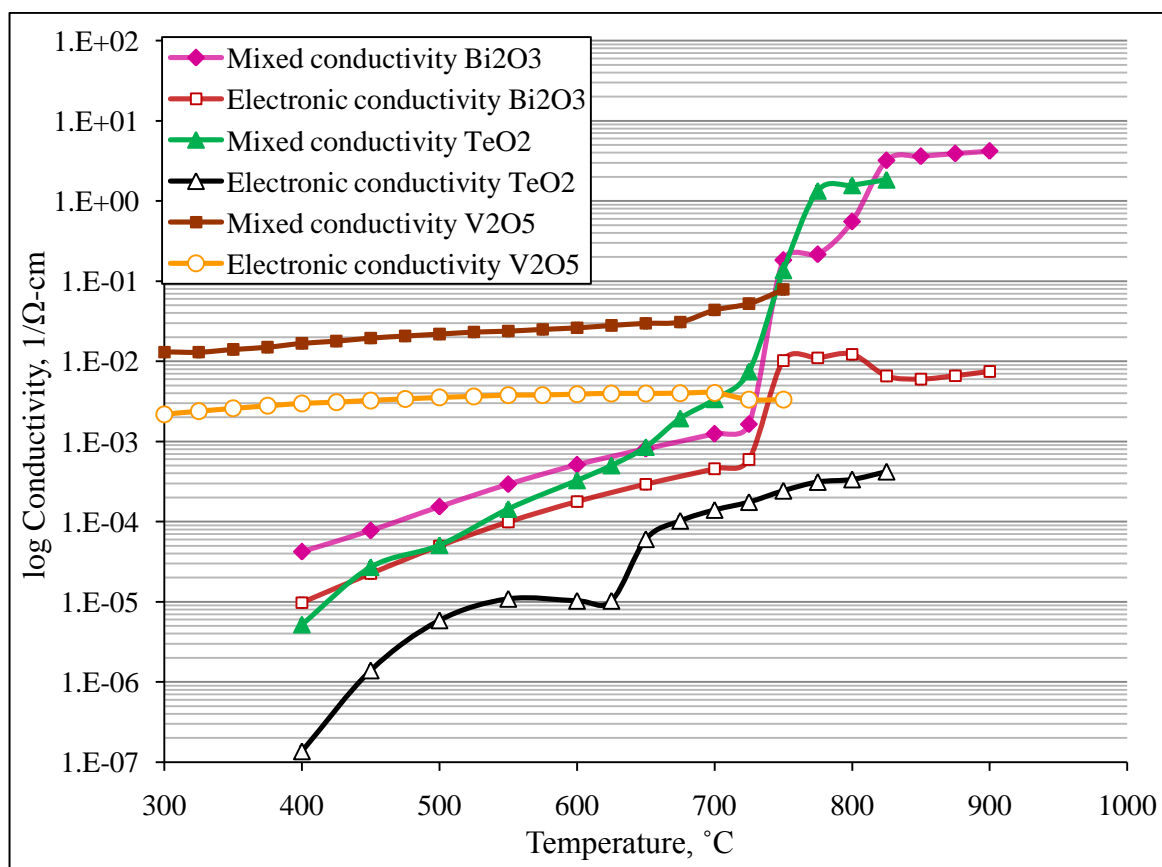
Figure 3.24: Comparison of the mixed and electronic conductivities of Bi_2O_3, V_2O_5 and

TeO_2

CHAPTER 4

Performance of molten metal oxide electrolytes in a DCFC

4.1 Introduction

The second part of this research concentrates on evaluating the performance of molten metal oxide electrolytes (Bi_2O_3, V_2O_5 and TeO_2) in a DCFC fixture. Until now extensive research has been done on investigating the performance of molten carbonate, molten hydroxide and phosphoric acid electrolytes in a DCFC fixture. These DCFC fixtures were not feasible since their operating temperature was not high enough to overcome the sluggish carbon oxidation kinetics. Moreover, corrosive nature of molten carbonate and hydroxide electrolytes degrades the performance of the electrodes and hence life span of DCFC. Using molten metal oxide electrolytes in a DCFC fixture, operating temperatures will be elevated resulting in higher kinetic rate and power density.

Electrochemical properties of carbon oxidation in these molten metal oxide electrolytes at various temperatures have been measured using a data acquisition device and a DC ohmmeter. Variation of thermodynamic potential with temperature has been assessed using a data acquisition device and DC ohmmeter was used to check whether there was any electrical short between anode and cathode.

4.2 Experimental setup

Since these molten electrolytes were mixed (both ionic and electronic) conductors, using them in a DCFC will require placing a solid state ionic electrolyte between the cell cathode

and the molten electrolyte to prevent shorting of the carbon anode and the molten electrolyte. Note that even though the electronic conductivity was very small relative to the total conductivity, it is still high enough to cause shorting. A hollow alumina tube of inner diameter 2cm was used as the cell. Composite YSZ/LSM discs were used as solid electrolyte/cathode because of their chemical compatibility and gold mesh was used as a current collector. The edges of the ceramic tube were sealed using an alumina adhesive. Figure 4.1 shows a schematic of a hybrid molten oxide DCFC used in this study. Air enters through the gold mesh and contacts the LSM cathode where oxygen in air was reduced to oxygen ions. These oxygen ions were transmitted through pure ionic conducting YSZ electrolyte to the anode where they react with carbon to generate electrical output and CO_2. One of the platinum wires was connected to the gold mesh and other to the carbon anode.
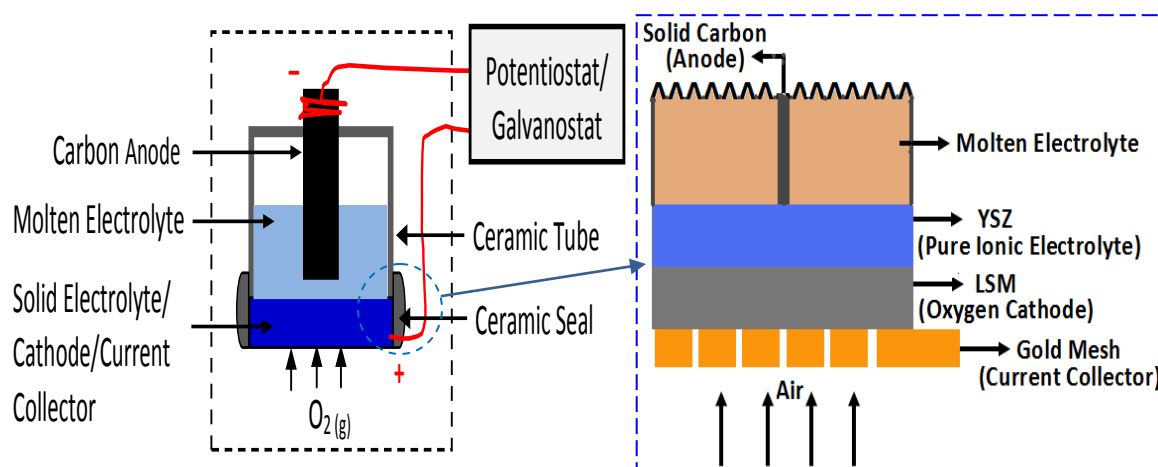
Figure 4.1: Schematic of the DCFC fixture

Platinum wires coming out of the fixture were hooked to a potentiostat. Electrochemical reactions involved with the DCFC fixture are shown below.

Anode: $C + 2O^= \longrightarrow CO_2 + 4e^-$

Cathode: $O_2 + 4e^- \longrightarrow 2O^=$

_____

Overall: $C + O_2 \longrightarrow CO_2 \quad E_0 = 1.02$ V
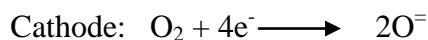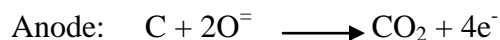
4.3 Experimental procedure

Initially composite YSZ/LSM discs were prepared and then the whole DCFC fixture was assembled for measuring the electrochemical properties. This section describes the experimental procedure involved with the fabrication of composite YSZ/LSM discs and measurement of electrochemical properties of the assembled hybrid DCFC fixture.

4.3.1 Preparation of composite YSZ/LSM discs

Composite YSZ/LSM samples prepared at University of Virginia were used in this study. Preparation of composite YSZ/LSM discs involves three steps which are listed below.

- Preparation of dense YSZ discs
- Screen printing of LSM ink on to the dense YSZ discs
- Co-sintering of composite YSZ/LSM discs

Initially 2 grams of YSZ powder (TZ-8Y, Tosoh, OH) was compressed in an uniaxial press at 140 bar. The resulting 0.75 inch diameter YSZ pellet was sintered in air at 1550˚C with a ramp rate of 2˚C/min for 6hours. After cooling down, dense YSZ discs of 2cm diameter and 1mm thickness were acquired.

Next step involves the preparation of LSM ink. In this process graphite powder and glycerine were used as pore former and solvent respectively. Initially LSM powder (Praxair specialty chemicals) was mixed with graphite powder (Alfa Aesar, 200 mesh) in 1: 1 ratio. This composite powder was mixed with glycerine (Alfa Aesar, 99% pure) resulting in a thick paste. Amount of glycerine was adjusted in such a way that the paste doesn't become
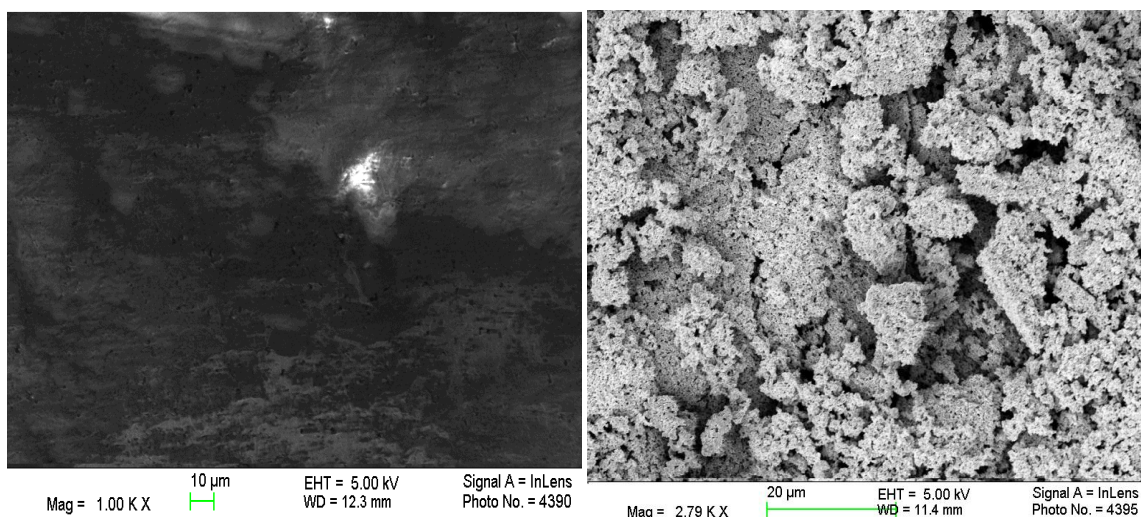
Figure 4.2: SEM images of dense YSZ (left image) and porous LSM (right image)

too dilute. The paste was then screen printed on to the dense YSZ substrate using a paint brush.

After screen printing the LSM ink, the composite YSZ/LSM discs were co-sintered in air at 1000°C with a ramp rate of 3°C/min for 4 hours. Graphite powder was evaporated at this temperature yielding porous LSM substrate of thickness of 250μm over dense YSZ discs. Figure 4.2 shows the SEM images of dense YSZ electrolyte and porous LSM cathode.

4.3.2 Procedure for measuring the electrochemical properties of DCFC

After preparing the composite YSZ/LSM discs, the whole DCFC fixture was assembled as shown in Figure 4.1. Procedure for evaluating the electrochemical properties is listed below.

- The whole DCFC fixture was mounted on alumina rods and then placed in the high temperature furnace.

- Platinum wires coming out of the fixture were then connected to data acquisition system and DC ohmmeter.

- Temperature of the furnace was then ramped at 5˚C/min until the metal oxide electrolyte was completely molten.

- Thermodynamic potential and resistance readings were taken at 50 ˚C intervals using data acquisition system and DC ohmmeter respectively.

- At every temperature set point readings were taken after 20-30min to ensure uniform temperature distribution inside the furnace.

- Finally voltage versus temperature and resistance versus temperature were plotted to analyze the performance of DCFC.

4.4 Performance of DCFC using molten Bi_2O_3 electrolyte

Bi_2O_3 is the primary choice of all three electrolytes because of its high ionic conductivity and low toxicity. Carbon and graphite rods were used as the solid carbon fuel in the DCFC. Figure 4.3 shows the assembled DCFC fixture. Alumina tube was filled with Bi_2O_3 powder and the whole setup was placed in the furnace. Nitrogen gas was blown over the top of the

Figure 4.3: Schematic of assembled DCFC fixture

fixture in order to prevent carbon rod from combustion with oxygen in air. Figure 4.4 shows the variation of thermodynamic potential with temperature with carbon rod as anode.
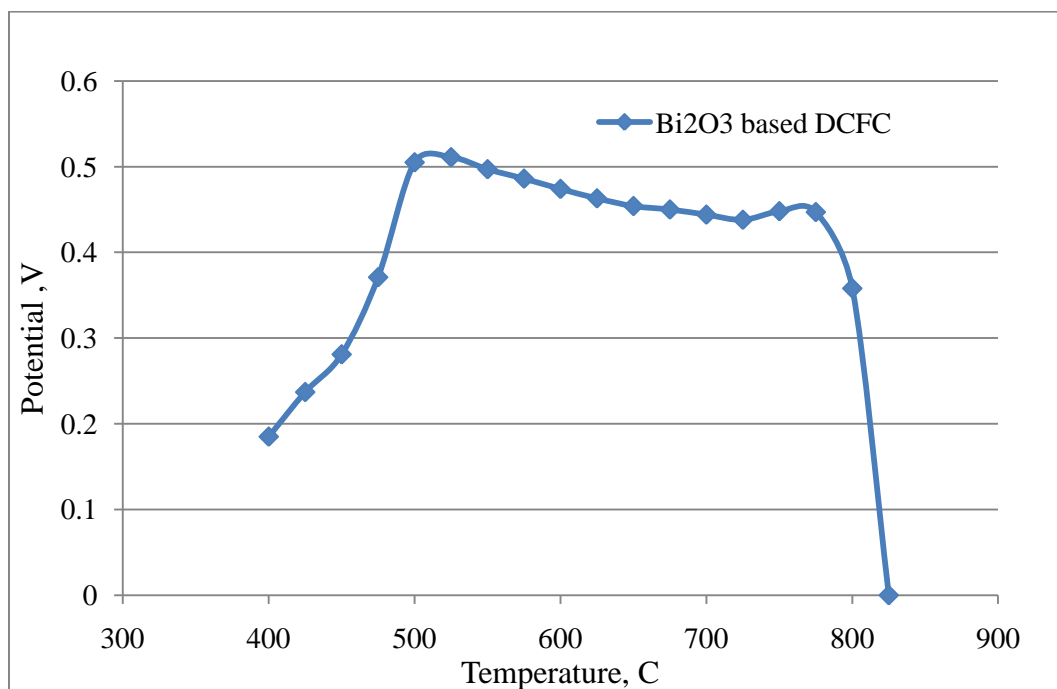
Figure 4.4: Performance of DCFC with a carbon rod

Thermodynamic potential of the DCFC fixture suddenly dropped to zero at 825˚C. Due to the rapid combustion of carbon rod at temperatures higher than 600˚C, platinum wire

connected to the carbon anode got loose resulting in zero potential readings. Thus carbon rod was proven to be inapplicable for DCFC applications.

Carbon rod was replaced with much stable graphite strip for the next run. Figure 4.5 shows the performance of the DCFC with graphite strip as anode. Although stable readings were obtained at higher temperatures, a decrease in potential was observed beyond 650˚C. Maximum potential obtained was around 0.55V which was very low. Analyzing the Bi_2O_3 crystal after multiple runs revealed traces of bismuth metal on the surface. Reduction of bismuth ions to bismuth metal was found to be more spontaneous than carbon oxidation. Thus, carbon instead of reacting with oxygen ions reduced bismuth oxide to bismuth metal
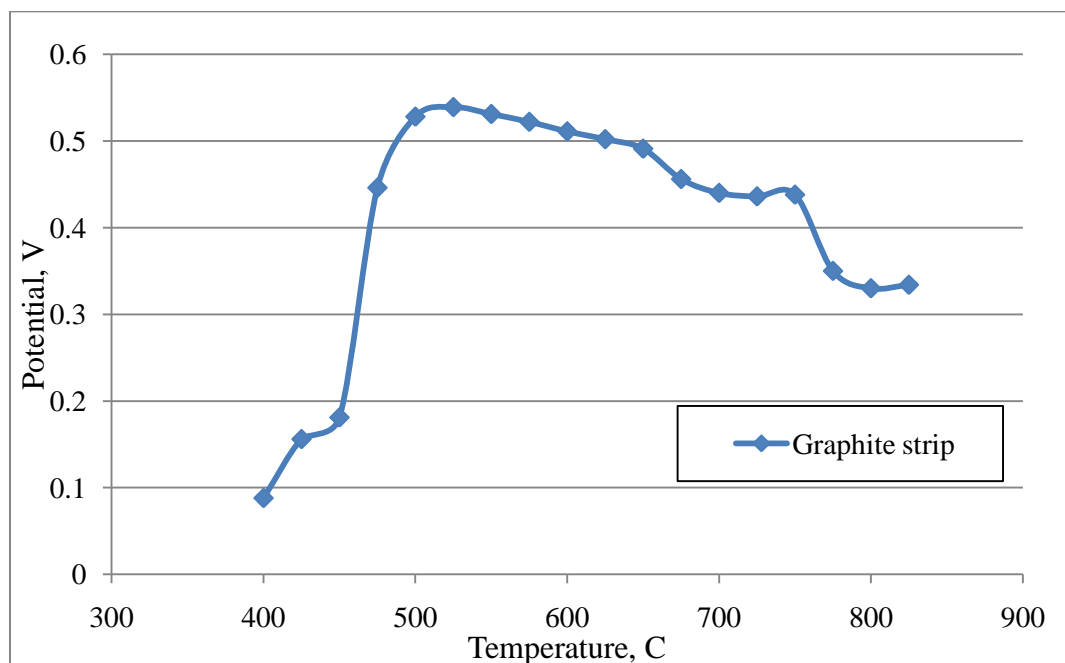
Figure 4.5: Performance of DCFC with graphite strip as anode material

at the anode degrading the performance of the DCFC. Figure 4.6 shows the traces of bismuth metal found on the surface of Bi_2O_3 crystal. Also, the resistance versus temperature data generated by DC ohmmeter has been plotted in Figure 4.7. Graphite strip

Figure 4.6: Traces of bismuth metal found on the surface of Bi_2O_3 crystal

was used as an anode in the DCFC fixture. Resistance between the anode and cathode increased with temperature indicating that there was a minor electrical short. Electrical short between the anode and cathode was mainly caused by diffusion of molten electrolyte through the alumina adhesive onto the cathode surface.
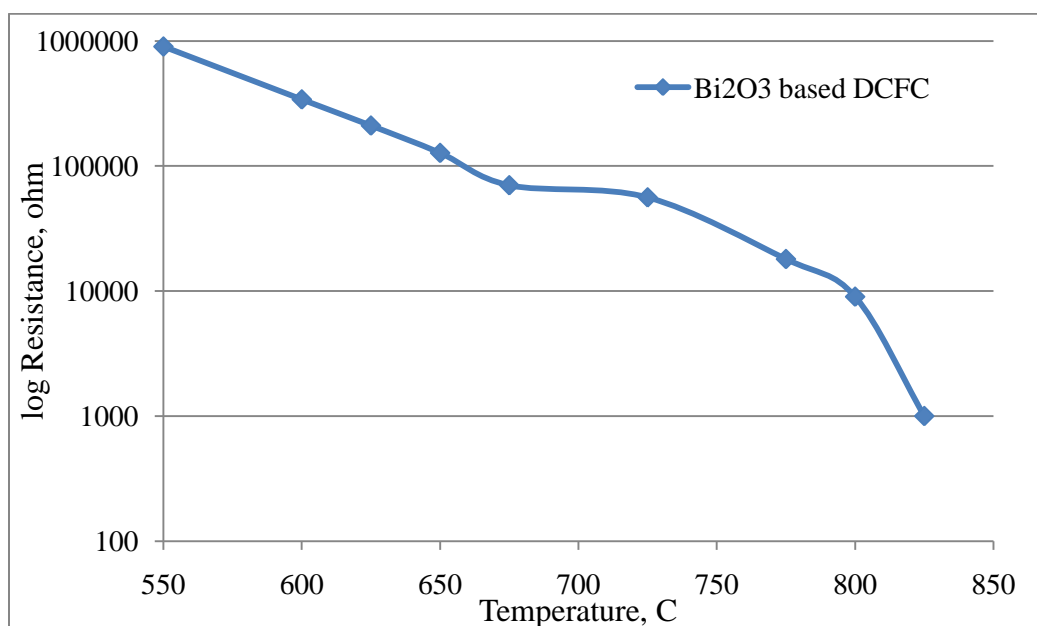
Figure 4.7: Resistance between the anode and cathode of a Bi_2O_3 based DCFC

4.5 Performance of the DCFC using molten V_2O_5 and TeO_2 electrolytes

One of the fundamental reasons for choosing V_2O_5 as an electrolyte in DCFC was that, reduction of vanadium ions to vanadium metal was less spontaneous than carbon oxidation. Also, V_2O_5 has a lower melting point, i.e. 690°C, when compared to Bi_2O_3.

Initially DCFC fixture has been prepared using alumina based materials. After the initial run, V_2O_5 was found to be contacting the cathode by diffusing through the alumina adhesive at higher temperatures. As discussed in section 3.7.3 alumina was an incompatible material for handling V_2O_5. Also, the thermodynamic potential readings obtained were very low (less than 0.1V). Figure 4.8 shows the whole DCFC fixture and cathode flooded by V_2O_5 after the first run.

(a)   (b)
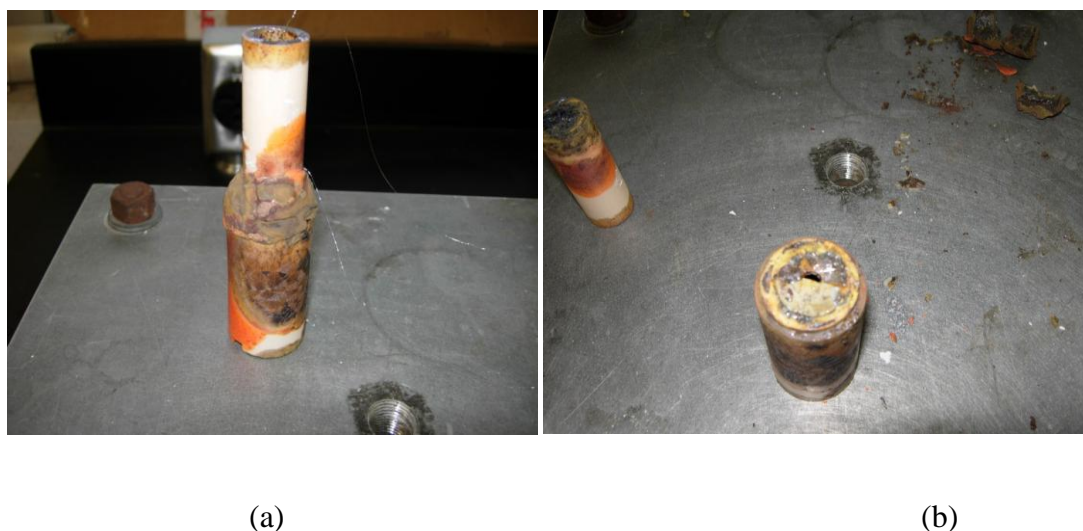
Figure 4.8: a) DCFC fixture showing leakage of V_2O_5 and b) LSM cathode flooded by

V_2O_5

Alumina based DCFC fixture was then replaced by quartz based one with similar dimensions. Experimental setup and procedure remained the same. In order to limit the extent of V_2O_5 diffusion through the adhesive, additional quartz adhesive was applied around the anode, particularly at the junction of quartz tube and the solid YSZ electrolyte. Although, the quartz based DCFC survived multiple runs, eventually molten V_2O_5 diffused

(a)   (b)
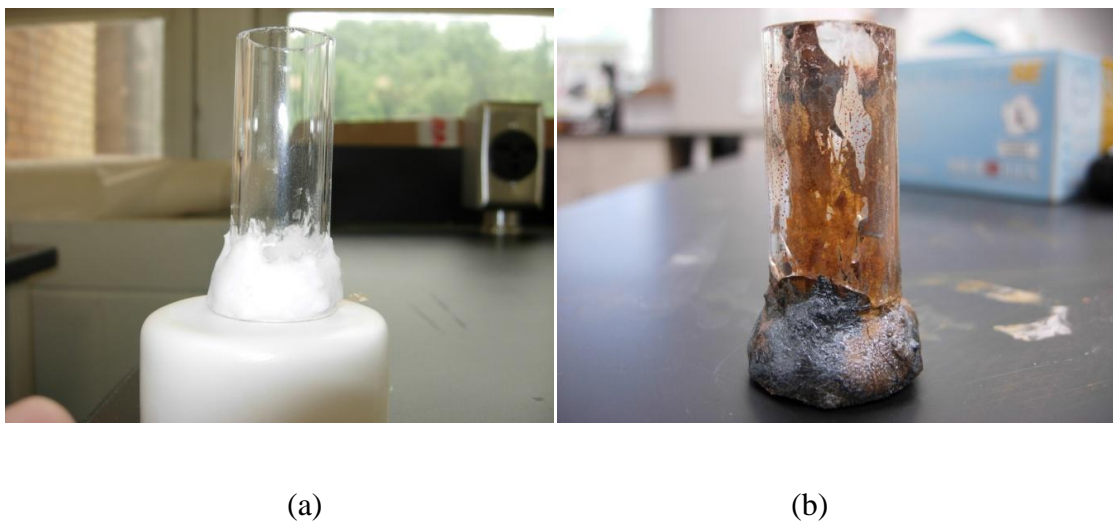
Figure 4.9: Quartz based DCFC a) before and b) after multiple runs

through the quartz adhesive and contacted the LSM cathode. Thermodynamic potential acquired was below 0.2V even at higher temperatures. Figure 4.9 shows the quartz based DCFC fixture before and after measuring the performance. The diffusion of V_2O_5 through quartz adhesive is clearly seen in Figure 4.9 (b). The resistance measured between anode and cathode with varying the temperature has been plotted in Figure 4.10. From the graph, one can see the decrease in resistance with temperature explaining the electrical short between anode and the cathode.
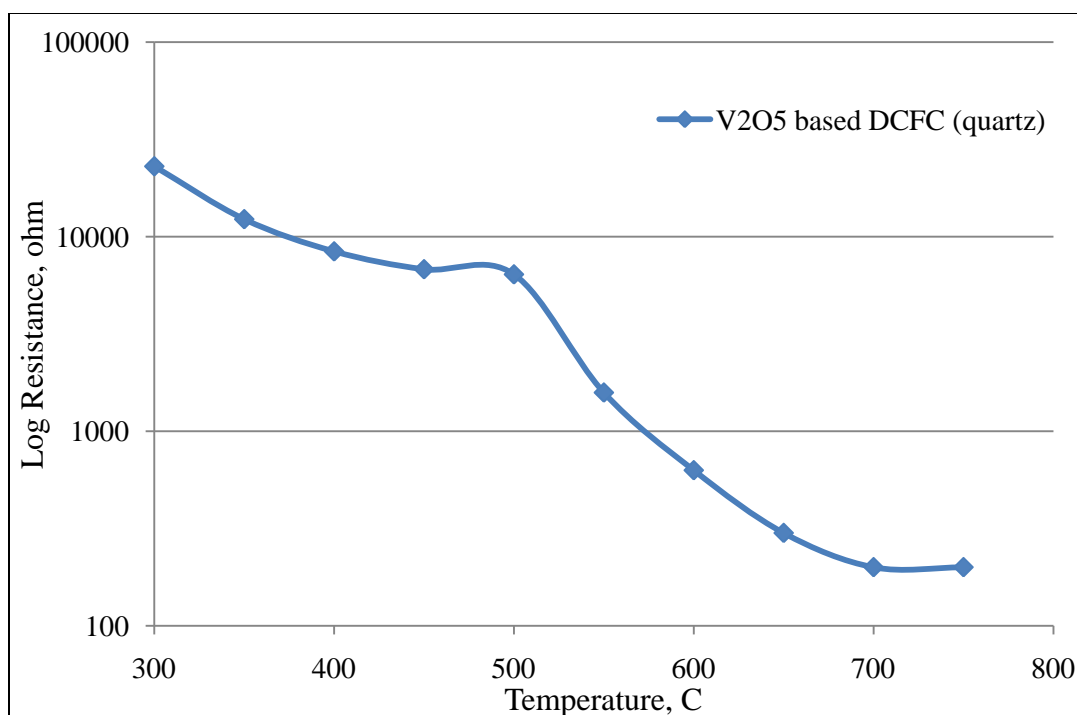
Figure 4.10: Resistance versus temperature data for a V_2O_5 based DCFC fixture

Finally performance of TeO_2 based DCFC fixture also has been evaluated. Similar problems were encountered as in the case of V_2O_5 based DCFC. Although the ionic conductivity of TeO_2 was very high, DCFC studies were discontinued due to its higher cost and lower abundance.

4.6 Conclusions

Performance of the molten metal oxide based DCFC was limited by many issues. Usage of Bi_2O_3 as a liquid electrolyte was hindered by the undesirable bismuth ion reduction at the anode. All the molten oxide based DCFC's exhibited low performance due to material related problems. Sealing the area between ceramic tube and YSZ electrolyte in order to impede the molten electrolyte from contacting the LSM cathode posed was a bigger

problem. Higher volumetric expansion of V_2O_5 caused the alumina and quartz tube to crack leading to electrolyte leakage at higher temperatures. Molten TeO_2 based DCFC was not studied further because of its high cost and lower abundance. Also, Graphite rod was proven to be better anode when compared to the carbon rod at elevated temperatures. These material issues need to be addressed in order to improve the performance of molten oxide fuel cells.

CHAPTER 5

Future work and recommendations

5.1 Conductivity measurements of molten metal oxides

Mixed and electronic conductivity of different metal oxides have been determined in this project using four probe sensing method. Although, the electronic conductivity was accurately measured, ionic conductivity has not been separated from the mixed conductivity. Currently there is no technique available that could precisely separate the ionic conductivity from mixed conductivity. However, measuring the transport number is one of the techniques used in literature to isolate the ionic conductivity from mixed conductivity approxiamately.[54-55] An experimental setup should be designed to calculate the transport number of these metal oxides, in particular, at elevated temperatures. In this study conductivity of the metal oxides has been studied in air environment. Conductivity studies of these metal oxides should be pursued in an inert gas environment. Effect of CO_2 on the conductivities of all the molten metal oxides should be investigated. Finally research should be done on finding an appropriate material for handling the high volumetric expansion of V_2O_5.

5.2 Performance of molten metal oxide based DCFC

Since molten oxide fuel cell research is in an exploratory stage, many fundamental and engineering issues will arise and need to be resolved. Present study mainly identified material related issues involved with construction of the fuel cell. Flooding of the cathode

material by molten electrolyte has proven to be the principle issue that needs to be resolved. Instead of using alumina or quartz adhesive, future research should be focused on identifying novel techniques to seal the edges of the fuel cell. Only few metal oxides existing in the nature can be used as a liquid electrolyte in DCFC because of several constraints such as very high melting points, stability, low abundance, high cost and extreme toxic nature. Doping these metal oxides in order to bring down their melting point and cost seems to be viable option for the future DCFC research. Also, choosing appropriate solid fuel as an anode material seems to be another challenge. Addressing these issues will solve major fundamental aspects related to molten oxide fuel cell.

REFERENCES

1. Gregory A. Hackett, John W. Zondlo, and Robert Svensson, "Evaluation of carbon materials for use in a direct carbon fuel cell," *J. Power Sources*, Vol. 168, 111-118 (2007).

2. Nerine J. Cherepy, Roger Krueger, Kyle J. Fiet, Alan F. Jankowski, and John F. Cooper, "Direct conversion of carbon fuels in a molten carbonate fuel cell," *J. Electrochemical Society*, Vol. 152(1), A80-A87 (2005).

3. Strahinja Zecevic, Edward M. Patton, and Parviz Parhami, "Direct electrochemical power generation from carbon in fuel cells with molten hydroxide electrolyte," *Chem. Eng. Comm.*, Vol. 192, 1655-1670(2005).

4. Sneh L. Jain, J. Barry Lakeman, Kevin D. Pointon, and John T. S. Irvine, "A novel direct carbon fuel cell concept," *J. Fuel Cell Science and Technology*, Vol. 4, 280-282 (2007).

5. Dianxue Cao, Yong Sun, and Guiling Wang, "Direct carbon fuel cell: fundamentals and recent developments," *J. Power Sources*, Vol. 167, 250-257 (2007).

6. John F. Cooper, Nerine Cherepy, and Roger Krueger, "Direct electrochemical conversion of carbon: systems for efficient conversion of fossil fuels into electricity," *Fuel Cell 2000 seminar*, Potland, Aug 2000.

7. Yuta Nabae, Kevin D. Pointon, and John T. S. Irvine, "Electrochemical oxidation of solid carbon in hybrid DCFC with solid oxide and molten carbonate binary electrolyte," *J. Energy & Environmental Science*, Vol. 1, 148-155 (2008).

8. Strahinja Zecevic, Edward M. Patton, and Parviz Parhami, "Carbon-air fuel cell without a reforming process," *Carbon*, Vol. 42, 1983-1993 (2004).

9. W. H. A. Peelen, M. Olivry, S. F. Au, J. D. Fehribach, and K. Hemmes, "Electrochemical oxidation of carbon in a 62/38 mol% Li/K carbonate melt," *J. Applied Electrochemistry*, Vol. 30, 1389-1395 (2000).

10. Xiang Li, Zhonghua Zhu, Jiuling Chen, Roland De Marco, Andrew Dicks, John Bradley, and Gaoqing Lu, " Surface modification of carbon fuels for direct carbon fuel cells," *J. Power Sources*, Vol. 186, 1-9 (2009).

11. Xiang Li, Zhonghua Zhu, Jiuling Chen, Roland De Marco, Andrew Dicks, John Bradley, Shaomin Liu, and Gaoqing Lu, "Factors that determine the performance of carbon fuels in the direct carbon fuel cell," *Ind. Eng. Chem. Res.*, Vol. 47, 9670-9677 (2008).

12. Sneh L. Jain, J. Barry Lakeman, Kevin D. Pointon, R. Marshall, and John T. S. Irvine, "Electrochemical performance of a hybrid direct carbon fuel cell powered by pyrolysed MDF," *J. Energy & Environmental Science*, Vol. 2, 687-693(2009).

13. N. M. Sammes, G. A. Tompsett, H. Nafe, and F. Aldinger, "Bismuth Based Oxide Electrolytes-Structure and ionic Conductivity," *J. European Ceramic Society*, Vol. 19, No. 10, 1801-1826 (1999).

14. P. Shuk, H. D. Wiemhofer, U. Guth, W. Gopel, and M. Greenblatt, "Oxide ion conducting solid electrolytes based on Bi_2O_3," *J. Solid State Ionics*, Vol. 89, 179-196 (1996).

15. K. Laurent, G. Y. Wang, S. Tusseau-Nenez, and Y. Leprice-Wang, "Structure and conductivity studies of electrodeposited δ-Bi_2O_3," *J. Solid State Ionics*, Vol. 178, 1735-1739 (2008).

16. P. D. Battle, C. R. A. Catlow, J. Drennan, and A.D. Murray, "The structural properties of the oxygen conducting δ phase of Bi_2O_3," J. Physics, Vol. 16(17), L 561 (1983).

17. H. A. Harwig and A. G. Gerards, "Electrical properties of α, β, γ and δ phases of Bismuth Sesquioxide," *J. Solid State Chemistry*, Vol. 26, 265-274 (1978).

18. Sossina M. Haile, "Fuel cell materials and components," *Acta Materialia*, Vol. 51, 5981-6000 (2003).

19. Rajalekshmi Chockalingam, Vasantha R. W. Amarakoon, and Herbert Giesche, "Alumina/cerium oxide nano-composite electrolyte for solid oxide fuel cell applications," *J. European Ceramic Society*, Vol. 28, 959-963 (2008).

20. Robert B Darling and Shiho Iwanaga, "Structure, properties, and MEMS and microelectronic applications of vanadium oxides," *Sadhana*, Vol. 34, Part 4, 531-542 (2009).

21. J. Haber, M. Witko, and R. Tokarz, "Vanadium pentoxide I. Structure and properties," *J. Applied Catalysis*, Vol. 157, 3-22 (1997).

22. C. Sanchez, M. Henry, J. C. Grenet, and J. Livage, "Free and bound polarons in vanadium pentoxide," *J. Physical Chemistry*, Vol. 15, 7133-7141 (1982).

23. J. Heamers, E. Baetens, and J. Vennik, "On the electrical conductivity of V_2O_5 single crystals," *J. Phys. Stat. Sol.*, Vol. 20, 381-386 (1973).

24. Ch. Karakotsou, J. A. Kalomiros, M. P. Hanias, A. N. Anagnostopoulos, and J. Spyridelis, "Nonlinear electrical conductivity of V_2O_5 single crystals," *J. American Physical Society*, Vol. 45 (20), 627-631(1992).

25. R. C. Kerby and J. R. Wilson, "Electrical conduction properties of liquid vanadates. I. Vanadium Pentoxide," *Canadian Journal of Chemistry*, Vol. 50, 2865-2870 (1972).

26. D. A. Pantony and K. I. Vasu, "Studies in the corrosion of metals under melts − III : kinetics of the corrosion of pure metals under molten vanadium pentoxide," *J. Inorg. Nucl. Chem.*, Vol.30, 755-779 (1968).

27. T. Alleresma, R. Hakim, T. N. Kennedy, and J. D. Mackenzie, "Structure and physical properties of solid and liquid vanadium pentoxide," *Journal of Chemical Physics*, Vol. 46 (1), 154-160 (1967).

28. A. P. Mirgorodsky, T. Merle-Mejean, J.-C. Champarnaud, P. Thomas, and B. Frit, "Dynamics and structure of TeO_2 polymorphs: model treatment of paratellurite and tellurite; Raman scattering evidence for new γ and δ phases," *Journal of physics and chemistry of solids*, Vol. 61, 501-509 (2000).

29. M. Ceriotti, F. Pietrucci, and M. Bernasconi, "Ab initio study of the vibrational properties of crystalline TeO_2: The α, β, and γ phases," *J. American physical society*, Vol. B 73, 104304 (2006).

30. C. Neatmu, Al. Darabont, E. Surducan, and Gh. Borodi, "Crystal growth and electrical properties of TeO_2 single crystals," *J. Optoelectronics and advanced materials*, Vol. 2 (5), 487-492 (2000).

31. Yanlu Li, Weiliu Fan, Honggang Sun, Xiufeng Cheng, Pan Li, and Xian Zhao, " Structural, electrical, and optical properties of α, β, and γ-TeO_2," *J. Applied Physics*, Vol. 107, 093506 (2010).

32. J. Zemann, "The crystal chemistry of the tellurium oxide and tellurium oxosalt minerals," *Zietschrift fur krystallographie*, Vol. 127, 319-326 (1968).

33. Janusz Leciejewicz, "The crystal structure of tellurium dioxide. A redetermination by neutron diffraction," *Zietschrift fur krystallographie*, Vol. 116, 345-353(1961).

34. E. Hartmann and L. Kovacs, "Electrical conductivity of paratellurite crystals (TeO_2)," *J. Phys. Stat. Sol.*, Vol. 59, 59-64 (1982).

35. H. Jain and A. S. Nowick, "Electrical conduction in paratellurite (TeO_2) crystals," *J. Phys. Stat. Sol.*, Vol. 67, 701-707 (1981).

36. Maria P. Albano, Luis A. Genova, Liliana B. Garrido, and Kevin Plucknett, "Processing of porous yttria-stabilized zirconia by tape-casting," *J. Ceramics International*, Vol. 34, 1983-1988 (2004).

37. http://www.dynacer.com/tape_casting.html.

38. Zuoyan Peng and Meilin Liu, "Preparation of dense platinum-yttria stabilized Zirconia and yttria stabilized Zirconia films on porous $La_{0.9}Sr_{0.1}MnO_3$ (LSM) substrates," *J. Am. Ceram. Soc.*, Vol. 84 (2), 283-288 (2001).

39. Michael C. Tucker, Grace Y. Lau, Craig P. Jackson, Steven J. Visco, and Lutgard C. De Jonghe, "Cu – YSZ cermet solid oxide fuel cell anode prepared by high-temperature sintering," *J. Power Sources*, Vol. 195, 3119-3123 (2010).

40. F. Snijkers, A. de Wilde, S. Mullens, and J. Luyten, "Aqueous tape casting of yttria stabilized Zirconia using natural product binder," *J. European Ceramic Society*, Vol. 24, 1107-1110(2004).

41. Cui Xue-Min, Ouyang –Shi Xi, Huang Yong, Yu Zhi-yong, Zhao Shi-Ke, and Wang-Chang An, "Aqueous tape casting process with Styrene-acrylic latex binder," *J. Wuhan University of Technology*, Vol. 19 (3), 90-93 (2004).

42. Maria P. Albano, Liliana B. Garrido, "Aqueous tape casting of yttria stabilized Zirconia," *J. Materials Science and Engineering*, Vol. A 420, 171-178 (2006).

43. Linghong Luo, Ying Lang, Zuzhi Huang, Liang Cheng, and Jijun Shi, "Fabrication of YSZ film by aqueous tape casting using PVA-B1070 cobinder for IT-SOFC," *J. Key Engineering Materials*, Vols. 434-435, 735-738 (2010).

44. D. Hotza and P. Greil, "Review: aqueous tape casting of ceramic powders," *J. Materials Science and Engineering*, Vol. A 202, 216-227 (1995).

45. Dou Jing, Li Heping, Xu Liping, Zhang Lei, and Wang Guangwei, "Preparation of YSZ solid electrolyte by slip casting and its properties," *J. Rare Metals*, Vol. 28 (4), 372-377 (2009).

46. X. J. Chen, K. A. Khor, S. H. Chan, and L. G. Yu, "Overcoming the effect of contaminant in solid oxide fuel cell (SOFC): spark plasma sintering (SPS) of 0.5 wt % silica doped yttria-stabilized Zirconia (YSZ)," *J. Materials Science and Engineering*, Vol. A 374, 64-71 (2004).

47. K. Wittmann-Teneze and A. L. Sauvet, " Plasma sprayed LSM cathode for solid oxide fuel cells," *ECS transactions*, Vol. 25 (2), 2319-2326 (2009).

48. B. D. White, O. Kesler, N. Ben-Oved, and A. Burgess, "Preparation of an SOFC LSM/YSZ composite cathode by air plasma spraying," *International Thermal Spray Conference*, May 15-18 (2006).

49. Huaiwen Nie, Wenhua Huang, Ting-Lian Wen, Hengyong Tu, and Zhongliang Zhan, "LSM cathodes for SOFC prepared by plasma spraying," *J. Material Science Letters*, Vol. 21, 1951-1953 (2002).

50. Hoda Amani Hamedani, Klaus-Hermann Dahmen, Dongsheng Li, Houman Peydaye-Saheli, Hamid Garmestani, and M. Khaleel, "Fabrication of gradient porous LSM cathode by optimizing deposition parameters in ultrasonic spray pyrolysis," *J. Materials Science and Engineering*, Vol. B 153, 1-9(2008).

51. Jeremiah R. Smith and Eric D. Wachsman, "Effect of harsh anneals on the LSM/YSZ interfacial impedance profile," *Electrochimica Acta*, Vol. 51, 1585-1591 (2006).

52. A. K. Sahu, A. Ghosh, A. k. Suri, P. Sengupta, and K. Bhanumurthy, "Studies on chemical compatibility of lanthanum strontium manganite with yttria-stabilized Zirconia," *Materials Letters*, Vol. 58, 3332-3336 (2004).

53. David R. Lide, "CRC handbook of chemistry and physics," 90th edition (2010).

54. Hooman Hafezi and John Newmann, "Verification and analysis of transference number measurements by the galvanostatic polarization method," *J. Electrochemical Society*, Vol. 147 (8), 3036-3042 (2000).

55. C. H. Chen, H. Kruidhof, H. W. M. Bouwmeester, A. G. Burggraff, "Ionic conductivity of perovskite $LaCoO_3$ measured by oxygen permeation technique," *J. Applied Electrochemistry*, Vol. 27, 71-75 (1997).

APPENDIX A

Experimental data for conductivity measurements of Bi_2O_3

Table A.1 Experimental data for Figure 3.7 (Mixed and electronic conductivity of Bi_2O_3)

(Temperature in ˚C; Mixed (σ mix) and electronic (σ el) conductivity in S/cm)

Temperature	σ mix	σ el
400	4.23E-05	9.78E-06
450	7.76E-05	2.25E-05
500	1.54E-04	4.96E-05
550	2.93E-04	9.89E-05
600	5.13E-04	1.78E-04
650	8.11E-04	2.93E-04
700	1.25E-03	4.56E-04
725	1.64E-03	5.96E-04
750	1.83E-01	1.02E-02
775	2.16E-01	1.10E-02
800	5.54E-01	1.22E-02
825	3.20E+00	6.57E-03
850	3.61E+00	5.99E-03
875	3.91E+00	6.60E-03
900	4.19E+00	7.47E-03

Table A.2 Experimental data for Figure 3.8 (EIS of molten Bi_2O_3 at 900°C) (f: Frequency (Hz); Z: Impedance (ohm); Real and Im represent real and imaginary parts of impedance)

f	Real Z	Im Z
1584.489	0.052346	-0.00015
1513.144	0.052392	-0.00034
1445.798	0.052419	-0.00055
1379.819	0.052462	-0.00076
1318.319	0.052503	-0.00096
1259.04	0.052565	-0.00115
1202.423	0.052631	-0.00134
1148.516	0.052699	-0.00152
1096.604	0.052764	-0.00172
1047.304	0.052843	-0.00194
999.948	0.052914	-0.00219
954.645	0.05301	-0.00245
911.8895	0.053109	-0.00272
870.9225	0.053219	-0.00298
831.5276	0.053353	-0.00322
794.1629	0.05348	-0.00344
758.5585	0.053603	-0.00363
724.2113	0.053721	-0.0038
692.0005	0.05384	-0.00393
660.6634	0.053965	-0.00405
630.984	0.05408	-0.00414
602.4557	0.054192	-0.00421
575.589	0.054289	-0.00428
549.7206	0.054397	-0.00436
524.7202	0.05452	-0.00448
501.3029	0.054614	-0.00463
478.7072	0.054763	-0.00476

456.9087	0.054914	-0.0049
436.4885	0.055078	-0.00506
416.9233	0.055239	-0.00522
398.2093	0.0554	-0.00539
380.3111	0.055568	-0.00556
363.2232	0.055741	-0.00573
346.8022	0.055918	-0.00592
331.2025	0.056113	-0.0061
316.1132	0.056325	-0.00631
301.9627	0.056558	-0.00654
288.4026	0.056821	-0.00678
275.3585	0.057115	-0.00702
262.9831	0.057424	-0.00726
251.1851	0.057741	-0.00749
239.8863	0.058053	-0.0077
229.0513	0.05835	-0.00789
218.7509	0.058624	-0.00805
208.9236	0.058875	-0.0082
199.4949	0.059099	-0.00832
190.5486	0.059287	-0.00843
181.9786	0.059451	-0.00851
173.755	0.059598	-0.00859
165.9617	0.059739	-0.00867
158.5334	0.059884	-0.00874
151.4051	0.060063	-0.00883
144.5599	0.060245	-0.00891
138.009	0.060477	-0.00902
131.7766	0.060737	-0.00915
125.9111	0.060999	-0.00927
120.1928	0.061314	-0.0094
114.8004	0.061602	-0.00955

109.6725	0.061909	-0.00972
104.7421	0.062237	-0.00989
100.0091	0.062571	-0.01007
95.5071	0.062931	-0.01026
91.19696	0.06333	-0.01045
87.12894	0.063737	-0.01062
83.18014	0.064177	-0.0108
79.40828	0.064636	-0.01094
75.84877	0.065129	-0.01106
72.44199	0.065559	-0.01118
69.19353	0.066012	-0.01128
66.05498	0.066446	-0.01133
63.0971	0.066865	-0.01145
60.26402	0.066918	-0.01144
54.54756	0.067883	-0.01177
54.54756	0.067748	-0.01169
54.54756	0.067679	-0.01172
50.00829	0.068299	-0.01192
46.16752	0.068793	-0.01205
46.16752	0.068655	-0.01204
42.85946	0.069186	-0.0122
42.85946	0.069099	-0.01218
40.00589	0.069625	-0.01224
37.50808	0.070134	-0.01231
35.30457	0.070617	-0.01237
35.30457	0.070611	-0.01238
33.32644	0.07116	-0.01248
31.57928	0.07169	-0.01258
30.00162	0.072216	-0.01272
28.57484	0.072738	-0.0128
27.27844	0.073235	-0.01287

26.09379	0.073742	-0.01292
24.99111	0.074238	-0.01297
23.99459	0.074676	-0.01296
23.07258	0.075065	-0.0129
22.21949	0.075479	-0.01288
20.69026	0.076108	-0.01283
20.00108	0.076361	-0.01273
19.35474	0.076698	-0.01277
18.18314	0.077193	-0.01274
17.14565	0.077723	-0.01278
16.66881	0.07793	-0.01282
15.79337	0.078339	-0.01286
14.99429	0.078715	-0.01289
14.28276	0.079078	-0.01291
13.95121	0.079143	-0.01291
13.04224	0.07967	-0.01288
12.50021	0.079925	-0.01284
12.00102	0.080154	-0.01274
11.53909	0.080419	-0.01269
10.91137	0.080887	-0.01262
10.52394	0.081164	-0.01258
9.99868	0.081671	-0.01256
9.5237	0.082221	-0.01253
9.09157	0.082751	-0.01249
8.69669	0.083266	-0.01244
8.331611	0.083722	-0.01236
7.893889	0.084188	-0.01224
7.594004	0.084504	-0.01212
7.228925	0.084809	-0.01196
6.897375	0.085125	-0.01177
6.591901	0.085436	-0.01171

6.316229	0.085939	-0.01162
5.999579	0.086367	-0.01156
5.770474	0.086699	-0.01153
5.505979	0.08698	-0.01147
5.263835	0.087324	-0.01141
4.997477	0.087579	-0.01135
4.798173	0.087873	-0.01127
4.580244	0.08803	-0.01121
4.379078	0.08832	-0.0111
4.166737	0.088584	-0.01099
3.973022	0.088803	-0.01088
3.797933	0.089101	-0.01079
3.637746	0.08934	-0.01069
3.468245	0.089718	-0.01057
3.315508	0.090121	-0.01047
3.157183	0.090519	-0.01034
3.01376	0.090868	-0.01019
2.885237	0.091248	-0.01003
2.752989	0.091541	-0.00985
2.631917	0.091769	-0.00968
2.510845	0.092031	-0.0095
2.399087	0.092068	-0.00934
2.289191	0.092246	-0.00919
2.19047	0.092462	-0.00906
2.089888	0.092725	-0.00893
1.994893	0.092962	-0.00881
1.905486	0.093136	-0.00872
1.817942	0.093314	-0.00863
1.73971	0.093459	-0.00856
1.657754	0.093548	-0.00846
1.583248	0.093734	-0.00837

1.51433	0.093966	-0.00826
1.445413	0.094246	-0.0081
1.38022	0.094592	-0.00793
1.318753	0.094905	-0.00767
1.257285	0.095046	-0.00743
1.203269	0.095166	-0.00715
1.147389	0.095181	-0.00685
1.097098	0.095337	-0.00665
1.046806	0.095461	-0.00656
1.000064	0.095491	-0.00674
0.955307	0.095432	-0.00661
0.911823	0.095404	-0.00649
0.870571	0.095572	-0.00629
0.832268	0.09585	-0.00605
0.794599	0.096139	-0.00573
0.75879	0.096319	-0.00535
0.724453	0.096274	-0.00503
0.692229	0.09636	-0.00483
0.660621	0.096568	-0.00464
0.631058	0.096689	-0.00452
0.602352	0.096662	-0.00442
0.575083	0.096105	-0.00418
0.549286	0.095778	-0.00391
0.525034	0.096067	-0.00356
0.501187	0.096211	-0.00317
0.478473	0.096264	-0.00275
0.457032	0.0965	-0.0025
0.436306	0.096803	-0.00246
0.417	0.096287	-0.00239
0.398272	0.095225	-0.00208
0.380115	0.095332	-0.00172

0.363001	0.095409	-0.00123
0.346945	0.095636	-0.00089
0.331066	0.09618	-0.00085
0.316296	0.095411	-0.00087
0.301967	0.094229	-0.00082
0.288476	0.094542	-0.00025
0.275486	0.094988	-0.0000303
0.262941	0.095511	-0.0000162
0.251206	0.094487	0.000152
0.239927	0.093766	0.000333
0.229079	0.094497	0.000444
0.218666	0.094639	0.000714
0.208969	0.093408	0.000861
0.199461	0.093652	0.000876

Table A.3 Experimental data for Figure 3.10 (Variation of conductivity under CO_2 environment at 825˚C) (Mixed conductivity (σ mix) in S/cm and Time in min)

Time	σ mix
0	3.404255
5	3.296703
10	3.3241
15	3.092784
20	3.057325
25	3
30	2.944785
35	2.891566
40	2.826855
45	2.803738
50	2.774566
55	2.702703
60	2.780997
65	2.70575
70	2.614379
75	2.566845
80	2.330097
85	2.222222
90	2.033898
95	1.967213
100	1.904762
105	1.904762
110	1.897233
115	1.882353
120	1.875

APPENDIX B

Conductivity measurements of V_2O_5

Table B.1 Experimental data for Figure 3.15 (Total and electronic conductivity of V_2O_5 using quartz and alumina crucibles) (Temperature in ˚C; Mixed (σ mix) and electronic (σ el) conductivity in S/cm)

Temperature	Alumina crucible		Quartz crucible	
	σ mix	σ el	σ mix	σ el
200	7.33E-04	1.17E-04	6.83E-03	1.24E-03
225	1.11E-03	1.86E-04	8.36E-03	1.52E-03
250	1.54E-03	2.63E-04	9.96E-03	1.74E-03
275	2.04E-03	3.57E-04	1.16E-02	2.00E-03
300	2.56E-03	4.54E-04	1.30E-02	2.19E-03
325	3.20E-03	5.64E-04	1.30E-02	2.39E-03
350	3.83E-03	6.88E-04	1.41E-02	2.58E-03
375	4.51E-03	8.14E-04	1.50E-02	2.79E-03
400	5.13E-03	9.39E-04	1.68E-02	2.98E-03
425	5.75E-03	1.05E-03	1.79E-02	3.09E-03
450	6.34E-03	1.17E-03	1.95E-02	3.25E-03
475	6.89E-03	1.28E-03	2.07E-02	3.39E-03
500	7.32E-03	1.38E-03	2.19E-02	3.53E-03
525	7.84E-03	1.48E-03	2.32E-02	3.65E-03
550	8.37E-03	1.59E-03	2.38E-02	3.78E-03
575	9.07E-03	1.74E-03	2.51E-02	3.79E-03
600	1.01E-02	1.91E-03	2.62E-02	3.89E-03
625	1.10E-02	2.08E-03	2.81E-02	3.97E-03
650	1.22E-02	2.25E-03	2.98E-02	3.96E-03
675	1.32E-02	2.55E-03	3.09E-02	4.00E-03

700	2.53E-02	3.02E-03	4.37E-02	4.05E-03
725	3.54E-02	3.04E-03	5.25E-02	3.32E-03
750	6.72E-02	2.90E-03	7.87E-02	3.32E-03

Table B.2 Experimental data for Figure 3.16 (EIS of V_2O_5 at 675˚C) (f: Frequency (Hz); Z:

Impedance (ohm); Real and Im represent real and imaginary parts of impedance)

Frequency	Real Z	Im Z
7942.6	3.219328	-0.00173
6311.096	3.222246	-0.00407
5011.18	3.208557	-0.00667
3980.932	3.198439	-0.00846
3162.667	3.185454	-0.01204
2511.16	3.18153	-0.01287
1995.371	3.177914	-0.01472
1584.489	3.175828	-0.01622
1259.04	3.170235	-0.01767
999.948	3.16965	-0.01948
794.1629	3.170895	-0.02054
630.984	3.171344	-0.02164
501.3029	3.172691	-0.02332
398.2093	3.172242	-0.02148
316.1132	3.172992	-0.02137
251.1851	3.166289	-0.02234
199.4949	3.166726	-0.02302
158.5334	3.167806	-0.02423
125.9111	3.168545	-0.02509
100.0091	3.170694	-0.02579
79.40828	3.173266	-0.02692
63.0971	3.176607	-0.02476
50.00829	3.179594	-0.02756
40.00589	3.184701	-0.0265
31.57928	3.187891	-0.02696
24.99111	3.191433	-0.02702
20.00108	3.194785	-0.0273

15.79337	3.198736	-0.02616
12.50021	3.202443	-0.0262
9.99868	3.206048	-0.02526
7.893889	3.210985	-0.02476
6.316229	3.214928	-0.02478
4.997477	3.219727	-0.0242
3.973022	3.242944	-0.02416
3.157183	3.245429	-0.02363
2.510845	3.248584	-0.02375
1.994893	3.251012	-0.02502
1.583248	3.253357	-0.02477
1.257285	3.25319	-0.02433
1.000064	3.257847	-0.02341
0.794599	3.264038	-0.02241
0.631058	3.268064	-0.02406
0.501187	3.270448	-0.02365
0.398272	3.291631	-0.0107

APPENDIX C

Conductivity measurements of TeO$_2$

Table C.1 Experimental data for Figure 3.20 (Mixed and electronic conductivity of TeO$_2$)

(Temperature in ˚C; Mixed (σ mix) and electronic (σ el) conductivity in S/cm)

Temperature	σ mix	σ el
400	5.20E-06	1.37E-07
450	2.71E-05	1.39E-06
500	5.08E-05	5.87E-06
550	1.44E-04	1.09E-05
600	3.27E-04	1.03E-05
625	5.02E-04	1.03E-05
650	8.52E-04	6.03E-05
675	1.94E-03	1.02E-04
700	3.36E-03	1.40E-04
725	7.45E-03	1.75E-04
750	1.36E-01	2.42E-04
775	1.34E+00	3.12E-04
800	1.57E+00	3.35E-04
825	1.84E+00	4.19E-04

Table C.2 Experimental data for Figure 3.21 (EIS of TeO$_2$ at 800˚C) (f: Frequency (Hz); Z:

Impedance (ohm); Real and Im represent real and imaginary parts of impedance)

Frequency	Real Z	Im Z
1584.5	0.08111	-0.00067
1259.04	0.081409	-0.00188
999.948	0.081929	-0.00302
794.1629	0.082691	-0.0041
630.984	0.083584	-0.00507
501.3029	0.084644	-0.00598
398.2093	0.086001	-0.00663
316.1132	0.087519	-0.0072
251.1851	0.089185	-0.00758
199.4949	0.090753	-0.00764
158.5334	0.092096	-0.00747
125.9111	0.09313	-0.0072
100.0091	0.094175	-0.00689
79.40828	0.095074	-0.00655
63.0971	0.095809	-0.00614
50.00829	0.096019	-0.00588

APPENDIX D

Performance of molten metal oxide electrolytes in a DCFC

Table D.1 Experimental data for Figure 4.4 (Performance of DCFC with a carbon rod) (Temperature in °C and Voltage in Volts)

Temperature	Voltage
400	0.185
425	0.237
450	0.281
475	0.371
500	0.505
525	0.511
550	0.497
575	0.486
600	0.474
625	0.463
650	0.454
675	0.45
700	0.444
725	0.438
750	0.448
775	0.447
800	0.358
825	0

Table D.2 Experimental data for Figure 4.5 (Performance of DCFC with graphite strip as

anode material) (Temperature in ˚C and Voltage in Volts)

Temperature	Voltage
400	0.088
425	0.156
450	0.181
475	0.446
500	0.528
525	0.539
550	0.531
575	0.522
600	0.511
625	0.502
650	0.491
675	0.456
700	0.44
725	0.436
750	0.438
775	0.35
800	0.33
825	0.334

Table D.3 Experimental data for Figure 4.7 (Variation of resistance between anode and cathode with temperature in a Bi_2O_3 based DCFC) (Resistance in ohms and Temperature in ˚C)

Temperature	Resistance
550	900000
600	340000
625	210000
650	127000
675	70000
725	56000
775	18000
800	9000
825	1000

Table D.4 Experimental data for Figure 4.10 (Variation of resistance between anode and cathode with temperature in a V_2O_5 based DCFC) (Resistance in ohms and Temperature in ˚C)

Temperature	Resistance
300	23000
350	12300
400	8400
450	6800
500	6400
550	1580
600	630
650	300
700	200
750	200